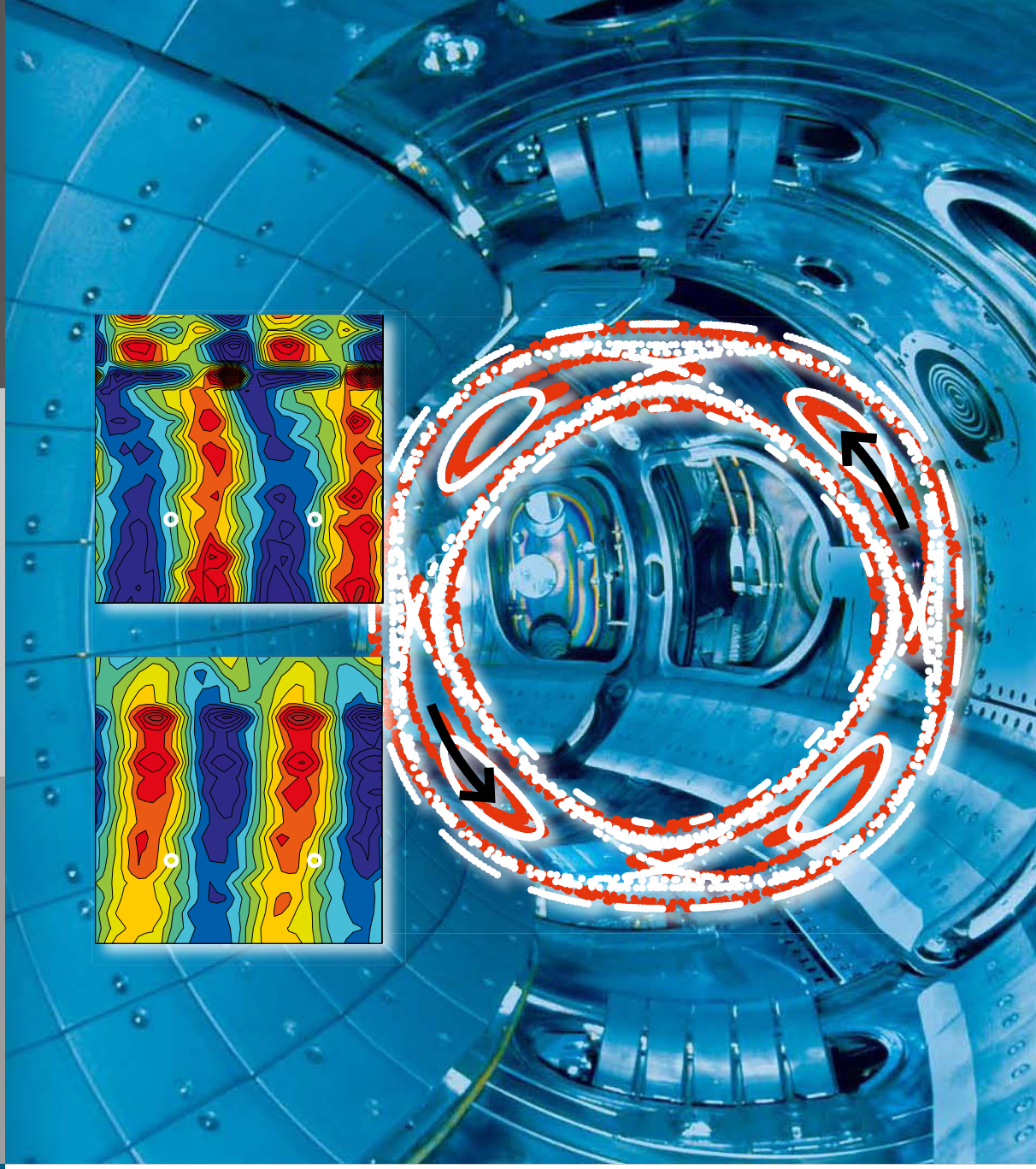

Electron Transport in the Plasma Edge with Rotating Resonant Magnetic Perturbations at the TEXTOR Tokamak

Henning Stoschus

Mitglied der Helmholtz-Gemeinschaft

JÜLICH
FORSCHUNGSZENTRUM

Electron Transport in the Plasma Edge with Rotating Resonant Magnetic Perturbations at the TEXTOR Tokamak

Inaugural-Dissertation

zur
Erlangung des Doktorgrades der
Mathematisch-Naturwissenschaftlichen Fakultät
der Heinrich-Heine-Universität Düsseldorf

vorgelegt von

Henning Stoschus
aus Siegen

März 2011

Aus dem
Institut für Energie- und Klimaforschung – Plasmaphysik,
Forschungszentrum Jülich GmbH
für die Heinrich-Heine-Universität Düsseldorf

Gedruckt mit der Genehmigung der
Mathematisch-Naturwissenschaftlichen Fakultät der
Heinrich-Heine-Universität Düsseldorf

Referent: Prof. Dr. Ulrich Samm
Koreferent: Prof. Dr. Georg Pretzler

Tag der mündlichen Prüfung: 27.06.2011

Forschungszentrum Jülich GmbH
Institut für Energie- und Klimaforschung (IEK)
Plasmaphysik (IEK-4)

Electron Transport in the Plasma Edge with Rotating Resonant Magnetic Perturbations at the TEXTOR Tokamak

Henning Stoschus

Schriften des Forschungszentrums Jülich
Reihe Energie & Umwelt / Energy & Environment Band / Volume 111

ISSN 1866-1793 ISBN 978-3-89336-718-4

Bibliographic information published by the Deutsche Nationalbibliothek.
The Deutsche Nationalbibliothek lists this publication in the Deutsche Nationalbibliografie; detailed bibliographic data are available in the Internet at http://dnb.d-nb.de.

Publisher and Distributor:	Forschungszentrum Jülich GmbH Zentralbibliothek 52425 Jülich Phone +49 (0) 24 61 61-53 68 · Fax +49 (0) 24 61 61-61 03 e-mail: zb-publikation@fz-juelich.de Internet: http://www.fz-juelich.de/zb
Cover Design:	Grafische Medien, Forschungszentrum Jülich GmbH
Printer:	Grafische Medien, Forschungszentrum Jülich GmbH
Copyright:	Forschungszentrum Jülich 2011

Schriften des Forschungszentrums Jülich
Reihe Energie & Umwelt / Energy & Environment Band / Volume 111

D 61 (Diss. Düsseldorf, Univ., 2011)

ISSN 1866-1793
ISBN 978-3-89336-718-4

The complete volume ist freely available on the Internet on the Jülicher Open Access Server (JUWEL) at http://www.fz-juelich.de/zb/juwel

Abstract

Small three-dimensional (3D) magnetic perturbations can be used as a tool to control the edge plasma parameters in magnetically confined plasmas in high confinement mode ("H-mode") to suppress edge instabilities inherent to this regime, the Edge Localized Modes (ELMs). In this work, the impact of rotating 3D resonant magnetic perturbation (RMP) fields on the edge plasma structure characterized by electron density and temperature fields is investigated. We study a low confinement (L-mode) edge plasma ($r/a > 0.9$) with high resistivity (edge electron collisionality $\nu_e^* > 4$) at the TEXTOR tokamak. The plasma structure in the plasma edge is measured by a set of high resolution diagnostics: a fast CCD camera ($\Delta t = 20\,\mu$s) is set up in order to visualize the plasma structure in terms of electron density variations. A supersonic helium beam diagnostic is established as standard diagnostic at TEXTOR to measure electron density n_e and temperature T_e with high spatial ($\Delta r = 2\,$mm) and temporal resolution ($\Delta t = 20\,\mu$s). The measured plasma structure is compared to modeling results from the fluid plasma and kinetic neutral transport code EMC3-EIRENE.

A sequence of five new observations is discussed: (1) Imaging of electron density variations in the plasma edge shows that a fast rotating RMP field imposes an edge plasma structure, which rotates with the external RMP rotation frequency of $|\nu_{RMP}| = 1\,$kHz. (2) Measurements of the electron density and temperature provide strong experimental evidence that in the far edge a rotating 3D scrape-off layer (SOL) exists with helical exhaust channels to the plasma wall components. (3) Radially inward, the plasma structure at the next rational flux surface is found to depend on the relative rotation between external RMP field and intrinsic plasma rotation. For low relative rotation the plasma structure is dominated by a particle and energy loss along open magnetic field lines to the wall components. For high relative rotation indications for a magnetic island acting as locally confining sub-volumes are found. (4) For high relative rotation, the entire measured edge plasma structure is shifted by $\pi/2$ toroidally with respect to the position modeled in vacuum approximation. The latter two experimental findings are compatible with modeling results of the underlying magnetic topology including plasma response obtained by a 4-field drift fluid transport model. (5) A smaller shift is measured in front of the RMP coils. This gives direct experimental evidence that the near field plasma structure is governed by the competition between the RMP near field and the local plasma structure at the next inward rational flux surface.

The results obtained are essential input for benchmarking models, which include plasma response, in order to extrapolate the RMP imposed 3D plasma structure toward the next step fusion experiment ITER. The measurements of the plasma structure presented indicate that the underlying magnetic topology is rotation dependent and may therefore stimulate direct measurements of the components of the magnetic field in future.

Kurzfassung

Kleine dreidimensionale (3D) magnetische Störungen stellen eine Möglichkeit dar, die Plasmaparameter am Rand in magnetisch eingeschlossenen Fusionsplasmen so zu kontrollieren, dass typische Randschichtinstabilitäten, sogenannte Edge Localized Modes (ELMs), unterdrückt werden. In dieser Arbeit wird der Einfluss von rotierenden, dreidimensionalen, resonanten magnetischen Störfeldern (Resonant Magnetic Perturbation fields - RMP fields) auf die Randschichtplasmastruktur anhand von Messungen von Elektronendichte- und Temperaturfeldern untersucht. Gegenstand der Untersuchung ist ein hoch resistives Randschichtplasma ($r/a > 0.9$, Elektronenstößigkeit $\nu_e^* > 4$) am Tokamak TEXTOR in der sogenannten L-mode (low confinement mode). Die Plasmastruktur wird mit einem Satz von hochauflösenden Diagnostiken gemessen: eine schnelle CCD Kamera ($\Delta t = 20\,\mu$s) wurde aufgebaut, um die Plasmastruktur im Hinblick auf Variationen der Elekronendichte zu visualisieren. Ein Helium-Überschallstrahl wurde als Standarddiagnostik an TEXTOR etabliert, um Elektronendichte n_e und -temperatur T_e mit hoher Raum- ($\Delta r = 2\,$mm) und Zeitauflösung ($\Delta t = 20\,\mu$s) zu messen. Die experimentell charakterisierte Plasmastruktur wird mit dem 3D Transport Modell EMC3-EIRENE verglichen, das das Plasma im Flüssigkeitsbild und Neutralteilchen in einem kinetischen Modell beschreibt.

Fünf neue Beobachtungen werden diskutiert: (1) Die visuelle Beobachtung von Elektronendichtevariationen im Plasmarand zeigt, dass schnell rotierende RMP Felder eine Plasmastruktur aufprägen, welche mit der Rotationsfrequenz des externen Störfeldes von $|\nu_{RMP}| = 1\,$kHz rotiert. (2) Messungen der Elektronendichte und -temperatur liefern experimentelle Belege, dass in der äußersten Randschicht eine rotierende, 3D Abschälschicht mit helikalen Strömungskanälen zur Wand existiert. (3) Radial innen konnte gezeigt werden, dass die Plasmastruktur an der nächsten rationalen Flussfläche von der Relativrotation zwischen externem RMP Feld und intrinsischer Plasmarotation abhängt. Für geringe Relativrotation ist die Plasmastruktur dominiert durch einen Teilchen- und Energieverlust aufgrund von offenen magnetischen Feldlinien. Für hohe Relativrotation wurden Anzeichen für eine rotierende magnetische Insel mit lokalem Einschluss in Teilvolumina gefunden. (4) Für hohe Relativrotation stellt sich eine Verschiebung der gesamten Randschicht-Plasmastruktur im Vergleich mit der berechneten Position in der Vakuumnäherung um $\pi/2$ in toroidaler Richtung ein. Diese Befunde for hohe Relativrotation sind in qualitativer Übereinstimmung mit Modellierungsergebnissen der zugrunde liegenden Magnetfeldtopologie mit interner Plasmareaktion, welche im Rahmen eines Flüssigkeitsmodells mit Teilchendriften beschrieben wird. (5) Eine geringere Verschiebung der Plasmastruktur in der Nähe der RMP Spulen weist deutlich darauf hin, dass ein Wettbewerb zwischen dem magnetischen Nahfeld und der lokalen Plasmastruktur an der äußersten rationalen Flussfläche existiert, die somit letztlich die Wechselwirkung der 3D Randschicht mit der Wand bestimmt.

Diese Ergebnisse stellen eine grundlegende Referenz für Modellierungen mit selbstkonsistenter Plasmareaktion dar, um die durch RMP Feldern aufgeprägte Plasmastruktur prädiktiv hin zum zukünftigen Fusionsreaktor ITER zur extrapolieren. Die Messungen der Plasmastruktur weisen auf eine Rotationsabhängigkeit der zugrunde liegenden Magnetfeldtopologie hin und motivieren daher direkte Messungen des Magnetfeldes in Zukunft.

Contents

Chapter 1

Introduction

Controlled nuclear fusion is an option as future energy source for base electricity supply [1]. For this purpose, the fusion process of light nuclei can be utilized. The fusion reaction

$$D + T \rightarrow He + n + 17.6\,\mathrm{MeV} \tag{1.1}$$

between the hydrogen isotopes deuterium (D) and tritium (T) is most promising for the application on earth since for this reaction the highest fusion rate is reached for accessible temperatures of $T = 10 - 30\,\mathrm{keV}$[1] [2]. At these temperatures, the fuel mixture represents a fully ionized plasma, in which deuterium and tritium nuclei are fused to an helium (He) nucleus and a neutron. A free energy of 17.6 MeV is released and distributed to the fusion products as kinetic energy.
In order to achieve a positive energy balance by this process, a thermo-nuclear system has to be created. This requires thermal insulation and confinement of the plasma with a sufficient high temperature T and density n_0. The so-called *fusion triple product*

$$n_0 \cdot T \cdot \tau_E > 10^{21}\,\mathrm{keV\,s\,m^{-3}} \tag{1.2}$$

quantifies the confinement with τ_E being the energy confinement time which describes the characteristic timescale on which the constituents are thermally insulated [3]. The lower limit in Eq. 1.2 defines the plasma parameters for which the fusion power (P_F) balances the externally applied heating power (P_H^{ext}), i.e. power gain $Q = P_F/P_H^{ext} = 1$.
At present, the realization of a confined D-T plasma with $Q \gg 1$ is the main aim of the international fusion community. Therefore, devices have been developed in order to confine and insulate high temperature plasmas. The most promising approach is the so-called *Tokamak*[2] concept [3, 4]. It utilizes a doughnut-like, i.e. toroidally symmetric setup of magnetic fields in order to reduce particle and energy losses effectively. At the JET tokamak in England, a power gain of $Q = 0.6$ was achieved in 1997 which showed the general applicability of the fusion process as an energy source on earth [5]. The new experiment *ITER* (latin: "the way") shall demonstrate physical and technical solutions

[1] $T[\mathrm{eV}] = k_B \cdot T[\mathrm{K}]$ with k_B: Boltzmann constant

[2] "ТОраидальная КАмера в Магнитных Катушках - russian: toroidal chamber with magnetic field, ТОК - russian: current

for a fusion plasma with a power gain of $Q = 10$ for a duration of eight minutes for the first time.

In order to achieve this goal, the baseline scenario for ITER is foreseen to run in so-called high confinement mode ("H-mode") [6] which is characterized by steep edge pressure and current gradients. They drive the plasma edge unstable toward peeling (current driven) and ballooning (pressure gradient driven) modes causing repetitive instabilities, the so-called Edge Localized Modes (ELMs) [7]. ELMs lead to high transient heat and particle loads to the plasma facing components which will potentially reduce the lifetime of the plasma facing components in ITER due to enhanced material erosion [8]. It was shown experimentally at the DIII-D tokamak that small three-dimensional (3D) Resonant Magnetic Perturbations (RMPs) can be used as a tool to suppress ELMs [9]. The physical mechanisms of ELM suppression are not yet fully understood but are supposed to depend on the impact of RMP fields on transport processes in the plasma edge and the resulting 3D distribution of the plasma parameters, i.e. on the plasma structure.

In the frame of this work, the impact of externally applied Resonant Magnetic Perturbation fields on the edge plasma at the TEXTOR tokamak is studied experimentally. The measurements obtained provide direct experimental information on the plasma structure imposed by the RMP field. They allow to study the local transport mechanisms and to conclude on the underlying magnetic topology.
The particular aim of this thesis is the characterization of the RMP imposed 3D plasma structure for fast rotating RMP fields by means of electron density and temperature profile measurements with high temporal and spatial resolution. A gas-puff imaging diagnostic was developed in the frame of this work in order to visualize the rotating edge plasma structure. A more detailed study was possible utilizing a Supersonic Helium Beam diagnostic which was improved toward high temporal and spatial resolution and established as a standard diagnostic.
The measurements obtained are performed in highly resistive edge plasmas in low confinement mode ("L-mode") at the TEXTOR tokamak featuring a flexible RMP coil set, the Dynamic Ergodic Divertor (DED). Rotation of the external RMP field is utilized in this context for two purposes: (a) as a diagnostic tool to scan the potential 3D plasma structure in the rotation direction of the RMP field and (b) in order to change the relative rotation between plasma fluid and RMP field externally to study the rotation dependence of internal plasma response.

The measurements provide experimental information, in how far the characteristic topological domains found with static RMP fields are preserved with fast rotating RMP fields. A detailed comparison of the experimentally determined plasma structure with basic findings with static RMP fields and simulations of the local transport properties allow to deduce indirectly the underlying magnetic topology. Additionally, for the first time the rotation dependence of the edge plasma structure is measured. A more complete interpretation will be provided by a comparison of the experimental results with models including non-linear coupling effects between RMP field, equilibrium and plasma parameters, i.e. plasma response effects.

The thesis is structured as follows:

- In chapter 2, the tokamak principle and the edge instability control by means of Resonant Magnetic Perturbations will be introduced.
- A brief description of the setup of the TEXTOR tokamak will be given in chapter 3.
- A set of high resolution diagnostics for probing the edge plasma will be introduced in chapter 4. The focus will be on two diagnostics, which were set up and improved in the frame of this work: a Supersonic Helium Beam diagnostic and a new gas-puff imaging system. A set of high resolution Langmuir probes as standard diagnostic at TEXTOR will be described.
- Chapter 5 will focus on concepts to model the magnetic topology in the plasma edge under impact of Resonant Magnetic Perturbation fields at TEXTOR. The so-called vacuum approximation will be introduced and their limitations discussed. Modeling results of a more complete 4-field drift-fluid model will be described which avoids the vacuum approximation and takes into account internal plasma response self-consistently.
- Chapter 6 is dedicated to new results which provide strong experimental evidence that a plasma edge structure exists and depends on the relative rotation level between externally applied DED field and plasma fluid.
- In chapter 7, a summary of the results and conclusions toward high performance H-mode plasmas in ITER will be given.

Chapter 2

Basics of Tokamaks and Edge Stability Control

In section 2.1, we will introduce briefly the tokamak as plasma confining device and concepts for particle and energy exhaust. A detailed description can be found in Ref. [3] and references therein. In section 2.2, we motivate the studies in the frame of this work by showing one example of controlling the plasma edge parameters and hence the edge stability with external Resonant Magnetic Perturbations at the DIII-D tokamak [10]. It will be shown for high performance plasmas with improved confinement that the plasma edge parameters vary with the coupling between the RMP field and the plasma. However, this modulation is not correlated to the stability of the plasma edge, which motivates basic studies to get a physical understanding of the impact of Resonant Magnetic Perturbation fields.

2.1 Basics of Tokamaks

2.1.1 Tokamak Principle

Devices based on magnetic confinement utilize the physical effect that charged particles gyrate in a magnetic field around magnetic field lines due to the Lorentz force. The motion of charged particles perpendicular to the magnetic field is reduced. In a toroidal, i.e. "doughnut"-shaped, setup closed field lines avoid end losses effectively due to field lines intersecting the material walls.
Figure 2.1 shows schematically such a toroidal device based on the so-called *Tokamak*-concept[1] [3, 4]. It consists basically of a toroidal vacuum chamber with a major radius R and a minor radius r. The main magnetic field B_t in the toroidal direction ϕ is generated by toroidal field coils. It represents the strongest component of the magnetic

[1] "ТОраидальная КАмера в Магнитных Катушках - russian: toroidal chamber with magnetic field, ТОК - russian: current

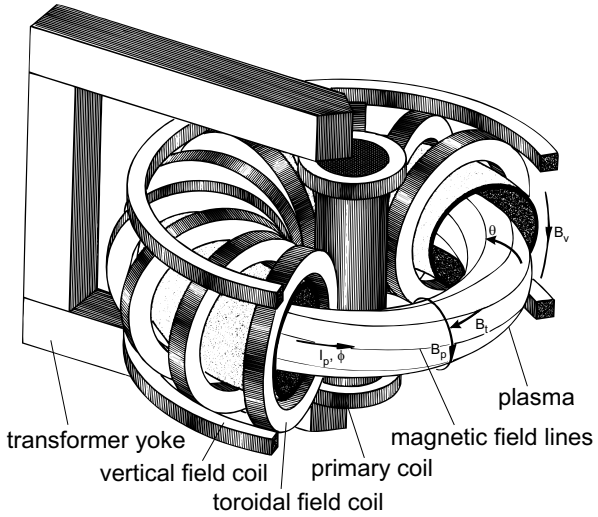

Figure 2.1: Tokamak principle by means of a circular shaped toroidal chamber.

field typically in the order of several tesla and decreases with increasing major radius of the device. Therefore, the inner side of the vessel is termed high magnetic field side (HFS) and the outer side low field side (LFS). The poloidal magnetic field B_p in the poloidal direction Θ is generated by inducing a current I_p in the plasma as a highly conductive medium. For this, the transformer principle is utilized with a primary coil at the center of the tokamak, the toroidally formed plasma representing a single winded secondary coil and transformer yokes. The superposition of both, B_t and B_p results in a magnetic topology with helically wounded magnetic field lines as shown in figure 2.2. The helicity is described by the so-called safety factor $q = d\phi/d\Theta$. In other words, q gives the toroidal angle $\Delta\phi$ after which a field line returns to the same poloidal position ($\Delta\Theta = 2\pi$). For a tokamak geometry with $r \ll R$, one can calculated q as a function of the magnetic field and the geometrical dimensions

$$q(r) = \frac{2\pi r^2 B_t}{\mu_0 I_p(r) R} \tag{2.1}$$

with the plasma current profile $I_p(r)$ and the magnetic susceptibility μ_0 [3]. Hence, the helicity of magnetic field lines depends on the radial position but can be steered by the current profile and the toroidal magnetic field B_t.

The helical setup of the magnetic field enables the confinement of the plasma by avoiding effectively drifts which occur due to the warped field lines on toroidal pathes, i.e. due to curvature and inhomogeneity of the magnetic field. These drifts (∇B and curvature drifts) are directed perpendicular to ∇B and $\vec{B}$ and separate positive and negative charges vertically. Therefore, a magnetic field in the toroidal direction only would lead to a vertical electric field and a particle loss due to $\vec{E} \times \vec{B}$-drifts on a short time scale. The poloidal magnetic field connects magnetically top and bottom of the device and short-circuits the separated charges.

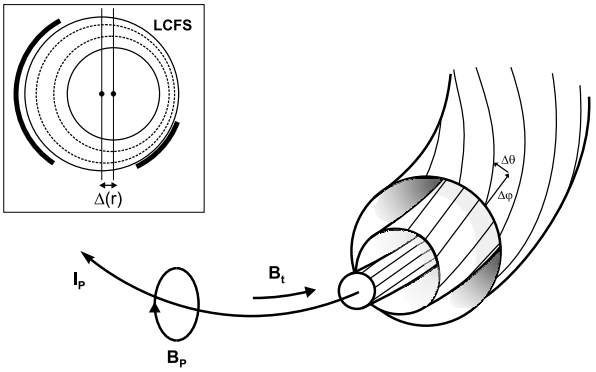

Figure 2.2: Helical field lines on nested flux surfaces shifted radially by $\Delta(r)$ due to Shafranov shift.

A tokamak device is capable to confine a plasma with plasma pressure $p = nk_BT$ (k_B: Boltzmann constant). As the magnetic pressure of the setup is technically limited, the ratio of plasma pressure and magnetic pressure (p_{mag}) represents a key value to describe the level of confinement achieved. The poloidal component can be written as:

$$\beta_{pol} = \frac{p}{p_{mag}^{pol}} = \frac{n \cdot k_B \cdot T}{B_p^2/(2\mu_0)} \tag{2.2}$$

In an idealized equilibrium state the pressure gradient is supported by a $\vec{j} \times \vec{B}$ force, which arises from the plasma current density $\vec{j}$ and the total magnetic field $\vec{B}$. From the magnetic equilibrium condition

$$\nabla p = \vec{j} \times \vec{B} \tag{2.3}$$

it follows in the axisymmetric case (by forming the scalar product of $\vec{j}$, $\vec{B}$ with Eq. 2.3) that both $\vec{j}$ and $\vec{B}$ are perpendicular to the pressure gradient ∇p. In other words, current and field lines span nested flux surfaces of constant pressure, constant total current and constant magnetic flux and are therefore called "flux surfaces" as illustrated in figure 2.2. The flux labels Ψ of flux surfaces are often used as equilibrium related, device independent, radial coordinate.
The difference in surface area of the flux surfaces at the HFS and LFS and the toroidal current result in a radial net outward directed force ("hoop force") which can be compensated by a $\vec{j} \times \vec{B}_v$ force with an additional vertical magnetic field B_v (compare figure 2.1). As a result, the radial pressure profile and therefore the flux surfaces get shifted radially outward by the *Shafranov shift* $\Delta(r)$. It scales with β and depends on the radius as sketched in figure 2.2. Hence, the parameters $q(r)$, β_{pol} and the plasma position define the plasma equilibrium.

2.1.2 Particle and Energy Exhaust: Limiter vs. Divertor concept

The exhaust of impurities within the plasma is a crucial factor for present and future fusion devices as an accumulation of impurities, e.g. helium ash from the fusion process, leads to a reduction of the fuel purity and hence the fusion reaction rate. Therefore, concepts had to be studied to control the particle and energy exhaust.
In the so-called Limiter-concept (figure 2.3a), suited obstacles – called "Limiter" – are introduced to the far plasma edge intersecting the closed flux surfaces. The position of the limiting wall with respect to the plasma position defines the last closed flux surface (LCFS) at the plasma radius $r = a$ (dashed line), which separates the plasma volume into two regions: In the core region at $r < a$ the plasma is confined on closed flux surfaces (grey). For $r > a$, so-called "open" field lines intersect the material wall and form the Scrape-off Layer (SOL) (yellow). The transport properties in these two regions are completely different: From the core region only cross-field transport carries particles and energy across the LCFS into the SOL. Inside the SOL, particles and energy are transferred to the wall as a perfect sink by dominantly fast transport parallel along the open field lines. The latter process implies that the radial extent of the SOL is small (typically in the order of millimeter). As a consequence, the plasma parameters such as density and temperature are reduced in the SOL and the radial gradients at the position of the LCFS steepen. At the limiter, ions and electrons recombine to neutrals and can be pumped away as they are not bound to the magnetic field anymore.
In limiter configuration there is a significant probability that neutralized particles re-enter the plasma. The penetration depth of a neutral particle into the plasma characterized by the individual ionization length of the species is typically in the order of $10^{-3} - 10^{-1}$ m so that particles, in particular impurities, can enter the plasma towards the core: the impurity screening capabilities in limiter configuration are small. It is therefore

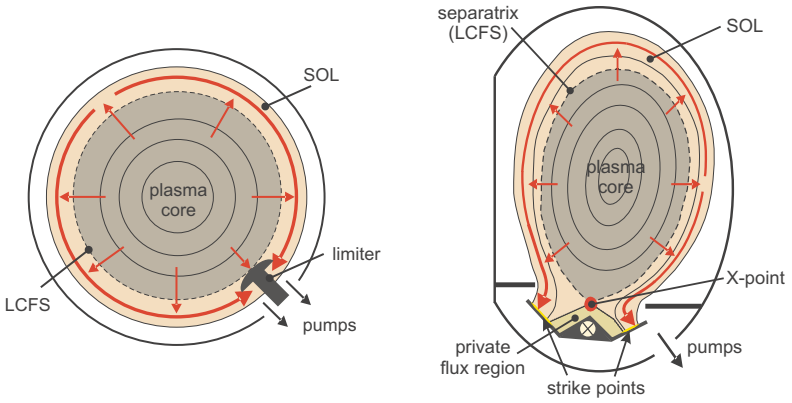

Figure 2.3: Sketch of a poloidal cut of a tokamak in limiter configuration (a) and divertor configuration (b).

advantageous to move the interaction zone between plasma and limiter spatially away from the confined volume, which is the basic idea of the so-called divertor concept [11].

The principle of the divertor concept is illustrated in figure 2.3b. An additional coil is placed inside the vacuum vessel in order to divert the outermost magnetic field lines into a separate chamber, the divertor, where they intersect the material divertor target plates. The coil with its current in parallel with the plasma current is placed in toroidal direction creating an additional poloidal field which cancels the resulting net poloidal field at the position of the so-called "X-point". The latter defines the separatrix (dashed line in figure 2.3b) which separates the SOL from the core plasma with closed flux surfaces. The position, where the separatrix strikes the divertor target plates is called strike lines or strike points. Between the inner and the outer strike point a region exists which is fully decoupled from both confined core plasma and SOL and is termed private flux region.

2.1.3 High Confinement Mode and Edge Instabilities (ELMs)

It was shown that with the introduction of the divertor concept an improvement of the confinement can be accessed, which was discovered first at the ASDEX tokamak [6]. Experiments in this so-called high confinement mode ("H-mode") are characterized by an increased energy confinement time by a factor of two than those obtained in the standard low confinement mode ("L-mode"), e.g. in the limiter scenario. It was shown that the H-mode scenario leads to a reduction of the transport in the plasma edge yielding a steepening of the radial edge pressure gradient and an improved particle and energy confinement. The reason for the formation of such a pedestal is under investigation but supposed to be related to a decorrelation of the edge fluctuations and therefore a reduced turbulent cross-field transport [12].

The H-mode regime in divertor tokamaks was shown to cause repetitive magneto-hydrodynamic (MHD) instabilities in the edge, called **E**dge **L**ocalized **M**odes (ELM) [7]. Characteristic for ELMs is that they lead to high transient heat and particle loads to the plasma facing components and therefore an increased erosion of the limiter material [13]. Present extrapolations toward ITER indicate that the enhanced wall erosion due to ELMs will reduce the life time of the first wall components to an unacceptable low level and reduce the plasma performance by enhanced impurity release [14]. Therefore, ELMs have to be mitigated or avoided in future fusion devices such as ITER.
The comparison between experiments and modeling approaches have carried out that the ELM can be described as an interplay between two MHD instabilities: the pressure gradient driven "ballooning" instability and the bootstrap current driven "peeling" instability [15]. A dedicated control of the edge pressure gradient to a level below the critical stability limit is therefore a possibility to control or suppress ELMs in present and future fusion devices.

2.2 ELM Control in High Confinement Plasmas by Resonant Magnetic Perturbations

It was shown at the DIII-D tokamak [10] that ELMs in H-mode plasmas can be suppressed by perturbing the equilibrium with the help of small, externally applied **R**esonant **M**agnetic **P**erturbation (RMP) fields [9]. They impose a complex magnetic topology, which depends on the coupling of the RMP field to the magnetic flux surfaces, their radial position and is therefore a function of β and $q(r)$. One working hypothesis is that the RMP imposed magnetic topology leads to a controlled change of the pedestal pressure gradient below the critical ballooning stability limit as the cause of ELM suppression. Therefore, a basic understanding of the plasma parameter changes arising due to the external RMP field is key to validate or disprove this hypothesis.

Figure 2.4 shows time traces of the electron density n_e, temperature T_e and the resulting electron pressure $p_e = n_e k_B T_e$ for a representative ELMy H-mode plasma at the DIII-D tokamak [16]. The static RMP field is applied from $t = 2.2 - 4.8\,\mathrm{s}$. Time traces are measured at the radial position of the pedestal with the normalized flux label $\Psi_N = 0.95$, where $\Psi_N = 1$ is defined to be the flux label of the separatrix. The edge safety factor q_{95} is governed externally which changes the coupling between the RMP field and the plasma and hence the resulting magnetic topology. Three phases are found during this scan, in which ELMs are suppressed for certain resonant q_{95} windows (shadowed area). The latter is detected by the peaking in the D_α recycling emission

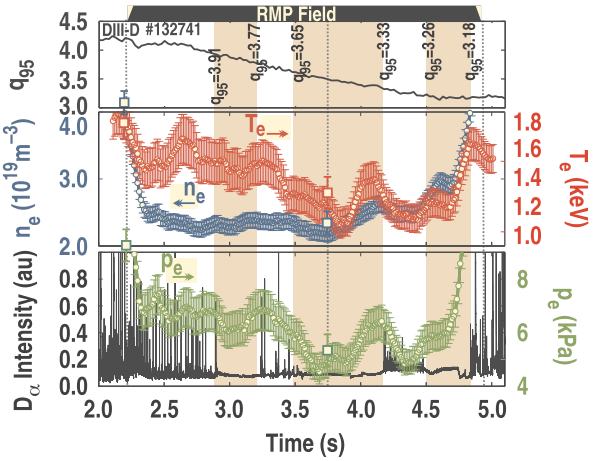

Figure 2.4: Pedestal time traces in DIII-D discharge #132741 with q_{95} ramp-down (from top to bottom): $q_{95}(t)$, $T_e(t)$, and $n_e(t)$ and the resulting $p_e(t)$ including the D_α-recycling emission light at the inner divertor strike line. ELM suppressed periods are marked with shaded boxes and the RMP period is indicated on top. The square markers show n_e, Te, and p_e values for a second discharge at fixed $q_{95} = 3.5$. The error bars shown are the fitting and statistical measurement uncertainties. [16]

detected in the divertor. The application of a static RMP field is found to lead to a pronounced drop in electron pressure p_e (green), which is dominantly caused by a reduction in the electron density n_e (blue), called particle pump-out. However, the measurement shows that a modulation of the electron temperature T_e (red) appears during the q_{95} scan, which causes a pressure modulation. The modulation indicates that an underlying magnetic topology exists which changes the energy and (weakly) the particle transport in the pedestal. One important aspect of the measurement is that the modulation in the pedestal plasma parameters does not correlate to the ELM suppression windows as it also appears in ELMy phases. This indicates that more detailed studies of both the plasma parameter distributions and their gradients are needed to quantify the working hypothesis for ELM suppression and the impact of RMP fields in general.

The experiment at complex H-mode plasmas at DIII-D motivates the experiments performed in the frame of this thesis to (a) understand the variation of the plasma edge parameters n_e, T_e and p_e and (b) to provide inversely information on the underlying edge magnetic topology.

Chapter 3

Experimental Setup

The experimental setup at the TEXTOR tokamak will be introduced in section 3.1. A new concept for plasma edge particle and energy control is realized by means of the *D*ynamic *E*rgodic *D*ivertor (DED) imposing a resonant magnetic perturbation field to the plasma. A description of its setup will be given in section 3.2.

3.1 TEXTOR Tokamak

The TEXTOR[1] tokamak [17] is operated at the Institute for Energy and Climate Research - Plasma Physics at the Research Center Jülich as part of the Trilateral Euregio Cluster. The main parameters and features are depicted in table 3.1. TEXTOR is a midsize tokamak designed in limiter configuration, i.e. without divertor. The particle and energy exhaust is arranged by a toroidal belt limiter (ALT-II), which can be used as the main limiter depending on the plasma position. Circular shaped plasmas are generated with plasma radii of $a = 0.45...0.47\,\mathrm{m}$ depending on the plasma position.
A total heating power of 9 MW is available by means of two neutral beam injectors (NBI), two pairs of ion-cyclotron-resonance heating antennae and one electron-cyclotron-resonance heating antenna. The two NBI are aligned to inject in the co- and counter-I_p direction and can be used to steer the plasma rotation by means of external torque input.

The coordinate system in terms of the toroidal angle ϕ and the poloidal angle Θ will be defined for the remainder of this thesis in the mathematical positive sense, i.e. counter-clockwise direction as shown in figure 2.1. For the standard configuration of the magnetic fields displayed, therefore, the magnetic fields B_t and B_p are counter-directed to the toroidal (ϕ) and poloidal (Θ) angles, respectively.

[1] TEXTOR - **T**orus **Ex**periment for **T**echnology **O**riented **R**esearch

major radius	$R = 1.75\,\mathrm{m}$
minor radius	$r = 0.46\,\mathrm{m}$
number of toroidal field coils	16
toroidal field	$B_t \leq 2.8\,\mathrm{T}$
plasma current	$I_p \leq 800\,\mathrm{kA}$
total heating power	max. 9 MW
external heating systems	2 neutral beam injectors (NBI) 2 ion-cyclotron-resonance-heating antennae (ICRH) 1 electron-cyclotron-resonance-heating antenna (ECRH)
type	limiter tokamak
limiter	ALT-II (limiter) poloidal limiter (top and bottom) DED target at high magnetic field side

Table 3.1: TEXTOR parameters and features

3.2 Resonant Magnetic Perturbations at TEXTOR: the Dynamic Ergodic Divertor

A flexible tool for investigation of *R*esonant *M*agnetic *P*erturbation (RMP) fields is available at TEXTOR – the **D**ynamic **E**rgodic **D**ivertor (DED) [18, 19].

Figure 3.1 shows a compositional photo of the Dynamic Ergodic Divertor consisting of 16 helical RMP coils (figure 3.1b). They are mounted in-vessel at the high magnetic field side of the TEXTOR chamber. For protection they are covered with graphite tiles – the DED target (figure 3.1a) located at a radial position of $r_t = 47.7\,\mathrm{cm}$ – in order

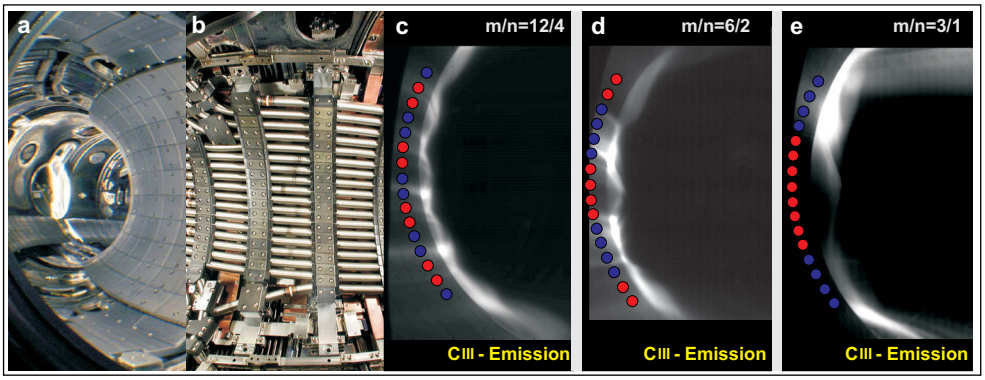

Figure 3.1: Photo composition of a view into the TEXTOR vessel onto the DED target limiter (a), the DED coils (b) and C-III emission during application of a static DED field in $m/n = 12/4$ base mode configuration (c). Figure (d) and (e) show the C-III emission for the $m/n = 6/2$ and $m/n = 3/1$ base mode configurations, respectively.

to withstand the local heat and particle loads. The helicity of the DED coils is aligned to the pitch angle of field lines at the rational $q = 3$ surface at the HFS. The main interaction zone is therefore given by a strong component which acts resonant at the radial position of the rational $q = 3$ surface.

The spectral composition of the RMP field can be changed externally in a flexible way. Three base mode configurations are featured: $m/n = 12/4, 6/2, 3/1$ with m, n being the poloidal and toroidal mode number. After $1/n$ toroidal or $1/m$ poloidal turns respectively the imposed structure appears to be same. The wiring of the coils to the power supplies and therefore the current distribution defines the base mode configuration as sketched in figure 3.1c-e in blue and red. Figure 3.1c shows the case, where each pair of neighboring coils are fed with an alternating current distribution ($m/n = 12/4$). In contrast, figures 3.1d-e show setups with sets of 4 and 8 coils fed in parallel ($m/n = 6/2, 3/1$). This results in a change of the spectral composition of the multipole magnetic field which leads experimentally to broader structures as seen by the C-III emission of recycling carbon released from the target in the vicinity of the DED coils.

Although the main resonance is given by the external setup, additional spectral components appear in each base mode configuration. As shown in figure 3.2 for the $m/n = 3/1$ base mode configuration, radial magnetic field components are also imposed with poloidal mode number $m \neq 3$ in a resonant way. In particular the strong $m = 2$ component can be utilized at TEXTOR to trigger externally a $m/n = 2/1$ tearing mode in the core plasma [20]. To avoid them, the perturbation level in terms of DED current has to be chosen below the critical excitation threshold. The strong side bands in the spectrum are caused in particular by two technical constraints: (a) For simplification, the feed throughs of the DED coils through the vacuum chamber are combined to sets of four DED coils each which causes an imperfect spectrum. As a consequence, a horizontal plasma displacement is needed to be compensated by a set of two additional compensation coils. (b) Misalignments of the DED coils leads to secondary spectral components of the RMP field.

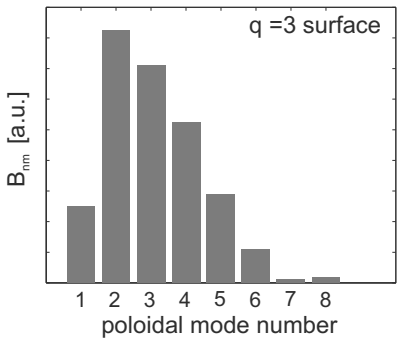

Figure 3.2: Spectrum of the DED induced radial magnetic field at the rational flux surface $q = 3$ in $m/n = 3/1$ base mode configuration. [19]

The DED is equipped with two power supplies feeding the DED coils without suffering the loss of flexibility. Historically, they are named $I_{DED}-1$ and $I_{DED}-5$. The maximum available coil currents are technically limited and depend in fact on the base mode chosen as listed in table 3.2. Additionally to constant coil currents (DC), the DED power supplies feature the application of currents with sinusoidal waveforms. Feeding the DED

DED base mode m/n	3/1	6/2	12/4
maximum current (DC)	3.75 kA	7.5 kA	15 kA
rotation frequencies (AC)	2 Hz ±1 kHz ±5 kHz	±1.38 kHz	±2 kHz ±7 kHz ±10 kHz

Table 3.2: DED parameters

coils or coils sets with sinusoidal currents, one shifted by $\pi/2$ to the neighbored one, leads to a rotation of the external resonant magnetic perturbation field with high rotation frequencies up to $\nu_{DED} = 10\,kHz$ depending on the DED base mode used (compare table 3.2). The sign of the relative phase between the currents of $\pm\pi/2$ defines the rotation direction of the DED field. For the remainder of this thesis, we define the helical AC(+) DED rotation direction in counter-B_p/counter-B_t direction respectively electron diamagnetic drift direction. The AC(-) rotation direction is defined in opposite direction and hence in B_p/B_t or ion diamagnetic drift direction. The resulting rotating magnetic fields for a certain spectral component m, n can be expressed with a time dependent phase as: $B \propto cos(m\Theta - n\phi \pm n \cdot 2\pi\nu_{RMP}t)$.

In order to measure the impact of rotating RMP fields imposed by the DED with high rotation frequencies on the plasma, high resolution diagnostics are needed which will be introduced in the next chapter 4. These measurements will be compared to the underlying DED induced magnetic topology, which is topic of chapter 5.

Chapter 4

Plasma Edge Diagnostics

In the frame of this work, fast rotating resonant magnetic perturbations (RMP) are used (a) to quantify their impact on the plasma edge and (b) as a diagnostic tool, to scan the rotating, i.e. locally time dependent, structure in the helical rotation direction of the RMP field. Therefore, a set of specially suited, high resolution diagnostics is used in order to quantify the edge plasma structure at different radial positions multi-dimensionally. Their toroidal positions in the TEXTOR vessel are indicated in figure 4.1.

A **gas-puff imaging system** (GPI, section 4.1) was installed in the frame of this work in order measure the poloidal and radial distribution of relative density fluctuations as a function of time with a high resolution. For a quantitative measurement of the

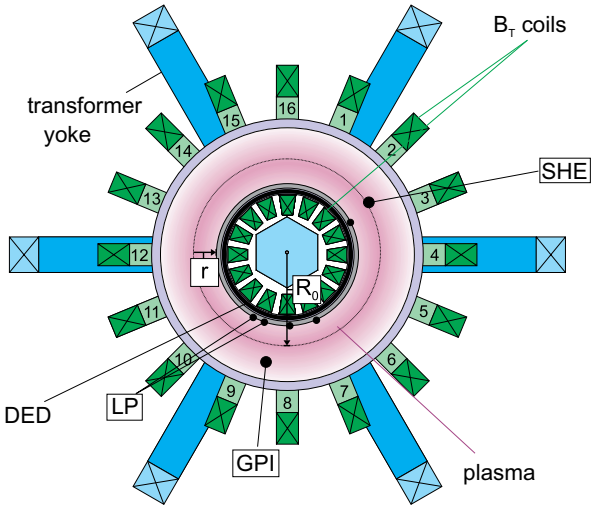

Figure 4.1: Top view onto the TEXTOR tokamak. The main parts and the diagnostics are marked: toroidal field coils (B_t coils), transformer yoke, Dynamic Ergodic Divertor (DED), minor and major radius (r, R_0), *S*upersonic *He*lium Beam (SHE), gas-puff imaging system (GPI) and Langmuir probe (LP) array.

radial and temporal electron density $n_e(r,t)$ and temperature $T_e(r,t)$ distributions, a **S**upersonic **He**lium Beam diagnostic (**SHE**, section 4.2) was improved toward high spatial and temporal resolution and established as a standard diagnostic at TEXTOR (see Refs. [21]). The plasma structure directly in front of the RMP coils is quantified by means of particle flux measurements at the DED target with the help of a set of toroidally distributed, high resolution **Langmuir Probes** (LP, section 4.3).

4.1 High Resolution Gas-Puff Imaging (GPI)

Gas-puff imaging (GPI) is a spectroscopic method for two dimensional measurements of the local plasma structure, which has been applied for instance in Alcator C-Mod [22, 23] and NSTX [24] tokamaks for high resolution turbulence measurements. We use this technique at TEXTOR to visualize the impact of the rotating DED field on the edge plasma for the first time. In section 4.1.1 the setup at TEXTOR will be described. Section 4.1.2 describes the relation of the measured quantities to the local plasma parameters.

4.1.1 Setup of GPI at TEXTOR

The setup consists of three parts: the gas puff system, the imaging optics and the detecting fast framing camera. The setup described here, utilizes a TEXTOR main gas inlet system, which is optimized for high duty cycles of $< 200\,\mathrm{Hz}$ with short rising and falling edges of $\approx 1\,\mathrm{ms}$. It is designed as a non-collimated, effusive source with an opening angle $\sphericalangle \approx 35°$ resulting in a cloud diameter of 14 cm at a radius of $r = 42\,\mathrm{cm}$

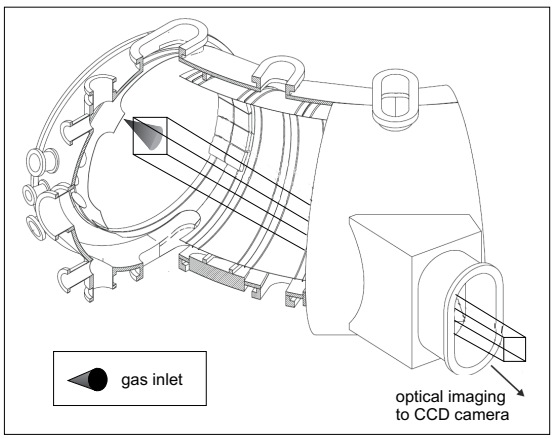

Figure 4.2: Perspective view into the TEXTOR vessel. The position of the gas cloud and the lines of sight are indicated.

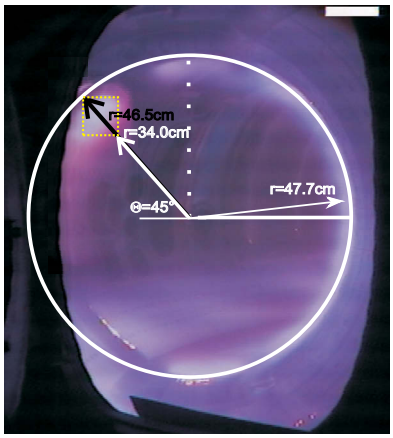

Figure 4.3: Color image of the overview camera. The observation area of the fast PSI5 camera is marked (yellow box).

for typical plasma parameters at TEXTOR. The toroidal and poloidal positions are $\phi = 180°$ and $\Theta = 45°$, respectively, at the low magnetic field side as shown in figure 4.2. The gas puff is imaged with a view perpendicular to the beam axis and tangential to the magnetic flux surfaces. This results in an integration of intensity along the line of sight in toroidal direction and a resolution of the gas puff in the radial and poloidal directions. The observation area of $18 \times 18\,\mathrm{cm}^2$ at the gas puff position is adjusted by a lens with a variable focal length of $50 - 500\,\mathrm{mm}$. Spectral wavelengths can be selected by means of different interference filters, here in particular with a wavelength of $\lambda = 656.3\,\mathrm{nm}$ and a width of $1.5\,\mathrm{nm}$ (FWHM) for hydrogen H_α emission. For detection of the emitted light a fast camera PSI5 developed by Princeton Scientific Instruments, Inc. is used with a frame rate of $< 500\,\mathrm{kHz}$ and a chip resolution of 64×64 pixel. This results in a spatial resolution at the gas puff position of $2 \times 2\,\mathrm{mm}^2$ per pixel. For a spatial cross-calibration of the observation area of the fast camera, a second slow camera measures at the same time the same spectral emission in a comparable tangential view over a complete poloidal cross-section. Figure 4.3 shows a color picture, here without spectral interference filter, with the spatial extension of the gas puff in the entire poloidal cross-section and the section the fast camera is looking at (yellow box). The spatial cross-calibration allows for an accurate allocation of the detection area of the PSI5 camera.

The specifications of the PSI5 camera are listed in table 4.1. It is equipped with an actively cooled CCD camera chip in order to decrease the thermal noise level. For a reduction of the storage time of the charges and hence to minimize the charge-transfer, each pixel of the chip consists of a photosensitive part and a covered storage part. It was found in Ref. [25] that the covering of the storage part is imperfect at the edges and that these "edge" frames suffer from post illumination. Therefore, the camera is equipped with a fast mechanical shutter with an opening/closure time of 10 ms, which represents the time of post illumination and limits therefore finally the usable frame rate of the camera. However, the setup enables for closing the valve coincident at the end of the measurement and avoids post illumination. Note that this issue occurs only for the edge frames, i.e. every 12th and 13th frame and diminishes for the setup described and a reduced frame rate of here $\leq 50\,\mathrm{kHz}$.

frame rate	$\leq 500\,\mathrm{kHz}$ (set to $50\,\mathrm{kHz}$ here)
spectral range	$\lambda = 300 - 1000\,\mathrm{nm}$
chip	64×64 pixel
pixel area	$200 \times 200\,\mu\mathrm{m}^2$
photo sensitive area	30.5%
storage	300 frames
well capacity	8400 counts
background noise level	800 counts
σ_{noise}	20 counts
working chip temperature	$-40°C$

Table 4.1: Main parameters of the PSI5 camera.

4.1.2 Electron Density Dependence of H_α Emission

Hydrogen was chosen as species for injection because the Balmer-α spectral line (H_α) in the visible wavelength range at $\lambda = 656.3\,\mathrm{nm}$ has its maximum emission for a wide range of plasma edge parameters at TEXTOR, i.e. electron density $2{\cdot}10^{18}\,m^{-3} \leq n_e \leq 1{\cdot}10^{19}\,m^{-3}$, electron temperature $20\,eV \leq T_e \leq 250\,eV$. The measured intensity depends on the population and depopulation of the hydrogen electronic state with principle quantum numbers $n = 3$ to the electronic state $n = 2$ which is a function of the local plasma parameters. The fluctuation level of the local H_α emissivity S_{H_α} within the beam is needed to be evaluated with a collisional radiative model based on atomic data of hydrogen atoms. With this approach, the injected hydrogen H_2 molecules are assumed to be fully dissociated at the given electron temperatures. In the collisional radiative approximation, S_{H_α} can be written as

$$S_{H_\alpha}(\mathrm{photons/m^3}) = n_0 f(n_e, T_e) A_{3\to2} \tag{4.1}$$

with the neutral particle density n_0 of the hydrogen atoms and the radiative decay rate (or Einstein coefficient) $A_{3\to2} = 4.41 \cdot 10^7\,\mathrm{s^{-1}}$ [26]. The function $f(n_e, T_e)$ summarizes the dependency of the emissivity on electron density and temperature based on modeling of the population of the $n = 3$ electronic state. The time scale for spontaneous emission of the spectral line once the atom has been excited is $1/A_{3\to2} = 0.02\,\mu\mathrm{s}$ and is a physical limitation of the temporal resolution of this method. However, the latter is much shorter than the technically realized resolution of $20\,\mu\mathrm{s}$ of the setup of the diagnostic.

In order to find $f(n_e, T_e)$, the excitation dominantly caused by electron-electron collisions, losses due to full ionization and depopulation by radiation have to be modeled numerically. We do not aim in the frame of this work on the modeling of the density and temperature dependence of the H_α emissivity but rely on results from the numerical database ADAS [27]. Figure 4.4 shows the emissivity S_{H_α}/n_0 normalized to the neutral density as a function of the electron density and temperature. The emissivity is found to depend on both n_e and T_e for temperatures $T_e < 40\,\mathrm{eV}$. For temperatures $T_e > 40\,\mathrm{eV}$, the emissivity is predominantly density dependent. At TEXTOR, this assumption is typically justified

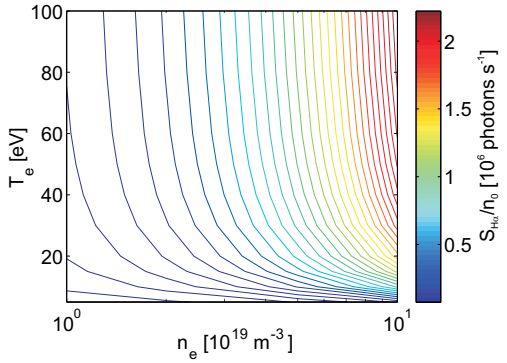

Figure 4.4: Contour plot of the normalized emissivity S_{H_α}/n_0 as a function of electron temperature T_e and density n_e.

inside of the last closed flux surface. Hence, the relative H_α intensity variations are equal relative density variations for TEXTOR edge plasmas with $T_e > 40\,\mathrm{eV}$:

$$\frac{I_{H_\alpha}(t) - \bar{I}_{H_\alpha}}{\bar{I}_{H_\alpha}} = \frac{n_e(t) - \bar{n}_e}{\bar{n}_e}. \tag{4.2}$$

In conclusion, the method described can be utilized to measure density variations with the GPI diagnostic with high temporal resolution.

4.2 Electron Density and Temperature Measured with a Supersonic Helium Beam

One specific method for measurements of the edge electron density n_e and temperature T_e in high temperature plasmas is Beam Emission Spectroscopy (BES) on thermal helium (He) [28, 29, 30, 31], in literature also known as He-I line-ratio technique. A beam of neutral helium atoms is injected into the plasma and gets excited and ionized by plasma electron and ion impact. The population densities of higher energetic states of the helium are determined by a balance of gain and loss processes, mainly due to electron collisions and spontaneous radiation with characteristic spectral wavelengths. The intensities of these spectral lines depend on the local plasma parameters. In measuring the radiation emission of suited transitions one can calculate n_e and T_e applying a collisional-radiative model (section 4.2.1), which is necessary to describe the physical processes for the existing conditions in the plasma edge of TEXTOR. This method is basis for all thermal helium diagnostics, which can be subdivided with respect to their source type with different divergence of the resulting beam. As the beam divergence defines the spatial resolution perpendicular to the beam axis due to line-of-sight integration, one has to deal with the two contrary requirements of as low as possible divergence but high helium density at the same time. While effusive and collimated sources, as e.g. installed at TEXTOR [30], have a divergence larger than ±10 degree, a more sophisticated approach represented by a supersonic beam source gives a beam divergence of typically ±1 degree and minimizes therefore the line-of-sight integration of the radiated emission. These kind of sources are realized at the H-1 heliac [32] and TJ-I UP/TJ-II experiments [33, 34] having a relatively low spatial and temporal resolution with respect to the setup presented here.

In the following, the setup and properties of a multi-pulse **S**upersonic **He**lium Beam diagnostic (SHE) installed at TEXTOR will be described, which was improved in the frame of this work to measure reliable n_e and T_e in the plasma edge with high spatial and temporal resolution. This requires a discussion of the applicability of the stationary Collisional Radiative Model to dynamic plasma conditions in section 4.2.1, which might limit the measurement of fluctuating n_e and T_e. A brief summary of the physical requirements of a supersonic source will be given in section 4.2.2. In sections 4.2.3 and 4.2.4 the initial setup will be described, characterized and compared to the new improved setup. Finally, we will demonstrate in section 4.2.5 the capabilities and reliability of the SHE diagnostic by proof of principle measurements.

4.2.1 Stationary Collisional Radiative Model and Application to Dynamic Processes

The **B**eam **E**mission **S**pectroscopy (BES) on thermal helium represents a reliable method to determine electron density n_e and temperature T_e in the range of $2.0 \cdot 10^{18}\,\mathrm{m}^{-3} < n_e < 2.0 \cdot 10^{19}\,\mathrm{m}^{-3}$ and $10\,\mathrm{eV} < T_e < 250\,\mathrm{eV}$ in the plasma edge [30].
The basis of the BES on helium is a **C**ollisional-**R**adiative **M**odel (CRM) [29, 35, 36]. It is based on the assumption that thermal helium atoms, which for temperatures below $1000\,K$ are mainly in the energetic ground state, are injected into a plasma with constant plasma parameter n_e and T_e. Due to collisions with plasma electrons helium atoms can be excited into higher energy levels and ionized. Induced by increasing population of the excited levels, further processes have to be considered to determine the amount of atoms in a specific electronic state. These processes are mainly electron collisions, spontaneous emission, ionization and charge exchange. From the analysis of the dominant processes in the given plasma parameter range, the charge exchange of helium with background gases [36] and the excitation by collisions with ions [30] can be neglected. However, depopulation by electron collisions is needed to be taken into account which forbids the application of a Corona model taken into account radiation only.
For each electronic state i the temporal development of the density population n_i can be calculated using a set of coupled partial differential equations (number of considered energy levels j), which include the rate coefficients of the involved processes (Eq. 4.3):

$$\begin{aligned}\frac{\partial}{\partial t} n_i = + \underbrace{\sum_{i,j\neq i} \langle \sigma_{ji} v \rangle n_e n_j}_{\text{gain by electron collisions}} - \underbrace{\sum_{i,j\neq i} \langle \sigma_{ij} v \rangle n_e n_i}_{\text{loss by electron collisions}} \\ + \underbrace{\sum_{j,j>i} A_{ji} n_j}_{\text{gain by spontaneous emission}} - \underbrace{\sum_{j,j<i} A_{ij} n_i}_{\text{loss by spontaneous emission}} \\ - \underbrace{\langle \sigma_{i,Ion} v \rangle n_e n_i}_{\text{loss by ionization}} \end{aligned} \tag{4.3}$$

with $\langle \sigma_{i,j} v \rangle$ being the rate coefficient and $A_{i,j}$ the Einstein coefficient for a specific transition $i \to j$. Within the CRM employed, equations 4.3 are solved for all electronic states with main quantum numbers $n \leq 6$ and therefore $i, j \in [0, 29]$ and the spectral line emission is calculated as a function of the local plasma electron density and temperature. The main feature of the CRM is that it accounts for the fact that the rate coefficients in the singlet and triplet system of helium processes depend on electron temperatures in a different way, i.e. achieving its maximum value at about $T_e = 200\,\mathrm{eV}$ and $T_e = 20\,\mathrm{eV}$, respectively. Therefore, a ratio of intensities from suited transitions of the singlet and the triplet systems is dominantly electron temperature dependent. For excitation from the ground state one expects only a weak temperature dependence for the population of excited levels with same quantum number in one energy system. However, the rate

coefficients for collisional transfer between these levels depend on the electron density. They generate a significant deviation of the population density in these energy levels. Because the intensity of the emission line is directly proportional to the density of a specific electronic state, the ratio of two spectral lines can also be dependent on electron density.

The method used as standard technique at TEXTOR applies the CRM for one transitions of the triplet system and two transitions of the singlet system of helium with the characteristic line emission with wavelengths:

$$\begin{aligned} \lambda_{3^1D\rightarrow 2^1P} &= 667.8\,nm \\ \lambda_{3^1S\rightarrow 2^1P} &= 728.1\,nm \\ \lambda_{3^3S\rightarrow 2^3P} &= 706.6\,nm. \end{aligned}$$

This set of spectral lines is chosen as they have a strong emission in the visible wavelength range which enables a simple optical setup of the diagnostic. Further more, the ratios of two of these lines are dominantly dependent on either the electron density or temperature over a wide range of edge plasma parameters at TEXTOR. However, the exact dependence is needed to be calculated by the CRM. The computed emission profiles are compared with the measured ones to determine inversely n_e and T_e in the range of $2.0 \cdot 10^{18}\,\mathrm{m}^{-3} < n_e < 2.0 \cdot 10^{19}\,\mathrm{m}^{-3}$ and $10\,\mathrm{eV} < T_e < 250\,\mathrm{eV}$. As a results of the CRM, figure 4.5 shows the calculated ratios for the emission ratios:

$$\text{solid line:} \quad \frac{I(\lambda = 728.1\,\mathrm{nm})}{I(\lambda = 706.5\,\mathrm{nm})} \quad (T_e\text{-sensitive})$$

$$\text{dashed line:} \quad \frac{I(\lambda = 667.8\,\mathrm{nm})}{I(\lambda = 728.1\,\mathrm{nm})} \quad (n_e\text{-sensitive})$$

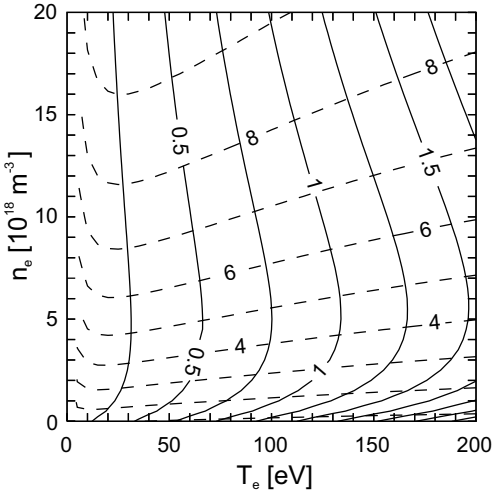

Figure 4.5: Intensity ratios as a function of n_e and T_e [36].

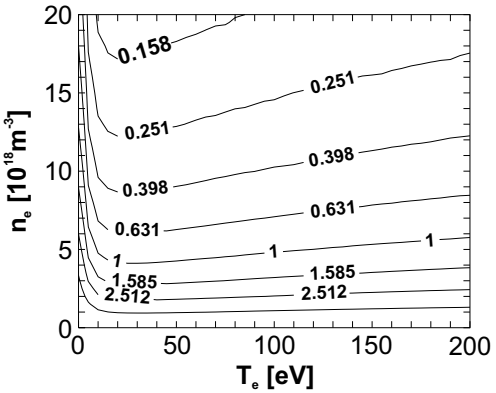

Figure 4.6: Contour lines of constant relaxation times in microseconds in the n_e-T_e-plane for the triplet system (2^3S), taken from [36].

Equation 4.3 enables to study the time dependence of the population of the electronic states. It was shown in Refs. [36, 35] that the population densities normalized by the ground state density approaches an equilibrium after a relaxation time τ. For these stationary conditions time independent solutions for the set of differential equations can be evaluated. This becomes important, if n_e and T_e variations take place on the same timescales, hence $n_e \cdot (dn_e/dt)^{-1} \approx \tau$ or $T_e \cdot (dT_e/dt)^{-1} \approx \tau$. As we will show in section 4.2.4, the SHE diagnostic allows for detecting electron density and temperature variations on a sub-100 μs time scale. Therefore, we show in the following that the stationary CRM is still valid for relaxation times being on time scales of the temporal resolution of the diagnostic in a limited parameter domain. As described in Refs. [36, 30], relaxation processes of the triplet system and hence in T_e are slower by one order of magnitude compared to the singlet system and therefore represent the lower limit. Figure 4.6 shows the relaxation time of the meta-stable triplet state 2^3S as a function of n_e and T_e (taken from [36]). A strong dependence of the relaxation time on T_e is observed for $T_e < 20\,\mathrm{eV}$. For $T_e > 20\,\mathrm{eV}$ a dependence of τ on n_e is found only and τ decreases with n_e. Minimal plasma parameters can be derived where the stationary CRM can still be applied. Beyond the parameter range effects due to non-relaxed states have to be taken into account and the stationary CRM is not valid anymore. For a relaxation time $\tau = \Delta t = 2\,\mu\mathrm{s}$, i.e. on order of magnitude larger than the technically achieved temporal resolution, we find for $T_e^{crit} > 20\,\mathrm{eV}$ a minimal electron density of $n_e^{crit} = 2 \cdot 10^{18}\mathrm{m}^{-3}$. The critical limit in n_e matches the general lower limitation of the CRM. Therefore, the stationary CRM can be applied for $T_e > 20\,\mathrm{eV}$ and relaxation effects can be neglected, which is true for all discharges discussed in the frame of this work.
However, for injected, i.e. moving helium, the relaxation time can be also seen as the time of flight for the helium atom until it gets into a relaxed state. This defines a characteristic length for relaxation and therefore the minimal radial resolution of the diagnostic. Considering a helium mean velocity of $\bar{v}_{He} = 1760\,\mathrm{m/s}$ [37], we get for low electron density of $n_e = 2{\cdot}10^{18}\,\mathrm{m}^{-3}$ and therefore a relaxation time of $\tau = 2\,\mu\mathrm{s}$ a relaxation length of 3.5 mm. This means that for low electron density the intensity integrated over

a smaller radial extent is lower due to unrelaxed states which is needed to be taken into account. The radial resolution of the detection system described in section 4.2.3 is 2 mm and therefore this is effect is needed to be taken into account for low electron densities, which are, however, not considered in the frame of this work.

4.2.2 Application of Supersonic Gas Injections

To get both a high temporal resolution and a high spatial resolution in the direction perpendicular to the beam axis (limited by line-of-sight integration), the injection system has to be optimized with respect to the two contrary requirements of low divergence and high neutral flux density at the same time. Both requirements are combined in the so-called skimmed supersonic gas injection systems.

The basic principle is sketched in figure 4.7. An adiabatic gas expansion from a high pressure (p_H) to a low pressure regime (p_0) with a high pressure difference of several orders of magnitudes leads to a supersonic expansion radially away from the nozzle. The physics attached to this is described in Refs. [38, 39, 40, 41, 42, 43, 44]. In summary, close to the nozzle the Mach number being the ratio of the mean velocity of the atoms to the sound speed exceeds one ($M = \bar{v}_{He}/c_s > 1$) and a Mach disk with $M = 1$ is formed, where no collisions between the atoms take place. This is only possible, because $c_s \propto \sqrt{T_0}$ is temperature dependent and decreases below the He mean velocity $\bar{v}_{He} = 1760\,\mathrm{m/s}$, which is only 40% higher than the thermal velocity. Near the Mach disk and in the region of $M < 1$, shock waves develop which lead to random velocity vectors due to collisions, i.e. the supersonic properties are lost. Here, the distance of the Mach disk to the nozzle x_{MN} compared to the nozzle diameter d depends on the pressure ratio: $x_{MN}/d = 0.67\sqrt{p_H/p_0}$. In this collision free region a Campargue type skimmer [39, 41] is placed to cut out the

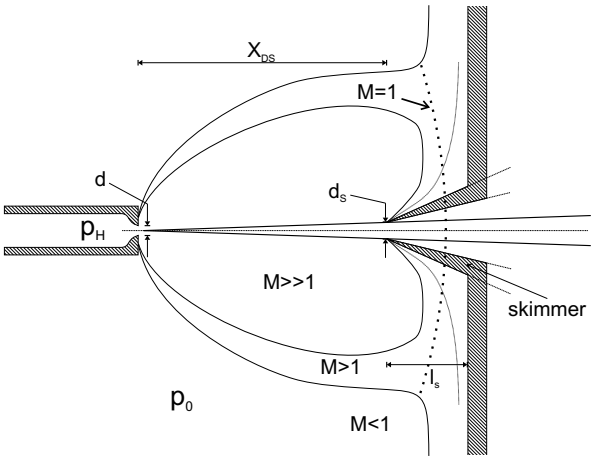

Figure 4.7: Sketch of a nozzle skimmer system with the regions divided by the beam Mach numbers. The Mach disk not perturbed by the skimmer is indicated by a dotted line.

atomic beam. As depicted in figure 4.7, the Mach disk itself will be deformed due to collisions of the atoms with the skimmer. To get the maximum beam intensity I_B, the nozzle skimmer distance x_{NS} has to be adjusted with respect to the pressure ratio p_H/p_0. There are two aspects reducing I_B by disturbing the beam by collisions: first, reduction by interference effects for small distances x_{NS} [41] and second, reduction by collisions with penetrating background atoms for x_{NS} near the Mach disk. Hence, it is reasonable that there must be an optimum position, which is at $x_{NS} \approx (0.6 - 0.7) \cdot x_{MN}$ [41].
The flux density Φ [45] of the resulting beam can be expressed by

$$\Phi = \frac{I_B \cdot \Omega}{A_B} = \frac{\kappa \cdot \Omega}{\pi \cdot A_B} \cdot \frac{dN}{dt} \tag{4.4}$$

with κ being the peaking factor describing the source efficiency comparing to an effusive source (typical $\kappa \approx 2$). The solid angle $\Omega = \pi/4 \cdot (d_S/x_{NS})^2$ and the cross-sectional area of the beam $A_B = \pi/4 \cdot w^2$ with the beam width w describe the geometrical properties of the circular beam. The helium flux dN/dt [37] for room temperature ($T_0 = 300\,\mathrm{K}$) before expansion calculated by

$$\frac{dN}{dt} = \dot{N} = 1.09 \cdot 10^{19} p_H \cdot d^2\,\mathrm{mbar}^{-1}\mathrm{mm}^{-2}\mathrm{s}^{-1} \tag{4.5}$$

defines finally the beam flux density Φ (with $[p_H] = \mathrm{mbar}$, $[d] = \mathrm{mm}$). Hence, Φ does not depend on the beam flow properties ($\kappa = const$) but on the helium particle flux dN/dt. It can be increased with p_H, which is technically limited to the pumping efficiency of the vacuum system to keep p_0 down.

4.2.3 Experimental Setup of the SHE

The Supersonic Helium Beam diagnostic described in detail in Refs. [37, 21] is installed at TEXTOR at a toroidal/poloidal position of $\phi = 315°$ and $\Theta = 80.5°$. The beam is injected vertically from top and the emitted light is imaged perpendicular to the beam axis onto the detection system. Here, the vertical axis z can be connected to the radial coordinate with $z = r \cdot sin(\Theta)$. The improved setup [21] of the supersonic gas injection system, the imaging and the detection system will described with respect to the initial setup [37] in the following.

Supersonic Beam Injection System The brief discussion of the physical concept in section 4.2.2 defines the technical requirements as basis for the initial setup. Three pressure volumes are needed to be separated: the high pressure (p_H) supply up to the nozzle, the low pressure (p_0) volume between nozzle and skimmer and the pressure in the TEXTOR vessel the beam is injected to. These three volumes are colored in the drawing in figure 4.8 showing the SHE setup at TEXTOR in a cross-sectional view. The low pressure volume (green) with the high pressure supply embedded (yellow/orange) can be separated from the TEXTOR vessel by a vertically movable slide-in port (purple). It can be retracted in order to decouple the entire diagnostic vacuum system from the TEXTOR

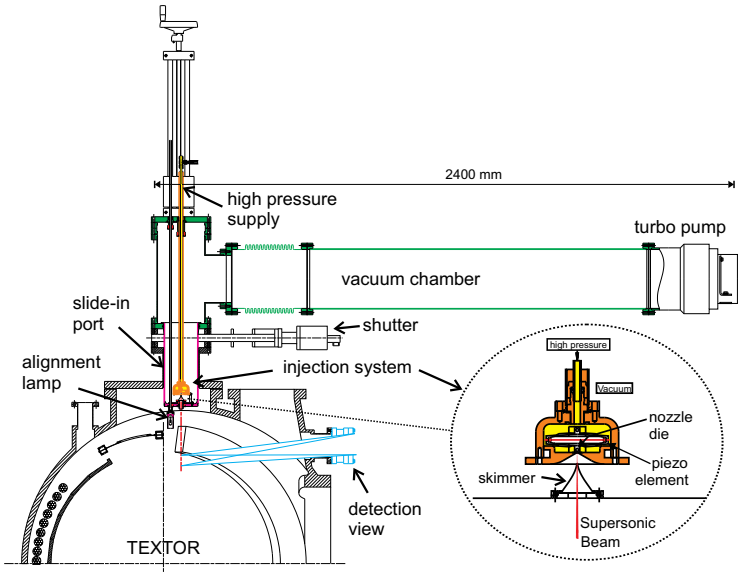

Figure 4.8: Technical drawing of the SHE diagnostic at TEXTOR with a zoomed insert of the valve skimmer system. Three pressure volumes can be identified: the TEXTOR vessel, the vacuum chamber (green) with the slide-in port (purple) and the high pressure volume (yellow/orange). The beam axis is highlighted red. The limiting lines of sight for detection from the window to the beam are marked in blue. [37]

vacuum by a gate valve.
First, we want to focus on the injection system itself, i.e. the nozzle skimmer system as shown in the zoomed picture of figure 4.8, which was improved in the frame of this work. A new copper skimmer (manufacturer: Beam Dynamics) with an opening of $d_s = 300\,\mu$m (see also figure 4.7) and a height of 25.4 mm replaces a skimmer of the initial setup with $d_s = 210\,\mu$m. It is placed in front of a nozzle at a distance of $\Delta x_{NS} = 14$ mm (before: $\Delta x_{NS} = 10$ mm). The nozzle itself consists of a new stainless steel plate with a central, laser drilled hole of 72 μm in diameter, which is less sensitive to blocking by impurities and improves therefore the system toward high reliability. The valve mechanism is based on a piezo element (PX 500, Piezosystem), which lifts a piston from the nozzle by 200 μm and acts as a valve. The repetition rate is limited to 40 Hz. As the piezo element suffers from temperatures above $70°C$, a passive cooling by the streaming helium is applied, which is cooled itself by compressed-air. During operation, the helium gas expands from the nozzle towards the skimmer into the low pressure volume. Here, the skimmer represents the only connection between the TEXTOR vacuum and the low pressure volume. Since the pumping efficiency of the system plays a key role in terms of repetition time and pulse duration (compare Eq. 4.5), we will focus in the following of the low pressure vacuum system.
The low pressure vacuum chamber with an overall volume of 165 l is pumped by a turbo drag pump (Pfeiffer, TMU 1600) with a throughput of $S = 1450$ l/s for helium and a powerful rotary pump (Leybold, Triviac D65B) with a throughput of $S = 18$ l/s. This

combination of pumps and volume reduces the pressure p_0 efficiently below 10^{-2} mbar during injection at a repetition rate of the gas puffs of 2 Hz and a pulse duration of 120 ms. The entire injection system is controlled remotely by a control unit (Simatic S5, Siemens) and monitored with the standard logger system at TEXTOR CAMAC [46].

Detection System The observation system is shown in figure 4.9 from top view. The upper right picture depicts the observation with respect to one sector of the TEXTOR vessel perpendicular to the beam, which is injected from the top (cp. also figure 4.8). As seen in more detail in the enlarged picture, the observation system with direct imaging optics consists of two independent detection subsystems, in the following called camera system and photomultiplier (PMT) system. Both are built up in a similar way and image the helium beam via a beam splitter within the optical path. Each subsystem is equipped with an array of dichroitic beam splitters reflecting the image wavelength dependent. The four preselected images are additionally filtered by narrow interference filters (FWHM 1.5 nm, manufacturer: Andover) according to the wavelengths described

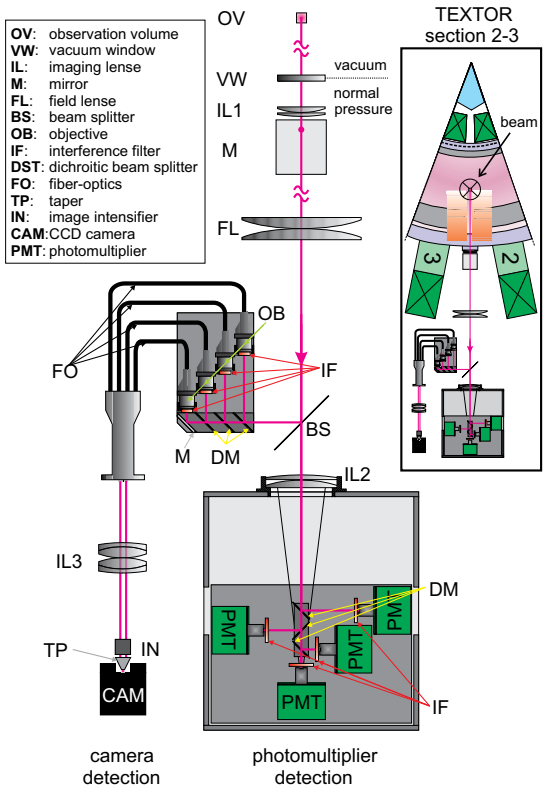

Figure 4.9: Sketch of the detection systems in top view [37]. The upper right picture shows the entire observation system with respect to the TEXTOR vessel - one sector is shown. The enlarged picture shows in detail the optics and detection setup.

in section 4.2.1 and are coupled to the detecting devices. For the camera system imaging fibre optics are used consisting of four light guides matrixes ($4 \times 4\,\mathrm{mm}^2$) which are united to one 2×2 matrix ($8 \times 8\,\mathrm{mm}^2$). This fiber matrix is projected via $1:1$ imaging optics on an image intensifier (S20 cathode, manufacturer: Proxitronic) and finally imaged by direct fiber coupling (Taper) to a CCD camera with a resolution of 256×256 pixel. This setup enables for measuring four spectrally separated images with one camera and one image intensifier at the same time. The spatial resolution of the camera subsystem of $\Delta r = 1.1\,\mathrm{mm}$ is limited by the optical setup.
The PMT subsystem is built up in a similar way using directly imaged multi-anode photomultipliers (H7260-20, manufacturer: Hamamatsu) instead of the camera. The photomultipliers consist of 32 linearly distributed channels with an interchannel spacing of 1 mm. Taking into account the optical magnification of $M = 0.5$ this corresponds to a radial extent imaged to the of the PMT system of $32 \times 2\,\mathrm{mm}$. In the toroidal direction the light is integrated over 14 mm as determined by the PMT channel width.

High bandwidth SMD readout electronics with a bandwidth of 400 kHz amplify and connect the PMTs with the digitizer. With respect to the maximum sampling rate of $f_{sampl} = 800\,\mathrm{kHz}$ of the digitizer, the entire bandwidth fulfills the Nyquist criterium. Figure 4.10 shows the readout electronics, which consists of current-voltage converters for each PMT channel, a patch panel as a flexible tool to select different channels and a multiplexer board. They are connected to 2×4 channel synchronized digitizer (E1564A, Agilent Technologies). The 4×1 multiplexer electronics enable for connecting remotely 8 of the 32 channels to the digitizer during a plasma discharge and hence to scan different radial positions from gas puff to gas puff (for example channels 1-8, 9-16, 17-24, 25-32). The flexibility of the system increases with the patch panel to preselect an individual configuration and connected it to the multiplexers.

In the frame of this work, the detection system was aligned toward maximum efficiency.

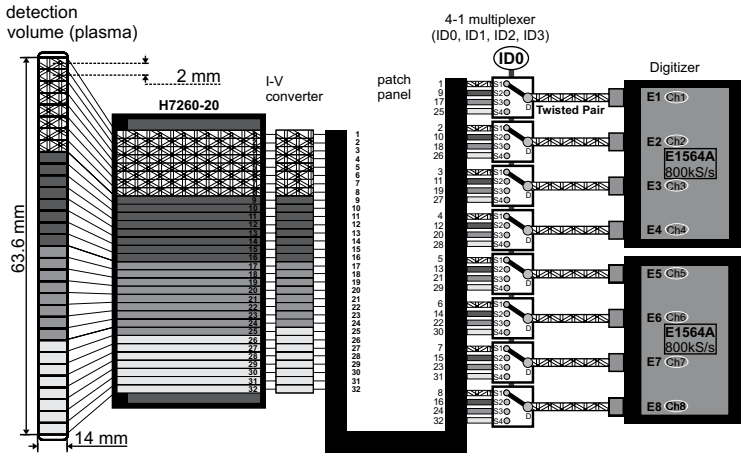

Figure 4.10: Read out electronics of the PMT signals including I-V converter and multiplexer board.

The digitizer system, in particular the data transfer into the central data base, was established in order to improve the SHE toward a reliable standard diagnostic at TEXTOR.

4.2.4 Spatial and Temporal Resolution of the SHE Diagnostic

Properties of the Injection System and Spatial Resolution In the following we compare the preliminary nozzle skimmer combination with a skimmer with $d_s = 210\,\mu$m and the optimized parameters $d = 40\,\mu$m and $x_{NS} = 10\,$mm to the improved setup with a new skimmer with $d_s = 300\,\mu$m and the optimized parameters $d = 72\,\mu$m and $x_{NS} = 14\,$mm. We discuss the beam properties with respect to beam divergence and neutral density. Figure 4.11 shows the intensity profiles of the cross-section of the helium beam for different combinations of pressure p_H and nozzle diameter d. They result in different helium fluxes $(dN/dt)_{nozzle}$ through the nozzle calculated with Eq. 4.5, which are shown in the legend. The intensity profiles are measured with the camera subsystem for the spectral line $\lambda = 668.7\,$nm during comparable TEXTOR discharges with identically plasma edge parameters. We will first focus on the preliminary setup (solid lines without markers). Here, the pressure p_H was varied linearly from 30 bar to 60 bar. As the beam shape is gaussian the full width at half maximum ($FHWM = w$) can be determined and decreases from $w(p_H = 40\,\text{bar}) = 12.1\,$mm to $w(p_H = 60\,\text{bar}) = 9.7\,$mm. This decrease is compatible with increasing shift of the Mach disk $x_{NS} \propto \sqrt{p_H/p_0}$ and indicates that the beam is perturbed by background atoms for low values of p_H. This effect is confirmed by comparing the absolute beam width with the theoretically expected one of $w_{geom} = 5.7\,$mm, which is larger by a factor of two. A calculation of the theoretical

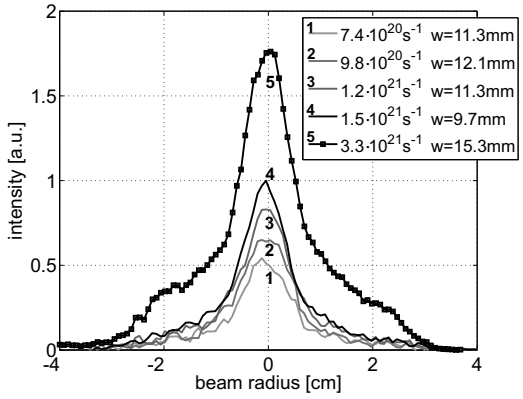

Figure 4.11: Beam profiles perpendicular to the injection direction for two skimmer nozzle combinations and helium fluxes $(dN/dt)_{nozzle}$ (see Eq. 4.5) measured by He emission ($\lambda = 668.7\,$nm, #100700, #100703, #100705, #100707, #110154). The solid lines without markers (1-4) show the profile with the preliminary nozzle skimmer set up. The black line with markers (□, 5) show the intensity profile for the improved nozzle skimmer combination.

position of the Mach disk of $x_{MN}^{th} \approx 6.6\,\text{mm}$ (section 4.2.3) shows that the experimentally determined skimmer position of $x_{NS} = 10\,\text{mm}$ is outside the Mach disk and therefore influenced by collisions.
In addition, it can be seen in figure 4.11 that the measured intensity and hence the helium flux of the beam increases linearly with p_H. Therefore the optimum operating parameters were found to be $p_H = 60\,\text{bar}$ resulting in a beam width of $w = 9.7\,\text{mm}$. This width corresponds to a beam divergence of $\sphericalangle = \pm 1°$. The particle flux into TEXTOR for this optimized parameters was measured by quadrupole mass spectroscopy and determined to $\dot{N}_{TEXTOR} = 1.7 \cdot 10^{17}\,\text{s}^{-1}$ [37]. Taking into account the helium atoms mean velocity of $\bar{v}_{He} = 1760\,m/s$ [37] and the cross-sectional beam area $A_B = \pi/4 \cdot w^2 = 74\,\text{mm}^2$, a beam density of $n_0 = \dot{N}_{TEXTOR}/(A_B \cdot \bar{v}_{He}) = 1.3 \cdot 10^{18}\,\text{m}^{-3}$ and an atomic beam flux density of $\Phi_{TEXTOR} = \dot{N}_{TEXTOR}/A_B = 2.3 \cdot 10^{21}\,s^{-1}\text{m}^{-2}$ is achieved. In comparison with Eq. 4.4 the measured beam flux is two times lower than the theoretically expected one of $\Phi^{th} = 4.5 \cdot 10^{21}\,\text{s}^{-1}\text{m}^{-2}$. This effect can be caused by the imperfect manufactured skimmer opening, which cannot be inspected due to its small scale.

The cross-sectional beam profile for the improved nozzle skimmer setup is shown in figure 4.11 by the black curve with markers (□, 5). The maximum intensity and therefore beam flux is increased by 85% as the flux through the nozzle dN/dt is increased by a factor 2.2. The new setup leads to a beam density of $n_0 = 1.0 \cdot 10^{18}\,\text{m}^{-3}$ resulting in a beam flux of $\dot{N}_{TEXTOR} = 3.2 \cdot 10^{17}\,\text{s}^{-1}$ and a width of $w = 15.3\,\text{mm}$, i.e. a divergence of $\sphericalangle \pm 1.6°$. The actual setup leads to shoulders, which can be connected to collisions with background atoms. This effect is discussed in detail in Ref. [37] as one explanation. The reduced pressure ratio of $p_H/p_0 = 40/10^{-5}\,\text{bar/bar}$ leads theoretically to a smaller distance x_{NS} between nozzle and skimmer. Hence, collisions with background atoms behind the Mach disk becomes more important, which might explain the shoulders.
In summary, the improvements of the nozzle skimmer system implemented in the frame of this work were shown to lead to an increased beam flux by 85%. The divergence of $\sphericalangle \pm 1.6°$ and therefore the line-of-sight integration is acceptable low below the spatial extent of the plasma structures to be resolved.

Temporal Resolution of the Injection and Detection Systems The temporal resolution of the SHE diagnostic depends on the beam flux, the aperture and transmission of the optics and the quantum efficiency of the PMTs. Without quantifying the efficiency of each component separately, we use here the method proposed in Ref. [47] in order to characterize the entire system. We will apply this method for the improved setup and compare the temporal resolution obtained to the one of the old setup obtained in Ref. [37]. The method compares the fraction of photon noise to the measured signal. We can assume that a signal detected with the full sampling rate of $f_{sampling} = 800\,\text{kHz}$ is totally dominated by photon noise. The standard deviation of such an intensity signal with pure photon noise satisfies the Poisson statistics - hence obeys $\sigma(I) = \sqrt{I}$. Here, the intensity depends on the number of photo electrons integrated during the time δt. Therefore, the intensity is the product of the photo electron flux $\dot{N}_{pe}$ and the integration time and the standard deviation can be written as: $\sigma(I) = \sqrt{\dot{N}_{pe} \cdot \delta t}$. In the logarithmic presentation the standard deviation relative to the intensity mean value $\sigma(I)/\bar{I}$ appears as straight

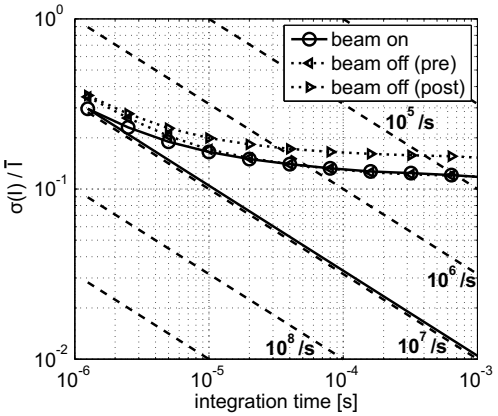

Figure 4.12: Standard deviation normalized to the mean value ($\sigma(I)/\bar{I}$) of the He-beam intensity (solid line, ∘) as a function of the integration time for discharge #110233 (1.6171 − 1.7369 s, $z = 44.8$ cm). Additionally, $\sigma(I)/\bar{I}$ is shown for passive background signals before and after the active beam phase (dotted lines, ▷/◁). Dashed lines indicate $\sigma(I)/\bar{I}$ of Poisson noise of constant photon flux.

lines as shown in figure 4.12 (dashed lines). Each difference to this square root behavior is supposed to be external and hence from the plasma. Figure 4.12 shows the relative variance of the active (beam on - ∘) and passive measured signal (beam off - ▷/◁) as a function of the integration time for the weakest observed wavelength $\lambda = 728$ nm, which limits finally the temporal resolution of n_e and T_e. For the lowest integration time of $\delta t = 1.25\,\mu$s the curves approach the square root behavior of Poisson noise. The latter is displayed as the solid line without marker. In this limit the measured photo electron flux for the active beam phase can be determined to $\dot{N}_{pe} = (9.1 \pm 0.1) \cdot 10^6\,\mathrm{s}^{-1}$. The photo electron flux for the passive signal (beam off) is lower as expected but different before and after the active beam phase which means that the signal fluctuation must have changed. Comparing now for the active signal the fraction of poisson noise on the total signal, a significant signal level with $\sigma_{PMT}/\bar{I} = 2 \cdot \sigma_{Poisson}/\bar{I}$ is reached for an integration time of $\delta t \geq 20\,\mu$s. Therefore, the temporal resolution in terms of the integration time is limited to $f^{max} = 1/\delta t = 50$ kHz, which is a factor of 5 higher than the one obtained with the initial setup proposed in Ref. [37].

4.2.5 Highly Resolved SHE Measurements and Comparison to Standard Diagnostic at TEXTOR

In order to show the reliability of the SHE diagnostic, we exemplarily compare radial n_e and T_e profiles with data from an effusive helium beam diagnostic [30]. Figure 4.13 shows radial profiles of n_e and T_e measured with the SHE diagnostic and averaged over an active beam phase of $\Delta t = 120$ ms. The error bars are calculated from the statistical variations of the intensity profiles within Δt and are applied to the CRM to determine

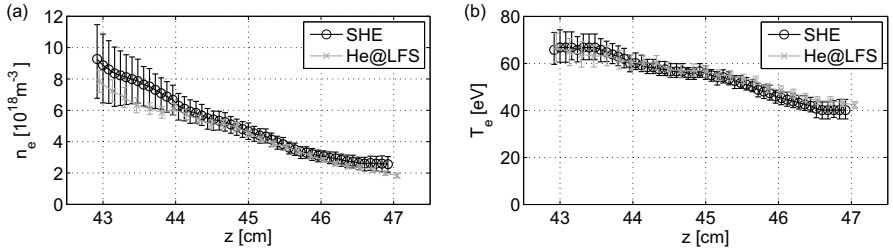

Figure 4.13: Radial profiles of (a) electron density and (b) temperature (averaged over $t = 2.1202 - 2.2412\,\mathrm{s}$) measured with the SHE diagnostic (black ∘) and a standard He diagnostic (grey, ×) for discharge #105293.

the errors in n_e and T_e. However, the systematic errors of the CRM of $\Delta n_e^{CRM} = \pm 10\%$ and $\Delta T_e^{CRM} = \pm 30\%$ [36] are not included. They are estimated by comparing the data to measurements of other diagnostics [30] and are mainly caused by imprecise atomic data.
The profiles in figure 4.13 are compared to the ones measured by an effusive helium beam diagnostic for a representative standard TEXTOR plasma. As the diagnostics are mounted at different poloidal and toroidal positions, the data are mapped via a circular magneto-hydrodynamic equilibrium to the SHE measurement position. With this technique we utilize the fact that the plasma pressure is constant on a flux surface and thus independent from the toroidal and poloidal position. However, it is important to note that the electron density and temperature can be different due to local effects at the individual measurement position. The radial distributions of both n_e and T_e in figure 4.13 are found to be in good agreement within the statistical errors. Small differences are caused by local plasma effects at the different measurement positions.

Figure 4.14 shows highly resolved $n_e(t)$ and $T_e(t)$ time traces measured with the PMT subsystem. In this discharge, a rotating resonant magnetic perturbation field with 1 kHz rotation frequency is imposed to the plasma, which leads in fact to a modulation of both plasma parameters and demonstrates the high time resolution capabilities of the SHE diagnostic. The signals shown are not only determined by the modulation of the rotating

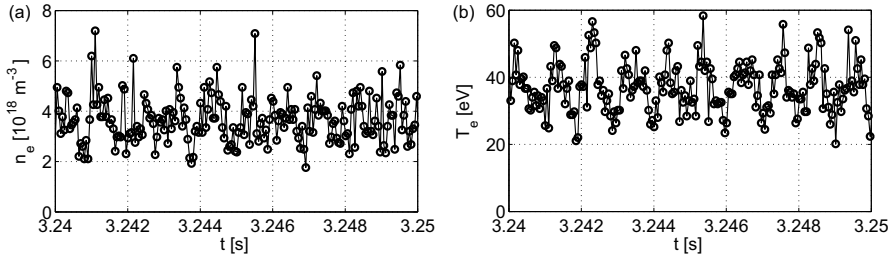

Figure 4.14: Electron density (a) and temperature (b) time traces of discharge #104741 measured with the SHE diagnostic at the position $z = 45\,cm$.

RMP fields, but also include variations due to e.g. other physical phenomena or statistical noise. Therefore, we will take advantage of additional evaluation methods described in section 4.4.

4.3 Particle Flux Measurements with Langmuir Probes in Front of the DED coils

A Langmuir probe represents an electrode, which is biased against the plasma potential V_p and exposed to the plasma [48]. The plasma potential V_p as plasma related quantity is not accessible as a reference potential. Therefore, the machine or vessel grounding is often used instead as the common base potential. The schematic principle of the wiring of a Langmuir probe with one electrode - a single Langmuir probe - is shown in figure 4.15a. The current I_{LP} through the circuit can be measured as a function of the applied variable biasing voltage V_{LP} and gives a characteristic current-voltage distribution as shown exemplary in figure 4.15b. It depends on the plasma related parameters $I_{i/e,sat}$ (ion/electron saturation current) and V_p (plasma potential), which allow for calculating the ion and electron fluxes to the probe, the local plasma density and temperature. For an applied voltage equal the so-called floating potential $V_{LP} = V_f$ the ion currents compensate the electron currents and the measured net current is $I_{LP} = 0$. For a negative voltages $V_{LP} \ll 0$ (region I in figure 4.15b), a strong potential barrier is created, which prevent electrons to reach the probe. Therefore, I_{LP} is fully determined by the ion current, the so-called ion saturation current $I_{i,sat}$. Ions move with sound speed c_s toward the probe head and the ion saturation current is then:

$$I_{i,sat} = e \cdot \Gamma_i \cdot A_{LP} = enc_s A_{LP} \tag{4.6}$$

with Γ_i being the ion flux on the probe, e the electron charge and n the density. In this simplified approach, A_{LP} represents the surface area of a planar probe reduces without taking into account the probe orientation with respect to magnetic fields. The thermal

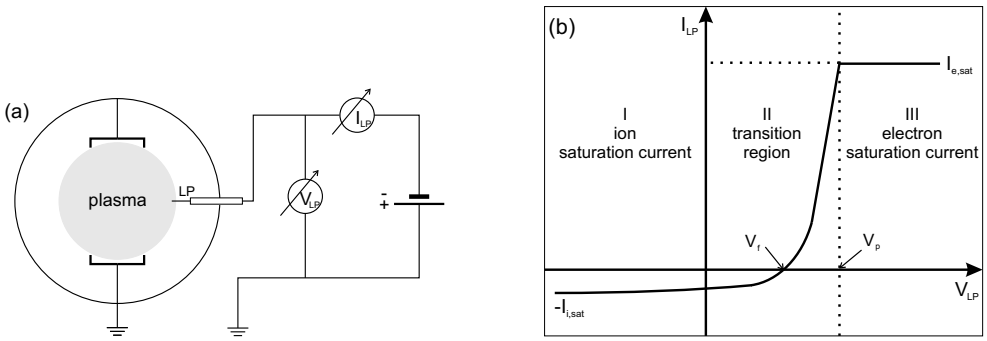

Figure 4.15: Principle (a) and current-voltage characteristics (b) of a single Langmuir probe. (derived from [48])

sound speed c_s

$$c_s = \sqrt{\frac{k_B(T_e + T_i)}{m_i}} \tag{4.7}$$

depends on the electron and ion temperatures T_e and T_i, the ion mass m_i and the Boltzmann constant k_B. Hence, this probe modus allows to measure the ion flux Γ_i on the Langmuir probe locally.
For an applied biasing voltage of $V_{LP} > V_p$ (region III of figure 4.15b), ions are fully repelled due to a positive potential barrier and the electron saturation current $I_{e,sat}$ and therefore the electron flux Γ_e is measured. The actual evolution of $I_{LP}(V_{LP})$ depends on the geometry of the probe area, which is planar here.
For biasing voltages $0 < V_{LP} < V_p$ (region II), the electrons are assumed to follow a Maxwellian velocity distribution.

$$I_e = I_{e,sat} \cdot \exp\left(\frac{e(V_{LP} - V_p)}{k_B T_e}\right) \tag{4.8}$$

The electron saturation current scales with the ion saturation current and the reduced mass:

$$\frac{I_{e,sat}}{I_{i,sat}} = \sqrt{\frac{m_i}{m_e}}. \tag{4.9}$$

Hence, we can write the total measured probe current $I_{LP} = I_e + I_i$ with the help of Eq. 4.8 as

$$I_{LP} = -I_{i,sat} + I_{i,sat} \cdot \sqrt{\frac{m_i}{m_e}} \cdot \exp\left(\frac{e(V_{LP} - V_p)}{k_B T_e}\right) \tag{4.10}$$

Equation 4.10 reproduces the evolution of the current in region II and enables for determining the plasma potential and the electron temperature. In the lower limit of $V_{LP} \ll 0$ evidently the ion saturation is reproduced.

At TEXTOR, a set of five single Langmuir probes is operational at present as standard diagnostic, which are mounted at the HFS at the DED target plates in the vicinity of the RMP coils at different toroidal positions (compare figure 4.16). The poloidal angle for all is $\Theta = 186.2°$ and the radial position $r = 47.7\,\mathrm{cm}$. The probes cover a wide toroidal range with $\phi = 172.3°, 176.5°, 194.8°, 210.2°, 307.0°$. They allow for a two-dimensional study of the near field plasma structure imposed by the rotating RMP fields in terms of $\Gamma_i(\phi, t)$, i.e. in the toroidal and the rotation direction of the DED field.

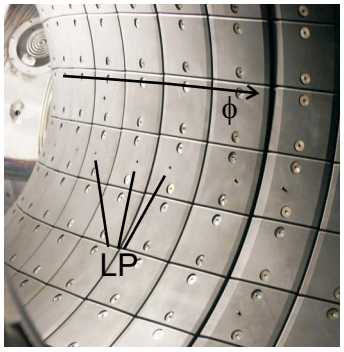

Figure 4.16: Photo of Langmuir probes (LP) mounted at the DED target at TEXTOR.

4.4 Data Evaluation Methods: Conditional Averaging and Cross-Correlation

Two evaluation methods have been applied in the frame of this work, the **conditional averaging** and **cross-correlation** technique.

Conditional Averaging can be used for signals, which contain a periodic modulation with a fixed and known frequency ν to emphasize the periodic component with multiples of ν. We assume a time dependent sinusoidal function $S(t)$ sampled in steps of $t_{i+1} - t_i$:

$$S_i(t_i) = A \cdot sin(2\pi\nu t_i) + f(t_i) \tag{4.11}$$

The amplitude A might contain noise but is larger than the function $f(t_i)$, which represents parasitic non-periodic or periodic functions with different frequencies than ν. The sampling rate of the signal $f_s = 1/(t_{i+1} - t_i) \gg \nu$ is larger than the modulation of the signal to resolve the modulation.
The signal can be subdivided into parts of the length $l = f_s/\nu$ of one period. The period time τ is then given by:

$$\tau = 1/\nu. \tag{4.12}$$

Each part with indices $k = i$ MOD l contains one period only and can be averaged for same indices k. This method applied for many periods $N \gg 1$ averages all components of the signal and therefore reduces noise and parasitic components by $1/\sqrt{N}$.

As an example, we recall figure 4.14, where density and temperature time traces measured by the SHE diagnostic during application of a fast rotating DED field was shown. The rotation frequency of the DED field is $\nu_{DED} = 974\,\mathrm{Hz}$. The period time given by Eq. 4.12 is $\tau_{DED} = 1.027\,\mathrm{ms}$. The result of the application of the conditional averaging method for these signals $n_e(t)$ and $T_e(t)$ for 40 periods is shown in figure 4.17 and two averaged periods ($2 \cdot \tau_{DED}$) are displayed. A clear modulation of both n_e and T_e gets visible, which is perturbed in the raw signal by superposed periodic or non-periodic fluctuations caused by the plasma and noise.

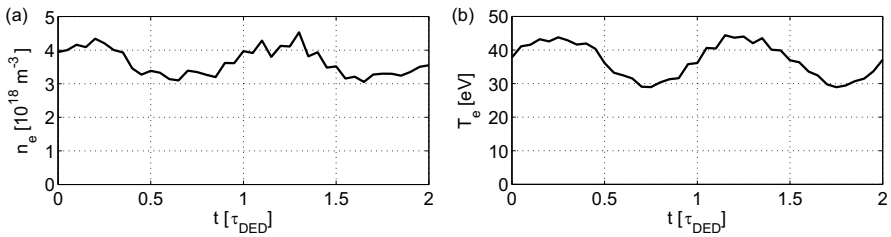

Figure 4.17: Conditional averaged electron density (a) and temperature (b) time traces of discharge #104741 measured with the SHE diagnostic at the position $z = 45\,cm$ at $t = 3.2401 - 3.2812\,\mathrm{s}$.

The Correlation Function $\Phi_{fg}(T)$ of two functions $f(t)$ and $g(t)$ [49] is defined as

$$\Phi_{fg}(T) = \int_{-\infty}^{\infty} f(t)g(t+T)dt \tag{4.13}$$

and for time-discrete signals:

$$\Phi_{fg}^{j} = \frac{1}{N-j} \sum_{k=0}^{N-1-j} f_k g_{k+j}. \tag{4.14}$$

For $f = g$, equations 4.13 and 4.14 describe the auto-correlation function, which is peaked at $T = 0$. For two functions $f \neq g$, $\Phi_{fg}(T)$ is called cross-correlation function. It is zero for uncorrelated signals and gets peaked for correlated phase-shifted signals. Figure 4.18 shows an example of two correlated signals shifted by $\Delta t = 10\mu$s. The peak position of the cross-correlation function is at $T = \Delta t$. This method was used in the frame of this work to determine the phase shift $2\pi T/\tau$ for periodic signals with a period time τ.

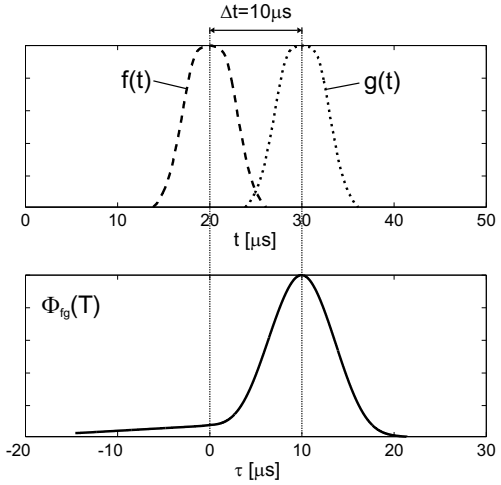

Figure 4.18: Two correlated signals phase-shifted by $\Delta t = 10\mu$s and cross-correlation function $\Phi_{fg}(T)$

Chapter 5

Perturbed Magnetic Topology at TEXTOR and Plasma Response

The formation of the DED induced magnetic topology at TEXTOR is of particular interest in this thesis. One attempt to model the magnetic topology represents the linear superposition of the external Resonant Magnetic Perturbation (RMP) field with the unperturbed magneto-hydrodynamic (MHD) equilibrium. This approach, the so-called vacuum approximation, allows to calculate the magnetic topology as described in sections 5.1 and 5.2. Three-dimensional transport models allow to calculate the resulting distribution of plasma parameters in this magnetic topology. In the frame of this work, the EMC3-EIRENE model is used which will be introduced briefly in section 5.3. However, this approach neglects changes of the basic equilibrium due to the RMP field and a possible feedback of the plasma due to internal plasma response currents. The latter result in additional internal magnetic fields, which weaken or screen the external field and therefore change the magnetic topology. In section 5.4 we will summarize experimental findings with static RMP fields, which support that the internal plasma response is negligible in highly resistive edge plasmas. With decreasing resistivity, i.e. toward the plasma core, any external perturbation is screened by a counter-acting internal plasma response current, which can be described with ideal plasma response MHD models for zero resistivity. It is reasonable that a layer with intermediate resistivity must exist, where both approaches fail. In section 5.5, a more complete approach to model the coupling of external RMP fields to the plasma is described by means of a 4-field drift fluid model, which includes internal plasma response self-consistently as a function of the plasma parameters such as resistivity and pressure gradient.

5.1 Field Line Tracing in Vacuum Approximation in High Resistivity Plasmas

For analysis of the magnetic topology imposed by the DED, field line tracing [50, 51, 18] is used as a basic approach in the frame of this thesis. A three-dimensional vector $\vec{x}(s)$ can be introduced in such a way that $\vec{x}(s)$ represents the position vector along a path s of field lines, hence,

$$\frac{d\vec{x}}{ds} = \frac{\vec{B}}{|\vec{B}|}. \tag{5.1}$$

For a given total magnetic field $\vec{B}(\vec{x}(s))$, the solution of Eq. 5.1 for each point describes a three-dimensional path of the magnetic field line $\vec{x}(s)$. It is convenient to choose generalized coordinates instead of geometrical coordinates r, Θ, ϕ as being the radial, poloidal and toroidal coordinate, respectively. The intrinsic so-called *Clebsch* coordinates (Ψ, θ, ϕ) are employed with the toroidal angle ϕ, the intrinsic poloidal coordinate θ, which is basically the transformed geometrical poloidal angle Θ and finally the magnetic flux label Ψ representing the radial direction. The latter represents the toroidal magnetic flux through a poloidal plane perpendicular to the magnetic axis with $\Psi = 0$ per definition.

Introducing the poloidal magnetic flux H, the total magnetic field can be expressed as a divergence free vector field:

$$\vec{B} = \nabla\Psi \times \theta + \nabla\phi \times \nabla H(\Psi, \theta, \phi). \tag{5.2}$$

Taking into account Eq. 5.1, we can derive a new set of equations describing the magnetic topology in Hamiltonian form [50]:

$$\frac{d\Psi}{d\phi} = -\frac{\partial H}{\partial \theta}, \quad \frac{d\theta}{d\phi} = \frac{\partial H}{\partial \Psi}. \tag{5.3}$$

For a non-perturbed axisymmetric tokamak plasma, the Hamiltonian function $H(\Psi, \theta, \phi)$ is independent of ϕ and the Hamiltonian system described by Eq. 5.3 is completely integrable. With θ being a function of the safety factor profile $q(\Psi)$ as $\theta = \phi/q(\Psi) + \theta_0$, $H(\Psi)$ remains only dependent on the radial flux coordinate Ψ. As a result for the unperturbed case, field lines lay on nested toroidal flux surfaces determined by the function $H_0 = H(\Psi)$.

A small periodic, resonant magnetic perturbation fields can be applied by adding a perturbation term H_1 to the static equilibrium term H_0:

$$H = H_0(\Psi) + \epsilon H_1(\Psi, \theta, \phi). \tag{5.4}$$

The dimensionless parameter ϵ scales the strength or amplitude of the perturbation term H_1, which can be expressed as a series of periodic trigonometric functions with the poloidal mode number m and the toroidal mode number n:

$$H_1(\Psi, \theta, \phi) = \sum_{m,n} H_{mn}(\Psi) cos(m\theta - n\phi). \tag{5.5}$$

The Fourier components H_{mn} in Eq. 5.5 are basically depending on the toroidal component of the vector potential $\vec{A}_{RMP}$, which is connected to the RMP field via $\vec{B}_{RMP} = \nabla \times \vec{A}_{RMP}$. They can be written in an integral form and are needed to be solved numerically and. Finally, the coordinates have to be mapped back to geometrical coordinates as described in detail in Ref. [18]:

$$H_{mn}(\Psi) = \mathrm{Re}\frac{1}{(2\pi R_0)^2}\iint_0^{2\pi} R(\vec{x}(\Psi,\theta,\phi)) \cdot A_\phi(\vec{x}(\Psi,\theta,\phi)) \cdot \exp(-im\theta + in\phi)\, d\theta d\phi. \quad (5.6)$$

Eq. 5.6 describes finally the spectral composition and the radial dependence expressed by the flux coordinate Ψ of the external RMP field.

Equation 5.4 assumes that the external perturbation is small with respect to the equilibrium term. For the maximum DED field, the perturbation amplitude in terms of the radial component of the RMP field B_r is in the order of $\sum_{q=3} B_r/B_\phi = 10^{-3}$ of the toroidal magnetic field B_ϕ and, therefore, the assumption is reasonable. This approach, i.e. the linear superposition of H_0 and H_1, implies that any coupling between the terms by means of *internal plasma response* is neglected per definition. The external RMP field can induce internal currents to the plasma as conductive medium that can potentially change the equilibrium itself in terms of H_0 or the RMP field distribution in terms of H_1 in coupled way which will be discussed in more detail in section 5.5. Neglecting these additional plasma response effects like in the approach discussed above, is known as the so-called **vacuum approximation**.

The set of equations of motion in Eq. 5.3 is solved three-dimensionally by numerical integration with the help of the *GOURDON* code [52, 53] which was adapted for the geometry at TEXTOR-DED. For the integration standard methods are used as described in detail in Ref. [54], e.g. *Runge-Kutta* [55, p.710]. It is important to note that the numerical integration can cause a loss of magnetic flux as a numerical error. However, for the edge magnetic topology discussed in this thesis, this effect is negligible as field lines leave the calculated space rapidly.
The unperturbed magneto-hydrodynamic equilibrium is calculated by means of the *DIVA* code [56]. The GOURDON code superposes the external magnetic perturbation field calculated with Biot-Savart's law for the DED geometry to the equilibrium calculated with DIVA. This allows for a flexible calculation of the magnetic topology for different coil setups, i.e. DED base mode or current distributions within the DED coils. In the following, a short overview of methods for displaying the magnetic topology and a detailed analysis of the topological domains is presented in section 5.4.

5.2 Visualization Methods of the Magnetic Topology

Two methods are established to visualize the magnetic topology: the **Poincare** plot and the **Laminar** plot [18]. They will be introduced in the following by means of a

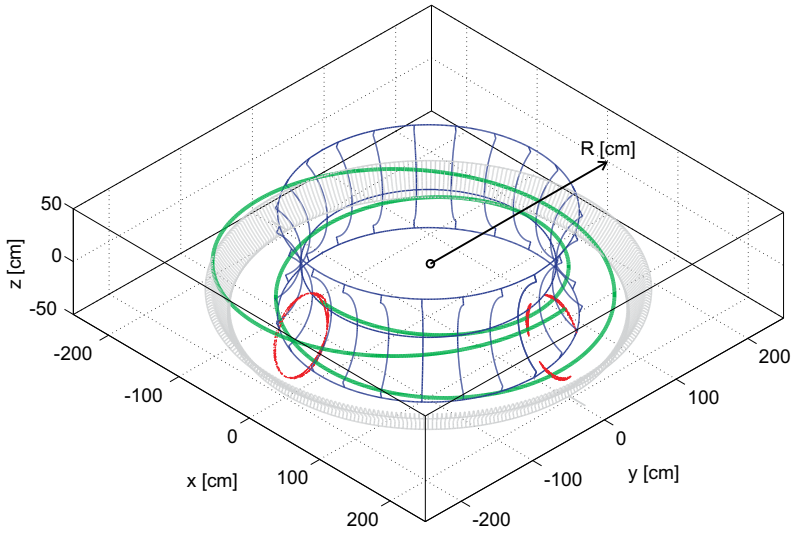

Figure 5.1: Perspective view onto the toroidal TEXTOR geometry in Cartesian coordinates with DED target at the high magnetic field side (blue) and ALT limiter at the low magnetic field side (grey). A field line (green) is traced around the torus for 2.25 toroidal turns. For the toroidal positions $\phi = 0$ ($\rightarrow y = 0$) and $\phi = 270°$ ($\rightarrow x = 0$), Poincare plots (red) are overlayed.

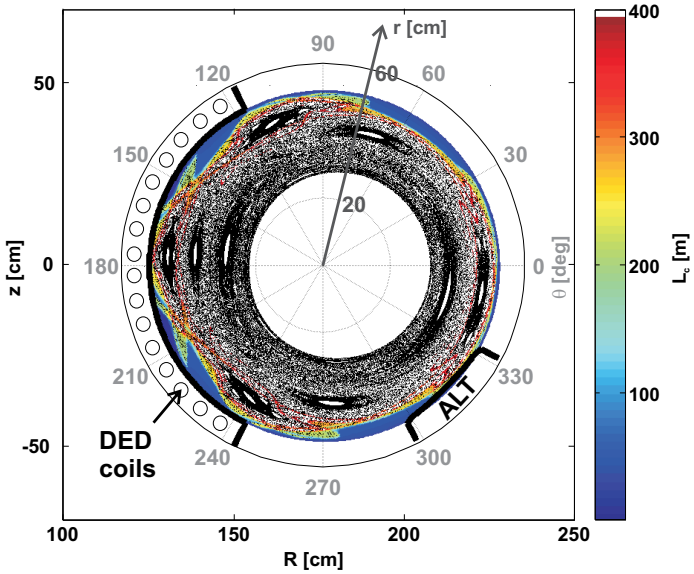

Figure 5.2: Poincare and laminar plot for a poloidal cross-section at $\phi = 0$ in $R - z$-coordinates. Polar coordinates are overlayed in grey.

TEXTOR plasma equilibrium with typical parameters: plasma current $I_P = 320\,\mathrm{kA}$, toroidal magnetic field $B_t = 2.28\,\mathrm{T}$, poloidal plasma beta $\beta_{pol} = 0.45$ and a safety factor at the LCFS of $q_a = 5.2$. A static DED field in $m/n = 3/1$ base mode configuration is applied with a current in the DED coils of $I_{DED} = 2.0\,\mathrm{kA}$. The GOURDON code is used for tracing the field lines three-dimensionally.
Figure 5.1 shows a perspective view on the TEXTOR geometry in Cartesian coordinates. The main plasma limiting surfaces, the DED target and the ALT, are indicated in blue and grey. A field line (green) is started at the position of the $q = 3$ surface and traced around the torus for 2.25 toroidal turns. The field line describes a helical path through the chamber with a third poloidal turn per one full toroidal turn due to given helicity given by the safety factor of $q = 3$.

The Poincare Plot is a puncture plot of field lines intersecting a poloidal cross-section at a fixed toroidal position. It can be calculated by means of field line tracing, e.g. with the GOURDON code. An example is shown in figure 5.1 for field lines around the $q = 3$ surface at two toroidal position $(x, 0, z)$ and $(0, y, z)$ corresponding to toroidal angles $\phi = 0$, $\phi = 270°$, respectively. In figure 5.2, a Poincare plot is shown with high resolution for the toroidal position $\phi = 0$ as a function of the vertical axis z and the radial axis R. Note also the major radius R in figure 5.1. In this display, the structure of the magnetic topology gets is visualized. The center of the magnetic topology is found to be shifted in the direction of the minor radius toward the low magnetic field side due to the Shafranov shift (compare section 2.1). However, at the far plasma edge, where field lines can connect to the wall components on short distances, the distribution of field lines gets thinner. Especially at this radial range another display of the magnetic topology is beneficial, the Laminar plot.

The Laminar Plot is produced by calculating the distance of a field line from the starting point until it hits the wall. This distance - the so-called connection length L_c - can be calculated, e.g. from the position of a specific diagnostic, in both directions. In terms of a general consideration of the magnetic topology, the sum, i.e., the total connection length is often used as a quantity to distinguish different domains. For interpretation of a local topological domain with respect to transport related properties the shortest connection length of field lines to the wall can be used as e.g. particles are supposed to follow the field lines with shortest connection length to the wall. As an example, figure 5.2 shows the total connection length in color scale with the Poincare plot as an overlay. In general, field lines with short connection to the wall are found to be present in the plasma edge. Toward the plasma core, the connection length exceeds the cut-off length of the calculation, here $L_c^{max} = 400\,\mathrm{m}$. Hence, the laminar plot can be used as a tool to quantify the plasma edge magnetic topology in detail.
It is convenient to display the magnetic topology as both Poincare and laminar plot transformed to polar coordinates. In figure 5.2 a polar coordinate system is plotted as an overlay. The enfolded presentation of the same laminar and Poincare plot is shown in figure 5.4 and will be used in section 5.4 to introduce the topological domain and to summarize experimental findings with constant DED field in support of them.

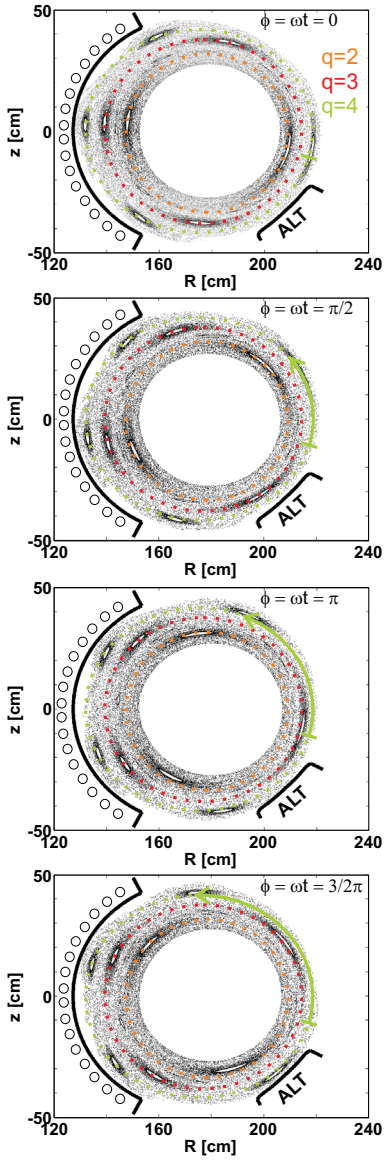

Figure 5.3: Poincare plots for different toroidal positions ϕ respectively a rotating DED field in electron diamagnetic drift direction. The position of the rational flux surfaces are marked (dotted colored lines).

Rotating DED Field in Quasi-Static Approach The rotation of the external RMP field is realized at TEXTOR by applying currents to the DED coils with sinusoidal waveforms. A stepwise application of this same sinusoidal current distribution in the DED coils to the modeling code as in the experiment enables for calculating time dependent rotation of the external DED field. This concept is used in the frame of this work as a quasi-static approach to compare the measured plasma structure with the rotating magnetic topology in vacuum approximation. Figure 5.3 shows Poincare plots of a rotating resonant DED field for a stepwise applied sinusoidal current distribution for different phases of one rotation period. The magnetic topology is shown to rotate in electron diamagnetic drift direction. It is important to note that due to the symmetrical properties of the DED one rotation period in time corresponds to one toroidal turn around the torus respectively $\Delta\Theta \approx \Delta\phi/q$ turn in poloidal direction. Hence, measuring at a fixed position a quantity – related to the magnetic topology as a function of time during application of a rotating DED field – corresponds to scanning the actual magnetic topology in the helical or both poloidal and toroidal direction. This approach is convenient as it isolates the 3D effects due to the RMP field and neglects additional effects, e.g. intrinsic error fields due to misalignments or the Shafranov shift, which lead to an additional 3D inhomogeneity of the magnetic topology. In particular, the connection length of field lines from the fixed measurement position to the wall will be calculated for a rotation period and, therefore, as a function of time in order to compare it to the measured quantities in chapter 6.

5.3 Modeling of the Plasma Parameters in a Perturbed Magnetic Topology in Vacuum Approximation

The experimental results presented in chapter 6 are compared to results from simulations with the code package EMC3-EIRENE. This code package accounts for 3D edge plasma and neutral gas transport within a static magnetic topology in vacuum approximation. Therefore, two 3D codes are coupled: The fluid edge plasma code **EMC3** [57] and the kinetic transport code **EIRENE** [58] for neutral particles. An iterative procedure is applied to obtain a self-consistent solution for all plasma (main/hydrogen component + trace impurities) and neutral particle parameters. Hence, it represents a powerful tool to study 3D effects on edge transport, not only in stellarators (W7-AS, W7-X, LHD) [59] but also in the tokamak TEXTOR [60] and in the poloidal divertor tokamak DIII-D [61] in the presence of external RMP fields.

The EMC3 code solves a set of steady-state transport equations for particle, momentum and energy for the edge plasma in the presence of interactions with neutral particles. While transport along magnetic field lines is considered within the so-called classical transport theory by Braginski [62], no concluding model for cross-field transport is known so far. Hence, the so-called "anomalous transport" is accounted for by the free parameters of the model $D_\perp$, $\chi_\perp$ for cross-field particle and energy transport, respec-

tively, [54] which are experimentally found to be in the range of $D_\perp = 0.5 - 1.5\,\mathrm{m}^2/\mathrm{s}$, $\chi_\perp = 3 \cdot D_\perp$ [63], which is one order of magnitude larger than what models including classical and neoclassical transport predict. In particular electrostatic and magnetic turbulence is supposed to be an additional mechanism, which may increase the transport coefficients in modeling [64] and might result in the values considered above.

Production and transport of neutral particles as well as their interactions with plasma ions and electrons is calculated by the EIRENE code. This interactions are given to the EMC3 code in the form of source terms in the balance equation for plasma transport.

In the following (section 5.4), an exemplary modeling result of the EMC3-EIRENE code is utilized to describe basic experimental findings in support of the vacuum approximation.

5.4 Experimental Findings with static RMP fields in High and Low Resistivity Plasmas

The results presented in chapter 6 are based on experiments with static RMP fields in highly resistive edge plasmas. In summary of Refs. [63, 65, 51, 66, 67] a fair agreement between experimental signatures and expectations based on modeling in vacuum approximation was found. It was shown that a new three-dimensional (3D) magnetic topology is formed. Therefore, radial electron density and temperature profiles were compared to modeling results from the fluid plasma and kinetic neutral transport code package EMC3-EIRENE (section 5.3).

In the following we will summarize the basic experimental findings in comparison with results from the EMC3-EIRENE code for static RMP fields at TEXTOR with the help of figure 5.4 and figure 5.5a. Both show an enfolded presentation of a laminar plot and a Poincare plot as an overlay in polar coordinates for an representative equilibrium with parameters as described in section 5.2 and a DED field in $m/n = 3/1$ base mode with $I_{DED} = 2.0\,\mathrm{kA}$ coil current. Figure 5.5b,c show additionally the plasma structure in terms of $n_e(\Theta, r)$ and $T_e(\Theta, r)$ modeled with the EMC3-EIRENE code.

In summary, the magnetic topology in a highly resistive edge plasma can be subdivided into three topological domains with specific transport properties:

1. At the radially innermost rational flux surface, which is perturbed by the respective resonant spectral component of the perturbation field, magnetic islands are formed.

2. Further out, these islands can overlap and form a region filled with stochastically distributed, ergodic field lines leading potentially to an effectively increased radial transport. This case is shown in figure 5.4 for an $m = 4$ magnetic island with intact O-point (OP) of the island with closed flux surfaces, but a strongly ergodized X-point (XP) with stochastically distributed field lines. The laminar plot indicates that field lines at the XP connect to the DED target with $L_c \approx 300\,\mathrm{m}$.

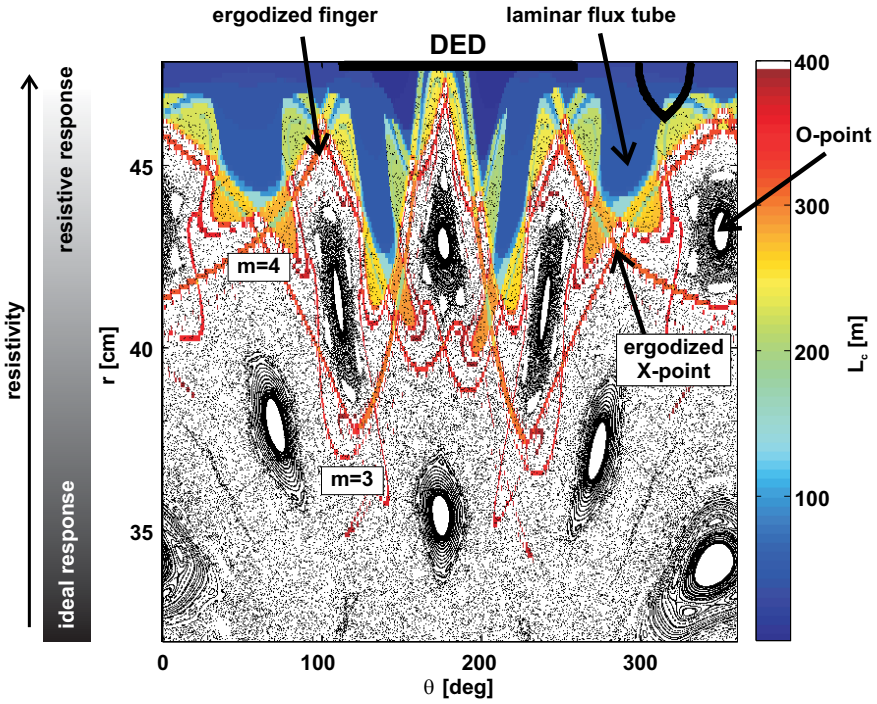

Figure 5.4: Poincare (black) and laminar plot (color) for a poloidal cross-section at $\phi = 0$ in polar coordinates.

3. The radially outermost region ($r > 44\,\mathrm{cm}$) is determined by coherent magnetic field lines with short connection length L_c to the wall. They are bundled to laminar flux tubes and are embedded into a sea of stochastically distributed field lines, which are formed as so-called ergodic fingers. This region is termed Laminar Zone of the stochastic boundary and acts like a new three-dimensional scrape-off layer (SOL) which leads to a corresponding footprint pattern on the DED target plates. It was shown (compare figure 5.5) that the Laminar zone is characterized by a fast parallel transport of both energy and particles in the laminar flux tubes which leads to a correlated drop of both n_e and T_e with respect to the surrounding ergodic fingers.

Toward the plasma core, resistivity decreases and plasma response is potentially needed to be taken into account. In particular, the magnetic topology can be dominated by instabilities driven by the current gradient and therefore deviate from the magnetic topology modeled in vacuum approximation. Experimentally, magnetic islands are detected at TEXTOR as a result of tearing instabilities, i.e. tearing modes [68, 20], which depend on the local gradient of the radial plasma current profile. They appear non-linearly and are triggered internally or due to external magnetic perturbations. This onset behavior of the tearing mode can be described by a linearized ansatz of the MHD equations as shown in detail in Refs. [69, 70]. In the zero resistivity limit, it results in an ideal plasma response, where an external magnetic perturbation leads to the formation of an internal

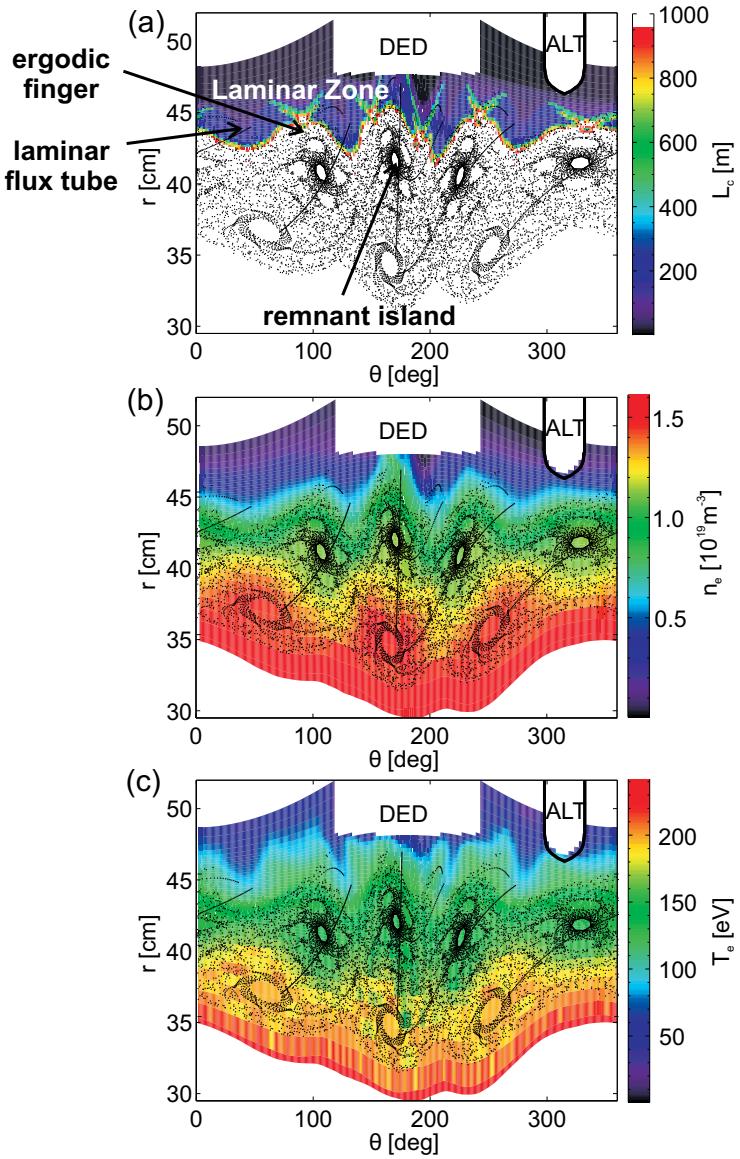

Figure 5.5: Poincare and Laminar plot (a), electron density (b) and electron temperature (c) modeled with the EMC3-EIRENE code as a function of the minor radius and poloidal angle ($D_\perp = 1\,\mathrm{m}^2/\mathrm{s}$, $\chi_\perp = 3\,\mathrm{m}^2/\mathrm{s}$).

current, which creates an counter-acting magnetic field: The external magnetic perturbation is shielded. With additional resistivity the ansatz allows to reproduce onset of the tearing instability by analyzing a critical stability parameter, which balances the gradient of the plasma current profile versus the local perturbation. With increasing perturbation, a bifurcation process in this model leads to the onset of a tearing mode. As the current decreases toward the edge due to an increasing resistivity, critical gradients of the plasma current are difficult to achieve here. Experimentally tearing modes were only detected in the core plasma at TEXTOR [68, 20].
It is reasonable that an intermediate layer must exist, where both the vacuum approximation for high resistivity and the MHD ansatz for low resistivity are not valid. A self-consistent model is needed, which contains internal plasma response currents depending on the local resistivity and in order to quantify the actual plasma response, the impact on the local plasma parameters and the resulting magnetic topology.

5.5 Plasma Response in Resistive Plasmas

Internal plasmas response currents due to an externally applied RMP field cause potentially two coupled effects: (1) The internal plasma currents can modify the plasma current profile $I_P(r)$ and therefore the equilibrium in terms of the safety factor $q(I_P)$ (axisymmetric part of current profile). Modeling focussing on this particular effect showed a minor impact on the resulting magnetic topology in comparison with the one in vacuum approximation for TEXTOR-DED equilibria [71]. (2) Due to Ampère's law the plasma response currents results in an additional magnetic field with non-axisymmetric components $m, n \neq 0$, which superposes to the vacuum magnetic field and change the resulting net local RMP field. The latter **plasma response effect** is discussed in the following and the impact on the actual magnetic topology.

The penetration process of externally applied RMP fields into a conductive plasma as depends on the local plasma parameters like e.g. resistivity, pressure gradient or plasma rotation, the basic equilibrium and therefore the geometry and the RMP field configuration and strength. This variety of variables motivates approximations often made: Approaches including plasma response often employ a constant electric field, and hence no coupling between the electric field and pressure driven forces, the so-called MHD approximation [72, 73]. Other models consider cylindrical geometry and only single basic resonant modes and assume therefore no coupling between different resonant modes [74, 75]. More complete are analyzed in Refs. [76, 77, 78] but are also restricted to cylindrical or slab geometry. In the frame of this work experimental results are compared to modeling results from a four-field drift-fluid model, the ATTEMPT code described in Ref. [79]. Four scalar fields, i.e. density n, ion flow $v_\parallel$ parallel to the magnetic field, electric potential Φ and parallel magnetic potential $A_\parallel$ are used to describe the plasma dynamics for constant electron temperature T_e and cold ions $T_i \ll T_e$. In addition the model accounts for geometrical three-dimensional curvature effects due to the toroidicity of the equilibrium of the tokamak and a self-consistent formation of internal currents

in time. It accounts for electromagnetic plasma dynamics and hence avoids the MHD approximation. The model assumes no initial relative rotation between RMP field and plasma fluid ($f_{rel} = 0$). The electrodynamic fluid interaction is basically described by Ohm's law, the parallel ion momentum balance, the quasi-neutrality condition and a particle balance as discussed in detail in Ref. [79]. The basic mechanisms of RMP field screening resulting from this model were reproduced by a simplified model proposed in Ref. [80] and will be illustrated in the following.

We consider Ohm's law with the internal current density $J_\parallel$, the classical resistivity $\eta_\parallel$, both parallel to the total magnetic field:

$$\eta_\parallel J_\parallel = \frac{\nabla_\parallel p_e}{en} - \nabla_\parallel \Phi \tag{5.7}$$

The righthand side of Eq. 5.7 describes the parallel forces on the electrons consisting of two terms: One is given by the electric potential Φ and one by the parallel electron pressure gradient ($\nabla_\parallel p_e$) with the elementary charge e and the electron density n. Equation 5.7 represents a force balance. The terms are balanced according to the local plasma parameters in way that the plasma free energy is minimized [80].
An RMP field can be introduced by considering Ohm's law (Eq. 5.7) in periodic slab geometry with z in the direction parallel to a field line of an unperturbed equilibrium, x in the direction normal to the flux surface and y bi-normal and hence perpendicular to a field line and in the plane of a flux surface. The magnetic field can be expressed as

$$\vec{B} = B_0\vec{e}_z + B_x\vec{e}_x + B_y\vec{e}_y \tag{5.8}$$

with the total radial and poloidal magnetic field smaller than the toroidal magnetic field $B_0 \gg B_x, B_y$, i.e. the deviations of the RMP field from the equilibrium field are small. Here, the components $B_x = \tilde{B}_x + R_x$ and $B_y = \tilde{B}_y + R_y$ include both the internal plasma response field $\vec{\tilde{B}}$ and the externally applied RMP field $\vec{R}$. Hence, the parallel current density in the direction of the magnetic field can be expressed as

$$J_\parallel = \frac{\vec{B}}{|\vec{B}|} \cdot \vec{J} \approx J_z + \frac{B_x}{B_0}J_x + \frac{B_y}{B_0}J_y \approx J_z. \tag{5.9}$$

Comparing Eq. 5.9 to Eq. 5.7, the radial component of the righthand side of Eq. 5.7 is found to be the radial component of the current density: $\eta_\parallel J_x = \frac{1}{en}\frac{\partial p_e}{\partial x} - \frac{\partial \Phi}{\partial x}$. With the radial component of the electric field $E_x = -\frac{\partial \Phi}{\partial x}$, Ohm's law can be rewritten to:

$$\eta_\parallel J_z \approx \frac{B_x}{B_0} \cdot \frac{1}{en}\frac{\partial p_e}{\partial x} + \frac{B_x}{B_0}E_x + \frac{B_y}{B_0}E_y. \tag{5.10}$$

In equation 5.10 the electric field component E_z has been neglected. Note that E_x describes the deviation of the radial electric field from the value without RMP, i.e. $E_x = 0$ for $R_x = 0$.

Eq. 5.10 describes the electrodynamic interplay between the pressure driven diamagnetic force, the electric field and the current density. The actual value of each term can identified

using a free energy minimization approach. According to Ref. [81] the local density of the plasma free energy $\mathcal{F}$ can be written as:

$$\mathcal{F} = \underbrace{\frac{m_i n}{2} v_E^2}_{\text{ion kinetic energy density}} + \underbrace{\frac{m_e n}{2}\left(\frac{J_\parallel}{en}\right)^2}_{\text{electron kinetic energy density}} + \underbrace{\frac{\tilde{B}^2}{2\mu_0}}_{\text{magnetic energy density}} \tag{5.11}$$

with $\vec{v}_E$ being the $\vec{E} \times \vec{B}$ velocity. It can be assumed that the plasma tries to get into a state where the plasma free energy is minimal. However, Eq. 5.10 acts as an constraint for the minimization problem, which implies that the distribution of the free energy depends on the local plasma parameters, i.e. plasma pressure gradient and resistivity.
Depending on the local plasma parameters, it can be energetically beneficial to create internal plasma response currents and hence magnetic fields $\tilde{B}_x$ and $\tilde{B}_y$. Eq. 5.10 has the following qualitative implications for the local coupling of an externally applied RMP field R_x:

- For **high resistivity**, only a small current density J_z is needed in order to compensate the righthand side of Eq. 5.10, i.e. the radial magnetic field $B_x = \tilde{B}_x + R_x$ scales with pressure gradient and the electric field. As in this case J_z is small, no internal magnetic field $\tilde{B}_x$ is generated, hence $B_x \approx R_x$. The ratio $\gamma = -\tilde{B}_x/R_x$ can defined as a screening factor, which gets $\gamma = 0$, if the total radial magnetic field corresponds to the externally applied radial magnetic field R_x. The external RMP fields penetrates completely and the vacuum approximation becomes valid.

- In the limit of **zero resistivity**, a large current density J_z is needed to balance the total magnetic and electric field. Large numbers of J_z in turn lead to an negative internal radial magnetic field $\tilde{B}_x$ and hence a reduction of $B_x = \tilde{B}_x + R_x$. Ideally, the total radial magnetic field can be totally compensated to zero for $\tilde{B}_x = -R_x$. In this case the externally applied radial magnetic field is screened by an internal radial magnetic field as a consequence of an internal current density. The screening factor becomes $\gamma = 1$ for a complete compensation in this ideal plasma response limit.

- In between these extremes of ideal plasma response and full field penetration, the current density is limited by an **intermediate resistivity**. As a consequence a stable equilibrium state is reached, as soon as Eq. 5.10 is balanced and the plasma free energy is minimal.

For tokamak plasmas with a resistivity depending on the electron temperature T_e as $\eta \propto T_e^{-3/2}$, the discussion above implies that in the plasma core with high values of T_e an ideal plasma response can be expected while towards the plasma edge (T_e small) a resistive response close to the vacuum approximation is expected.
In the following, a fixed "intermediate" resistivity at a certain rational flux surface is considered in order to understand the penetration process as a function of the external RMP field strength R_x. Figure 5.6 shows qualitatively results from the complete four-field drift fluid modeling taken from [80]. For **low external radial magnetic field strength** R_x, the external RMP field is screened ($\gamma = 1$) and the radial electric field $E_x = 0$.

With **increasing RMP amplitude**, the current density J_z is limited by the resistivity. As a consequence, a radial electric field E_x evolves and the screening factor γ decreases. This transition from screening to penetration of the RMP field gets plausible looking at Eq. 5.7. It is obvious that the current density diminishes as soon as $\vec{E} = -\nabla_\parallel \Phi \rightarrow \nabla_\parallel p_e/en$. Hence, the penetration transition is characterized by a compensation of the pressure gradient by an electric field. This consideration underlines that the screening threshold is shifted toward higher RMP amplitudes for higher pressure gradients as they appear typically in the plasma edge. This qualitative reflection shows the counter-dependencies of the screening effect on the plasma parameters, i.e. resistivity and pressure gradient. It points out the importance of measurements of in particular electron density, temperature and pressure profiles as important ingredients of plasma response.

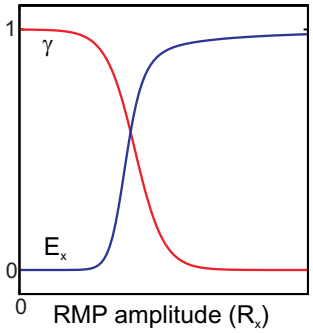

Figure 5.6: Qualitative dependence of f and E_x on the RMP amplitude. (taken from [80])

In order to quantify the internal current distribution, we focus on Eq. 5.10. It was described in section 5.1 that the external helical RMP field can be expressed by $\vec{B}/|\vec{B}| \propto cos(m\theta - n\phi)$ with m, n being the poloidal and toroidal mode number, respectively. As a consequence, also $J_\parallel$ is needed to be of the same mode composition. In the following numerical results of the more complete ATTEMPT code [79] will be discussed. Figure 5.7 shows the current density $J_\parallel(q, \Theta)$ color-coded as a function of the radial coordinate in terms of the safety factor q and the poloidal angle for a $m/n = 3/1$ DED field and and a screening factor of $\gamma_{m=4} = 0.9$ and $\gamma_{m=3} = 0.3$ for $m/n = 3/1, 4/1$ resonant components, respectively. A Poincare plot calculated in vacuum approximation is overlayed. The extrema of $J_\parallel$ are found to fit to the O-point and X-point position of a vacuum magnetic island and hence to the resonant composition of the external RMP field as motivated by means of Eq. 5.10. According to Ampère's law, $J_\parallel$ generates an RMP field on its own, which superposes with the external vacuum magnetic field and hence leads to a new magnetic topology. Figure 5.8 shows a comparison of the new "screened" magnetic topology (red) and the magnetic topology in vacuum approximation (black) with $\tilde{B}_x = 0$ and therefore $\gamma = -\tilde{B}_x/R_x = 0$ per definition. The magnetic island appears to be shifted helically by $\Delta\phi = \Delta\Theta/q \rightarrow \pi/2$ for $\gamma \rightarrow 1$ in co-B_t direction. This important finding can be used for comparison to experimental measurements as discussed in section 6.3.2.

It is important to note that the screening effect observed locally at a certain flux surface does not only depend on the pressure gradient, the resistivity and external RMP field spectrum and strength. It was shown the model described in Ref. [77] that the penetration of external RMP fields depends also on the relative rotation frequency

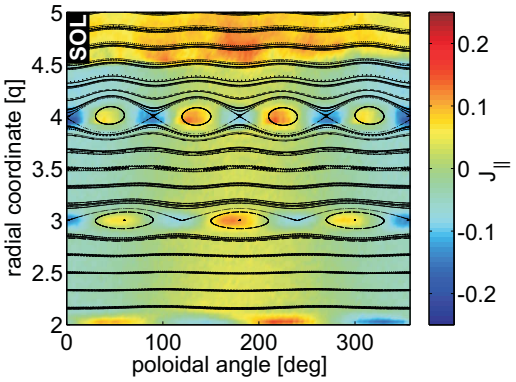

Figure 5.7: Display of the parallel current density $J_{\parallel}$ for $\gamma_{m=4} = 0.9$ as a function of the radial coordinate in terms of the safety factor q and the poloidal angle with a Poincare plot modeled in vacuum approximation as an overlay.

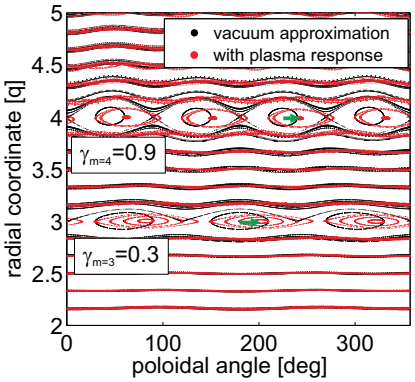

Figure 5.8: Poincare plots of the magnetic topology in vacuum approximation ($\gamma = 0$, black) and with plasma response included (red).

$f_{rel} =$ $_{tor}/2\pi -$ $_{RMP}$ between toroidal plasma fluid angular rotation frequency $_{tor}$ and external RMP field rotation frequency $_{RMP}$. For constant RMP fields the relative rotation reduces to $f_{rel} =$ $_{tor}$. The plasma rotation itself leads to an additional term $_{\parallel}J_z$ $v_y B_x/B_0$ due to Lorentz force and emphasizes a rotation dependence of the internal screening currents. In tokamaks the plasma fluid rotation is normally non-zero and for TEXTOR discharges typically in the order of $_{tor} = \pm 50\,kHz$ and $_{pol} = \pm 5\,kHz$ in the toroidal and poloidal direction, respectively [82] and therefore not negligible in general. However, the model discussed here [80] includes the relative rotation but does not account for an initial relative rotation without RMP field, i.e. $f_{rel} = 0$.

In conclusion, two important ingredients for plasma response can be utilized for experimental measurements: the electric field and the electron pressure profile, i.e. more specific the electron density and temperature. The latter can be used to detect a potential shift of the local magnetic topology.
In tokamak plasmas, the dependencies of resistivity, pressure and pressure gradient are strongly coupled and therefore impossible to be separated. The possible rotation dependence, is experimentally di cult to be controlled as changing the plasma rotation by controlling the torque input of neutral beam injection comes along with a change in particle input and hence typically in pressure and pressure gradient. An elegant way to change the relative rotation is therefore to keep the initial plasma rotation unchanged and rotate the external RMP field in different rotation directions and with different frequencies. This approach is used in the frame of this work by means of the Dynamic Ergodic Divertor at TEXTOR.

Chapter 6

Results

The plasma edge structure with fast rotating Resonant Magnetic Perturbation (RMP) fields is studied by applying the gas-puff imaging technique in a first step (section 6.1). In section 6.2, it is shown following Ref. [83] that the outermost radial region ($r/a > 0.98$) is determined by a three-dimensional Scrape-off layer (3D SOL) induced by the fast rotating RMP fields. The dependence of the plasma edge structure on both, rotation and perturbation amplitude in a radial region of $r/a > 0.9$ including the outermost rational flux surface is investigated in section 6.3. According to Refs. [84, 85], we study the extension of the 3D SOL and the impact of the plasma response on this 3D plasma structure. A comparison of the measured plasma structure with modeling results of transport in a 3D perturbed edge layer will provide evidence on the underlying magnetic topology. It is shown that the 3D SOL is terminated at the next inward rational flux surface. Here, the formation of the local plasma structures is limited by a rotation dependent plasma response. On the basis of these findings, dedicated measurements of the plasma structure directly in front of the RMP coils are presented and related to the underlying magnetic topology in section 6.4.

6.1 Three-dimensional Imaging of a Rotating Edge Plasma Structure

Electron density variations in the plasma edge are studied during application of a fast rotating Resonant Magnetic Perturbation (RMP) field. For static RMP fields applied the electron density is known to vary significantly due to a new inhomogeneous three-dimensional magnetic topology, and due to the transport properties deviating from those of the plasma in the unperturbed equilibrium state [51, 67, 65]. The gas-puff imaging technique on thermal hydrogen is utilized as a first step approach to investigate experimentally if a non-axisymmetric plasma structure exists with fast rotating RMP fields. In this effort, we present new three-dimensional measurements of the electron density variations, i.e. in the poloidal and radial directions and time dependent. In particular,

temporally resolved measurement will provide direct information of a 3D plasma structure in the rotation direction of the RMP field by confirming a correlation between a poloidal modulation of the electron density with a modulation in time at a fixed poloidal position. The findings described are based on experiments with static RMP fields as discussed in section 5.4. In these studies, electron density n_e and temperature T_e profile reactions [51, 67, 65] were compared to the magnetic topology in vacuum approximation, i.e. superposition of the magnetic perturbation amplitude onto a stationary axisymmetric equilibrium without plasma response. It was shown that a new three-dimensional (3D) plasma boundary structure is formed which could be understood by the vacuum based magnetic topology. The radially outermost topological domains is of particular interest here (compare section 5.4): The latter region is determined by coherent magnetic field lines with short connection length L_c to the wall. They are bundled to laminar flux tubes and are embedded into a sea of long stochastically distributed field lines, which propagate radial outward as so-called ergodic fingers. This region is termed Laminar Zone of the stochastic boundary and acts like a new three-dimensional scrape-off layer (SOL). It was demonstrated that the static 3D SOL imposes a poloidal modulation to the electron density and temperature fields [67, 65].
Here, we focus on measurements of the electron density fluctuation $\tilde{n}_e(\Theta, r, t)$ during application of a fast rotating RMP field in order to show for high RMP rotation that a 3D rotating plasma structure compatible with a fast rotating 3D SOL exists.

6.1.1 Experimental Scenario

The experiments were performed at TEXTOR-DED in $m/n = 3/1$ base mode configuration, a low order electro magnetic multi-pole with therefore high RMP amplitudes in the edge layer. A NBI heated plasma (heating power $P_H = 1\,\mathrm{MW}$, L-mode) is analyzed with circular shape and limited at the DED target with a plasma radius $a = 46.2\,\mathrm{cm}$. The global parameters are: line-averaged electron density in the core $\bar{n}_e(R = R_0) = 2.0 \cdot 10^{19}\,\mathrm{m}^{-3}$, electron temperature in the core $T_e(R = R_0) = 1.7\,\mathrm{keV}$,

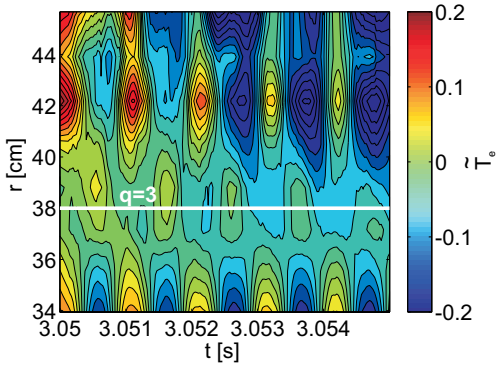

Figure 6.1: Normalized electron temperature $\tilde{T}_e$ measured with ECE-I as a function of minor radius r and time (#108000)

edge electron density at the position of the last closed flux surface of the unperturbed case $n_e(r/a = 1) = 2.0 \cdot 10^{18}\,\mathrm{m}^{-3}$, edge electron temperature $T_e(r/a = 1) = 57\,\mathrm{eV}$ and toroidal plasma rotation $\Omega_{tor} = +6\,\mathrm{kHz}$ at $r/a = 0.6$ measured by Charge Exchange Recombination Spectroscopy (CXRS) [86]. A DED field with a rotation frequency of $\nu_{DED} = +974\,\mathrm{Hz}$ (DED period $\tau_{DED} = 1/\nu_{DED} = 1.027\,\mathrm{ms}$) in electron diamagnetic drift direction is applied. Indications for an locked $m/n = 3/1$ magnetic island due to a tearing instability [20] were found in electron temperature measurements shown in figure 6.1. The electron temperature T_e measured by electron cyclotron emission (ECE) [87] is displayed normalized to its mean value $\bar{T}_e$: $(T_e - \bar{T}_e)/\bar{T}_e$. A counter-modulation appears at the rational flux surface $q = 3$ as an reliable indicator for an $m/n = 3/1$ magnetic island due to a tearing mode [88]. The counter-modulation in T_e can be explained considering the heat transport of a shifted magnetic island structure caused by the tearing mode as sketched in figure 6.2. The magnetic island changes the unperturbed equilibrium locally and lead to sub-volumes with closed flux surfaces at the so-called O-point (OP). Both heat and particles are transferred from the core by cross-field transport $q_\perp$, $\Gamma_\perp$, respectively, via potentially deformed closed flux surfaces and reach the island. The deformation of the flux surfaces nearby the island forces a modulation in T_e. However, at the position of the O-point (OP) the flux surfaces are short-cut over a radial extension defined by the island's width which lead to fast effective radial transport $q_\parallel$, $\Gamma_\parallel$ parallel along the short-cut flux surfaces around the island. In this interpretation, a periodic flattening of the $T_e(r)$ profiles at the island OP is expected which is phase-shifted poloidally. This behavior explains the counter-modulation of an rotating magnetic islands due to a tearing mode as measured in terms of T_e in figure 6.1. The detailed transport properties of a magnetic island are not yet fully understood and matter of actual research [88, 89, 90]. This scenario represents an ideal test case for the GPI diagnostic as a well diagnosed structure rotates at the DED rotation frequency and should cause electron density variations due to the magnetic island evidently present.

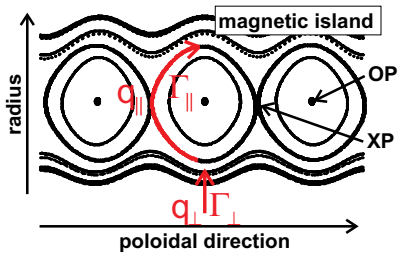

Figure 6.2: Simplified sketch of a magnetic island in the poloidal plane. O-point (OP) and X-point (XP) are labeled.

In the experiments presented, the electron density variations $\tilde{n}_e(\Theta, r, t)$ are measured with the gas-puff imaging (GPI) diagnostic (section 4.1). In order to show the orientation of the active volume of the GPI diagnostic, we recall the magnetic topology for a static RMP field modeled in vacuum approximation in figure 6.3 from section 5.4. The measurement position is marked by the pink box and the rotation direction of the RMP field along the position of the rational flux surface $q = 3$ is indicated.
The measured H_α intensity variation normalized to its average value corresponds to the density fluctuation level $(I - \bar{I})/\bar{I} = (n_e - \bar{n}_e)/\bar{n}_e$ for $T_e > 40\,\mathrm{eV}$, which is the case here at $r < a$. Therefore, the measured intensity fluctuations will be referred as density fluctuations $\tilde{n}_e = (n_e - \bar{n}_e)/\bar{n}_e$ for the remainder of this chapter. The method enables for

imaging density variations $\tilde{n}_e$ with high spatial and temporal resolution of $2 \times 2\,\mathrm{mm}^2$ and $\Delta t = 20\,\mu\mathrm{s}$ in both the radial and poloidal direction.

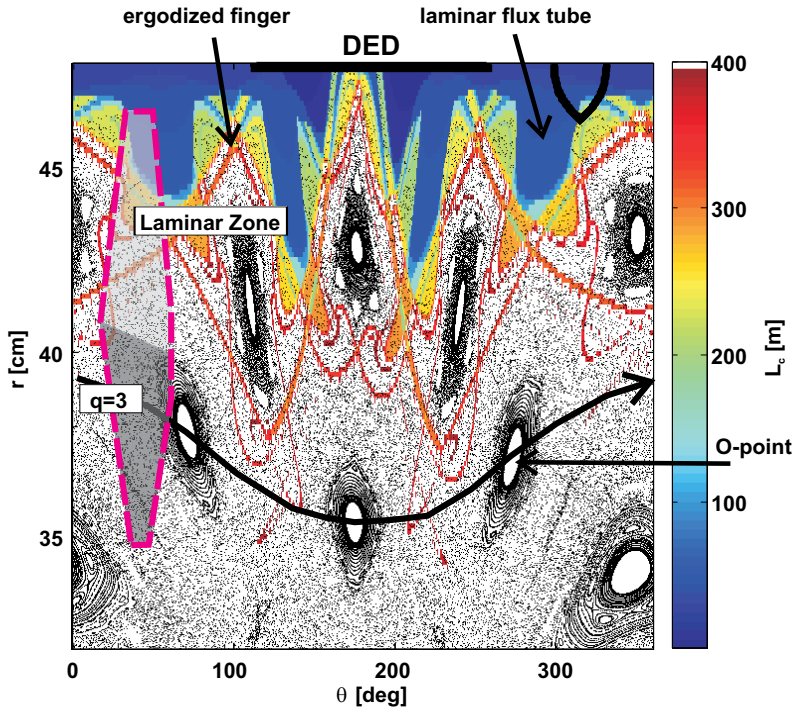

Figure 6.3: Magnetic topology modeled in vacuum approximation according to section 5.4. The measurement position of the GPI diagnostic is marked (pink/dashed box) and the rotation direction of the RMP field along the position of the rational flux surface ($q = 3$) is indicated by black arrows.

6.1.2 Visualization of a Rotating Plasma Structure

Figure 6.4 shows a sequence of frames recorded with the GPI diagnostic and transformed to $r - \Theta$ coordinates. Here, the electron density fluctuation level is displayed normalized to the average value of each pixel $\tilde{n}_e(t) = (n_e(t) - \bar{n}_e)/\bar{n}_e$. The frames are measured at times $t = t_0 + \Delta t$ with $t_0 = 3.051\,\mathrm{s}$ and we display frames within $\Delta t = [0, 0.92]\,\mathrm{ms}$ and therefore nearly one DED rotation period, i.e. $\tau_{DED} \in [0, 1]$. A modulation of $\tilde{n}_e(t)$ is measured coherent to the external RMP rotation frequency of $\nu_{DED} = +974\,\mathrm{Hz}$. This shows experimentally that a plasma structure exists, which rotates locked to the externally applied DED rotation. The density fluctuations $\tilde{n}_e$ are found to modulate by $\pm 35\%$ at maximum with the actual amplitude depending on the minor radius. The modulation depth is largest for $r > 40\,\mathrm{cm}$ and decreases toward the core plasma to $\pm 10\%$. In the poloidal direction, sub-modulations of $\tilde{n}_e(\Theta)$ are detected. This gives

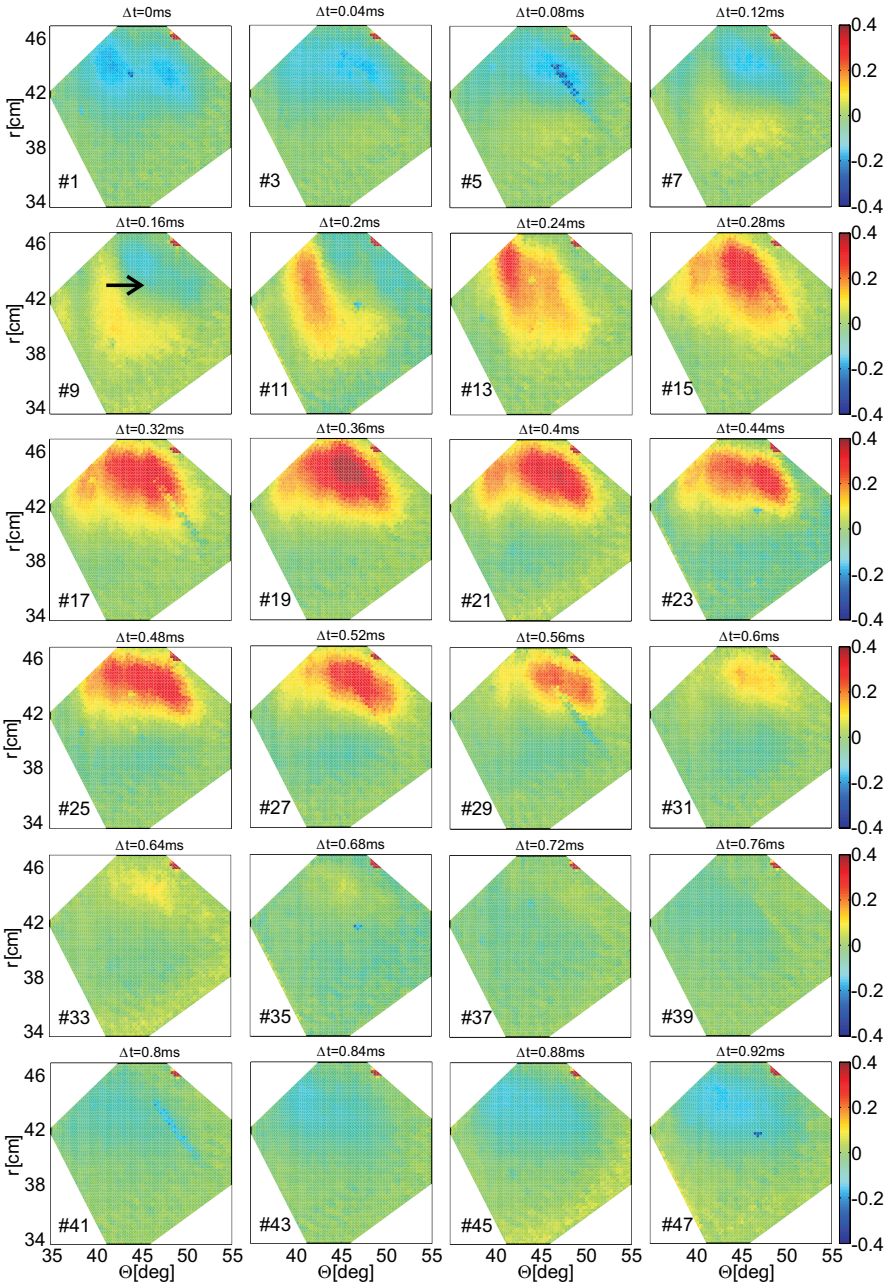

Figure 6.4: Sequence of relative density variations $\tilde{n}_e$ measured with the GPI diagnostic for #108000 as a function of the poloidal angle Θ and the minor radius r. Every second recorded frame is displayed according to the frame numbers.

first experimental evidence that a underlying rotating magnetic topology exists, which changes along the minor radius and is sub-structured in the poloidal direction. The sequence of frames indicates that the $\tilde{n}_e$ maximum moves in the poloidal direction toward larger numbers of Θ. This is consistent with the rotation direction of the DED field in electron diamagnetic drift direction.

In order to quantify the modulation properties of $\tilde{n}_e$ in detail, a radial profile $\tilde{n}_e(r)$ at a fixed poloidal position is analyzed. Figure 6.5a shows the temporal evolution of $\tilde{n}_e(r,t)$ at $\Theta = 45°$. A clear modulation is found coherent to the external DED rotation frequency and the modulation depth has a radial function with its maximum at $r > 40\,\mathrm{cm}$ consistently with the considerations in figure 6.4. As the frequency of the modulation is the DED rotation frequency, a conditional averaging method can be applied (section 4.4) as shown in figure 6.5b. This method allows to reduce statistical noise and the impact by physical effects which are not related to the RMP rotation frequency. The modulation at the rational flux surface $q = 3$ around $r = 39\,\mathrm{cm}$ is found to be delayed and therefore phase shifted with respect to the modulation at $r > 40\,\mathrm{cm}$. The consideration of both, modulation depth of $\tilde{n}_e$ and phase shift gives direct experimental evidence that the local plasma structure changes from the position of the rational flux surface $q = 3$ to $r > 40\,\mathrm{cm}$. This experimental findings are compatible with the general transport features of magnetic island due to the detected tearing mode as suggested in section 6.1.1. A dominantly parallel transport along these new flux surfaces around the O-point of the island and a displacement of the island due to the tearing mode lead to a phase-shift and flattening of the density profile. Here, this flattening results in a decreased modulation depth at $q = 3$. We show these measurements as an example for imaging a well studied plasma structure.

In order to correlate the modulation of $\tilde{n}_e$ at $r > 40\,\mathrm{cm}$ to the underlying magnetic

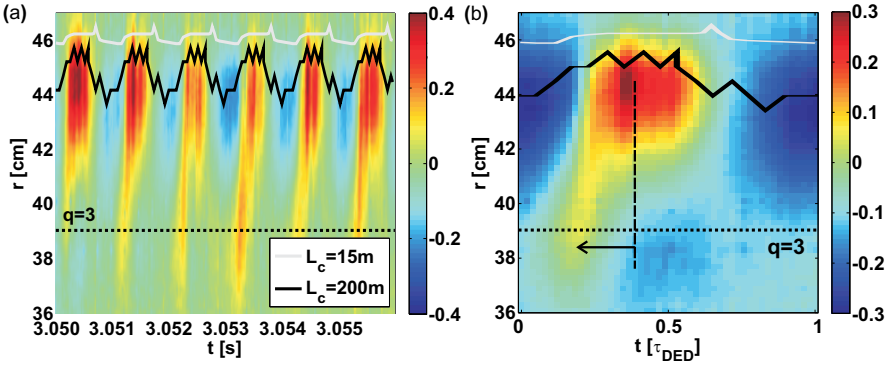

Figure 6.5: Time trace (a) of relative density variations $\tilde{n}_e/\bar{n}_e$ measured with the GPI diagnostic at $\Theta = 45°$ as a function of the minor radius r. Figure (b) shows the time trace averaged and normalized to the DED rotation period (compare section 4.4). Levels of constant connection length $L_c(t, r = \mathrm{const})$ are plotted overlayed (solid lines).

topology, the local magnetic topology is modeled in a quasi-static approach in vacuum approximation as proposed in section 5.2. The shortest connection length of field lines to the wall L_c is calculated at the position of the gas puff with an stepwise application of the sinusoidal current distribution in the DED coils. As a result, $L_c(r,t)$ modulates in t and r corresponding to an alternating layer of short connection length laminar flux tubes and long L_c ergodic fingers. Figure 6.5a shows overlayed two level of constant $L_c = \text{const}$ indicating the radial extent of the laminar flux tubes into the plasma of $\Delta r \approx 3\,\text{cm}$. The density modulation $\tilde{n}_e(t)$ at $r > 40\,\text{cm}$ is found to be in phase with the modulation of L_c with a drop in n_e correlated to a short connection length flux tube. This analysis provides first experimental evidence that the modulation measured can be correlated to the local magnetic topology modeled in vacuum approximation but that at deeper radial positions a poloidal displacement is measured as a phase between the density modulation and the applied field. The latter indicates a plasma response.

6.1.3 Summary and Conclusion

In summary, it was shown by means of the gas-puff imaging technique with high temporal and spatial resolution that rotating resonant magnetic perturbation (RMP) fields impose a plasma structure to the edge, which rotates locked to the external RMP frequency in the RMP rotation direction. The analysis shows that the rotation in the poloidal direction is correlated to a modulation in time at a fixed poloidal position. This justifies the applicability of radially and temporally resolved measurements for characterizing the rotating, RMP imposed plasma structure in two dimensions. At the rational flux surface $q = 3$, a reduced modulation depth of $\pm 10\%$ and a phase shift was found, which supports the presence of an edge magnetic island due a tearing instability detected correspondingly by ECE temperature measurements. Further out at $r > 40\,\text{cm}$, the modulation depth increases to $\pm 35\%$ and appears to be in phase with an alternating connection length layer modeled in a quasi-static approach in vacuum approximation. This indicates that a three-dimensional plasma boundary with ergodic fingers and laminar flux tubes with short connection length exists in experiments with fast rotating RMP fields. This first experimental findings will be studied based on simultaneous measurements of both electron density and temperature in section 6.2.

6.2 Formation of a Three-Dimensional Scrape-Off Layer with Fast Rotating Resonant Magnetic Perturbation Fields

Based on the initial findings of a plasma structure imposed by a fast rotating RMP field, a detailed study of the outermost edge layer is presented by means of electron density n_e and temperature T_e profiles following Ref. [83]. Both were shown to be affected during application of static Resonant Magnetic Perturbation fields due to a new three-dimensional (3D) magnetic topology [51, 67, 65].
Three-dimensional imaging of density fluctuations presented in section 6.1 gave initial experimental evidence that this 3D magnetic topology exists with fast rotating RMP fields. For two-dimensional measurements of the $n_e(r,t)$ and $T_e(r,t)$ fields, the rotation of the RMP field can be utilized as a tool to scan the plasma structure rotating through an observation volume at a fixed toroidal and poloidal position defined by the diagnostic setup.
This allows for the first time studying the geometrical properties, i.e. the geometrical extensions of the local edge plasma structure, and the plasma parameter changes under the influence of a fast rotating RMP field at TEXTOR. In combination, this will support the applicability of modeling codes for static RMP fields in vacuum approximation, i.e. without internal plasma feedback, for the far plasma edge layer ($r/a > 0.98$) in this scenario. For this, we extend the picture obtained during application of *static* RMP fields by investigating *fast rotating* RMP fields. For the static case electron density n_e and temperature T_e profile reactions were compared in Refs. [51, 67, 65] to the magnetic topology in vacuum approximation, i.e. superposition of the magnetic perturbation amplitude onto a stationary axisymmetric equilibrium without plasma response. A new three-dimensional magnetic topology is formed where the radially outermost region is defined by coherent magnetic field lines with short connection length L_c to the wall as shown schematically in figure 6.6. They are bundled to laminar flux tubes and are embedded into a sea of stochastically distributed field lines, which are formed as so-called ergodic fingers. This region is termed Laminar Zone of the stochastic boundary and acts like a new three-dimensional scrape-off layer (SOL). They are dominantly filled with a flux $\Gamma_\perp$ by radial and cross-field transport from the surrounding volume with stochastically distributed field lines, e.g. ergodic fingers. Additionally, in case of increased particle recycling, a flux $\Gamma_\parallel^{recycling}$ of ionized particles coming from the wall can contribute to the filling of the flux tube [91]. Along the flux tube, a fast parallel transport leads to flux $\Gamma_\parallel$ to the wall according to the 1D-SOL model discussed in section 2.1.2. In this interpretation, it is reasonable that the local plasma

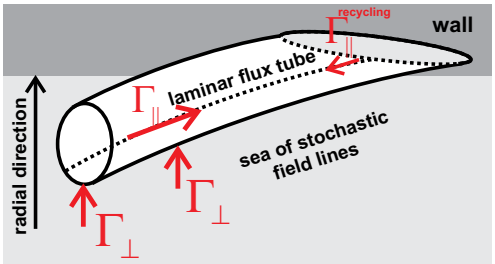

Figure 6.6: Schematic illustration of a laminar flux tube intersecting the plasma limiting wall.

parameters, e.g. electron density and temperature, depend on the interplay between parallel particle and heat transport along the flux tube and its filling by cross-field transport. It is important to note that this is a conceptual idea. Beyond this basic approach, a fast movement of electrons along the stochastic field lines will cause for instance a radial ion flux to preserve ambipolarity. This represents a particle transport as well. In the same manner, the perturbed fields will impact on trapped particles and helical effects are likely to change the particle orbits increasing particle transport. In this first attempt, such effects for correlation between the measurements and the topology not are investigated in detail. The parallel loss along field lines with a short connection to the wall is treated as dominant term determining the measured plasma structure in the very edge.
It was demonstrated in Refs. [67, 65] that the static 3D SOL exists and imposes a poloidal modulation to the electron density and temperature fields. In this section we focus on measurements of the electron density $n_e(r,t)$ and temperature $T_e(r,t)$ fields during application of a fast rotating RMP field at the radial position of the Laminar Zone. We show for high RMP rotations that the laminar flux tubes with short connection length to the wall lead to a coherent and simultaneous density and temperature drop. The full helical rotation of the external RMP field enables to determine (a) the geometrical extension of the laminar flux tubes in the radial and in the rotation direction of the rotating RMP field and (b) the plasma parameters n_e and T_e inside and at the boundary of the helical flux tube.

6.2.1 Experimental Scenario

The experiments were performed at TEXTOR with the DED field in $m/n = 3/1$ base mode configuration. An NBI heated ($P_H = 1.3\,\mathrm{MW}$) plasma with circular shape, limited at the DED target and therefore with a plasma radius $a = 46.3\,\mathrm{cm}$ is analyzed. The global parameters are adjusted to: line-averaged electron density in the core $\bar{n}_e(R = R_0) = 2.0 \cdot 10^{19}\,\mathrm{m}^{-3}$, electron temperature in the core $T_e(R = R_0) = 1.0\,\mathrm{keV}$, electron density at the position of last closed flux surface without RMP field $n_e(r/a = 1) = 5.0{\cdot}10^{18}\,\mathrm{m}^{-3}$, edge electron temperature $T_e(r/a = 1) = 80\,\mathrm{eV}$ and toroidal plasma rotation $\Omega_{tor} = +6\,\mathrm{kHz}$ at $r/a = 0.6$ measured by Charge Exchange Recombination Spectroscopy (CXRS) [86]. The DED field applied with a rotation frequency of $\nu_{DED} = +974\,\mathrm{Hz}$ (DED period $\tau_{DED} = 1/\nu_{DED} = 1.027\,\mathrm{ms}$) in electron diamagnetic drift direction results in a relative rotation between plasma fluid and rotating RMP field of $f_{rel} = +5\,\mathrm{kHz}$. The DED current is ramped up to $I_{DED} = 2.8\,\mathrm{kA}$ but is, in contrast to the plasma described in section 6.1, well below the excitation level of a tearing mode [20], i.e no indications were observed in the magnetic spectrum or in electron temperature measurements as discussed before.
The two-dimensional electron density $n_e(r,t)$ and temperature $T_e(r,t)$ fields are measured with the Supersonic Helium Beam (SHE) diagnostic based on beam emission spectroscopy on thermal helium (section 4.2). The helium beam with low divergence of $\sphericalangle \pm 1.6°$ and high neutral helium density enables for localized n_e and T_e measurements in the plasma edge ($r/a > 0.9$) with a temporal resolution of $\Delta t = 20\,\mu\mathrm{s}$ and a radial resolution of $\Delta r = 2\,\mathrm{mm}$.

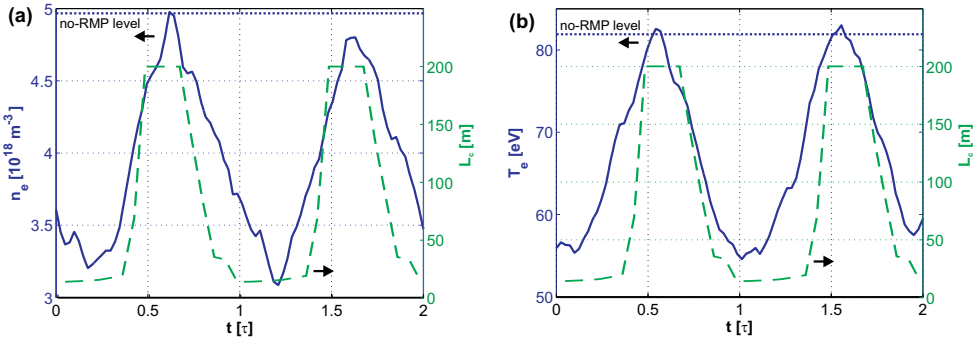

Figure 6.7: Electron density $n_e(t)$ (a) and temperature $T_e(t)$ (b) at $r = 46.6\,\mathrm{cm}$ ($r/a \approx 1$) and for a DED current of $I_{DED} = 1.5\,\mathrm{kA}$ (blue/solid, #110142). The time axis is in units of the DED period τ_{DED}. A time trace of the shortest connection length modeled quasi-statically for the rotating DED current distributions in vacuum approximation is shown overlayed (green/dashed).

6.2.2 Formation of a Rotating Three-Dimensional Scrape-Off Layer

The formation of the 3D edge layer is studied for a DED rotation of $\nu_{DED} = +974\,\mathrm{Hz}$ in electron diamagnetic drift direction. The structure of the edge plasma can be determined from the local temporal variation and the phase between n_e and T_e. Figure 6.7 shows a time trace of $n_e(t)$ and $T_e(t)$ for the radial position of the no-RMP last closed flux surface (LCFS) at $r = 46.6\,\mathrm{cm}$ ($r/a \approx 1$) and a perturbation current of $I_{DED} = 1.5\,\mathrm{kA}$. The method of conditional averaging (section 4.4) is applied and the time axis is given in units of the DED rotation period τ. A simultaneous drop of both n_e and T_e is found similar to experiments with static RMP fields [67, 65] but now followed for an entire DED rotation period. In order to compare to the magnetic topology in vacuum approximation without plasma feedback, we calculate the shortest connection length L_c from the position of the detection volume to the wall with the help of field line tracing in a quasi-static way. That means that we apply the same AC current distribution in the RMP coils to the code as being applied in the experiment during a DED rotation period. Figure 6.7 shows L_c overlayed on the n_e and T_e time traces as a function of a factitious time, which is correlated to the DED current distribution as given in the experiment. This analysis shows that the modulation in both n_e and T_e can be connected to an alternating connection length. In particular, the drop in both plasma parameters is correlated to magnetic flux tubes with short connection length being present at the measurement position, where a strong parallel transport along the field lines to the target is expected. In contrast, no drop is seen when stochastically distributed field lines with long connection length appear. This comparison shows that the 3D SOL or Laminar Zone as described by the modeling of the magnetic topology in vacuum approximation exists and rotates locked to the fast rotating external RMP field for the plasma conditions described before.

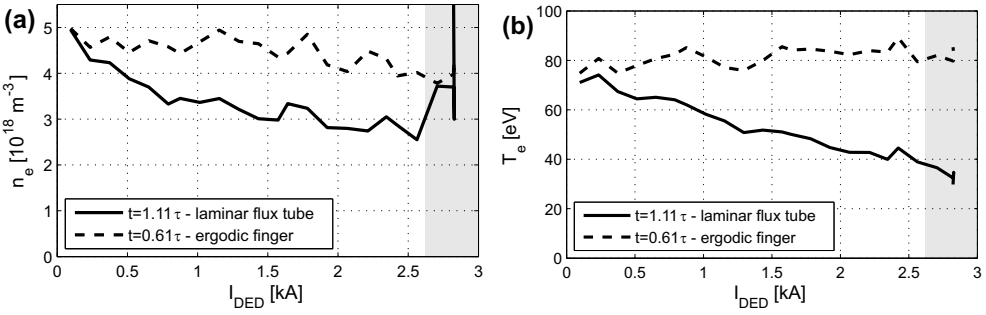

Figure 6.8: Electron density n_e (a) and temperature T_e (b) as a function of the DED current amplitude for a laminar flux tube (solid) and a long connection length field line finger (dashed) (#110141-#110146, $r = 46.6\,\mathrm{cm}$). The particle pump out phase is marked grey.

The behavior of density and temperature depends on the actual RMP current amplitude as shown in figure 6.8. The dashed lines for the plasma parameters for stochastically distributed field lines show that there is neither a drop in n_e nor in T_e independently of the RMP field amplitude. In contrast, as soon as a laminar flux tubes is present in the detection volume within a RMP rotation period, n_e drops by 35% and T_e linearly by 40% inside the laminar flux tube for a current amplitude of $I_{DED} = 1.5\,\mathrm{kA}$. For further increased perturbation strength ($I_{DED} > 2.7\,\mathrm{kA}$, highlighted grey) a transition to the so-called particle pump out effect (section 2.2) occurs where particles are transferred to the wall by enhanced transport yielding a reduction of the number of confined particle in the plasma. This results in a strong decrease of the plasma core density and an increase of the local plasma density in the edge. It is important to note that the particle pump-out described here occurs due to a strong stochastisation of edge magnetic topology as described in Ref. [92] and is not caused by a tearing mode.

The measurements of the plasma edge parameters with the fast rotating RMP field, enable to determine the geometrical dimensions and therefore the formation of the laminar flux tubes and the neighboring ergodic fingers with increasing perturbation current. Since a simultaneous drop in n_e and T_e results in a pronounced electron pressure drop as $p_e \propto n_e \cdot T_e$, this quantity will be used in the following. Figure 6.9a shows a perspective contour plot of the electron pressure $p_e(r,t)$ as a function of time and minor radius. In order to quantify the p_e modulation characteristics, a normalized helical width w_h can be introduced as the full width at half maximum (FWHM) of a modulation caused by the Laminar Zone rotating helically through the detection volume. Here, the helicity is given by the helical setup of DED coil set. The normalized helical width w_h is measured as the time delay Δt_{FT} the flux tube (FT) needs to pass through the detection volume per one DED period: $w_h = \Delta t_{FT}/\tau_{DED} = w_{FT}/(w_{FT} + w_{EF})$. Due to the symmetry of the DED field chosen with a toroidal base mode number $n = 1$, in total one flux tube and one ergodic finger (EF) rotates through the detection volume in

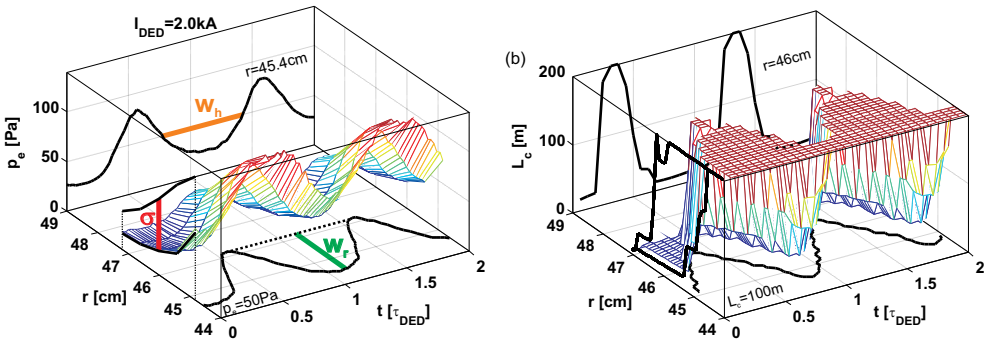

Figure 6.9: Electron pressure modulation p_e (a) and shortest connection length L_c (b) as a function of time (t) and minor radius (r) for a perturbation amplitude of $I_{DED} = 2\,\mathrm{kA}$ (#110144). Projections are extracted for a fixed radial position of $r = 45.5\,\mathrm{cm}$, a constant pressure of $p_e = 50\,\mathrm{Pa}$ and radial minimal and maximum p_e profiles (black lines).

one DED period, i.e. there is $w_{FT} + w_{EF} = \tau_{DED}$ per definition. Additionally, a radial width of a flux tube w_r can be defined as the radial extent of an isobaric modulation in $r - t$-space. It is important to note that the dimensions of the flux tube depend on the measurement position [51]. Finally, a pressure modulation depth σ can be determined in order to quantify the impact of the RMP field on the plasma transport. From figure 6.9a, it can be seen that the absolute value of $\sigma(r)$ has a radial function and decreases with increasing radius. Therefore, the drop of p_e will be quantified in the following by $\sigma(p_e)/\max(p_e)$ normalized to the local maximum of $p_e(t)$. The definitions of w_h and w_r can be also transferred to the connection length distribution $L_c(r,t)$, which is shown in a perspective view in figure 6.9b. The normalized helical width is again given by the FWHM of a connection length time trace $L_c(t)$ at a fixed radial position. The radial width w_r is determined by the modulation in $r - t$-space for a constant L_c. This allows to compare the geometrical properties of the rotating plasma structure in terms of p_e with those of the magnetic topology in terms of L_c quantitatively.

Figure 6.10 shows the geometrical quantities determined from the modulation of $p_e(r,t)$ (solid lines) and the modulation of $L_c(r,t)$ (◯) as a function of the DED current amplitude describing the formation of the Laminar Zone and the resulting plasma structure with increasing perturbation strength. Focussing first on the modulation depth giving the relative pressure drop (figure 6.10a), a clear increase is observed, which turns from a linear to a square root dependence for DED currents $I_{DED} > 1\,\mathrm{kA}$. In comparison with figure 6.8 this is strongly correlated with the trend of n_e. Three mechanisms can cause this effect: (a) a non-linear behavior of the geometrical dimensions of the laminar flux tubes and therefore the magnetic topology, (b) an increased radial transport from the region with stochastically distributed field lines to the short connection length flux tubes smearing out the modulation, (c) local recycling at the DED target of hydrogen, which is increased by 15%, leads to a radial inward directed flux filling the flux tube with ionized particles from this remote area (compare fig. 6.6).
It can be also seen that this pressure drop is in general lower for a radially inward position

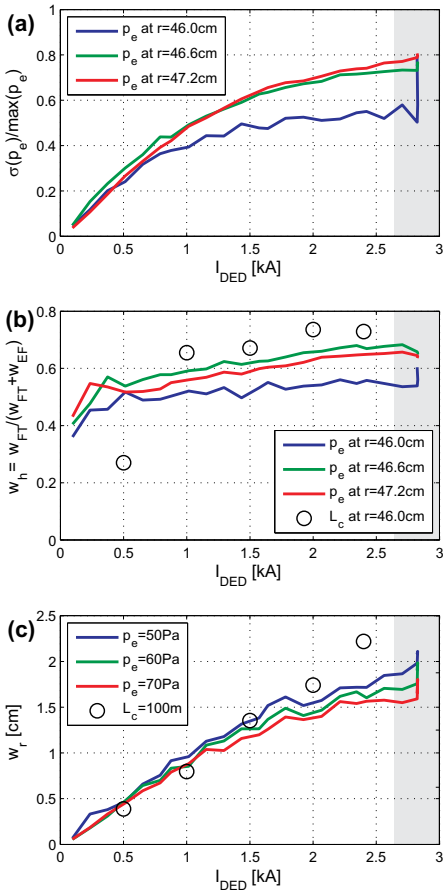

Figure 6.10: Relative modulation depth $\sigma(p_e)/\max(p_e)$ (a), normalized helical width w_h (b) and radial width w_r (c) as a function of the DED current amplitude for constant pressures p_e (solid lines) and the shortest connection length L_c (◯), respectively (#110141-#110146). The particle pump out phase is marked grey.

of $r = 46.0\,\mathrm{cm}$ due to a higher maximum pressure at this position. In order to discriminate the influence of the magnetic topology from the transport effects we compare in the following the geometrical p_e modulation properties with those of the magnetic topology in terms of $L_c(r,t)$.
Having a closer look to the normalized helical width w_h of the rotating laminar flux tube (figure 6.10b), a sudden increase is observed for $I_{DED} < 0.5\,\mathrm{kA}$ continuing linearly increasing until the particle pump out occurs. In comparison with the helical width of L_c, a similar onset with a linear trend in the following is obtained. The magnetic topology in vacuum approximation shows that for low RMP amplitudes magnetic flux surfaces are only deformed. At higher perturbation the connection of magnetic field lines to the wall is established as a sudden transition and a Laminar Zone is generated resulting in a step-

wise increase of the helical width. Increasing the perturbation current further, the helical width increases linearly. This sequence resembles the measured normalized helical width of the flux tube.
In addition, the radial extension or the penetration of the flux tube into the edge plasma w_r (figure 6.10c) follows the linear trend with increasing perturbation current for $I_{DED} < 1.5\,\mathrm{kA}$ but deviates from the linearity for higher DED currents. Similar to the discussion of the non-linear dependence of the density and pressure drop inside the flux tube, this effect can be explained by an increased radial transport, which in fact can smear out the modulation. As a consequence, for high RMP amplitudes ($I_{DED} > 1.5\,\mathrm{kA}$) the pressure drop inside the helical flux tube may be limited by an effectively enhanced radial transport. Additionally, the increased local recycling at the DED target of hydrogen fills the flux tube with ionized particles.
The existence of the p_e modulation in combination with the geometrical properties obtained show that the Laminar Zone exists for high RMP rotation before and during the pump out phase as observed consistently as well with static RMP fields.

6.2.3 Summary and Conclusion

In summary, we presented in this section measurements of electron density and temperature under the influence of the Dynamic Ergodic Divertor at TEXTOR, which provide substantial experimental evidence that a three-dimensional scrape-off layer is preserved for fast rotating RMP fields. In the far plasma edge at $r/a > 0.98$ a simultaneous drop of n_e and T_e and therefore a drop in the electron pressure exists before and after the onset of the particle pump out, which is coincident with a periodic change from a region with long stochastically distributed field lines to magnetic flux tubes with short connection length.
The radial and helical dimensions of the laminar flux tubes in terms of p_e increase linearly as soon as they are created for sufficient perturbation and follow the trend of the magnetic topology in vacuum approximation calculated in a quasi-static way. For high DED amplitudes finally the pressure drop inside the helical flux tube describes a square root dependence on the external perturbation strength which can be caused by both the local increase of recycling atoms at the wall and an effectively enhanced radial transport.
It was shown for fast rotating RMP fields in the direction of the intrinsic plasma rotation that the magnetic topology modeled in vacuum approximation fit to the measured edge plasma reaction at $r/a > 0.98$. Hence, it can be applied in this scenario as an approach to characterize the outermost perturbed plasma edge layer and its impact for plasma surface interaction studies at the TEXTOR tokamak.
In how far the plasma structure depends on the relative rotation between RMP field and plasma fluid rotation and therefore deviates from the expected magnetic topology in vacuum approximation is matter in the following in section 6.3.

6.3 Rotation Dependence of Electron Density and Temperature Fields in the Plasma Edge

The penetration process of the RMP field is determined by internal plasma response currents, which are established depending on the interplay between pressure gradient, resistivity and toroidal rotation of the plasma (section 5.5). In the following, the rotation dependence of the edge plasma structure in terms of electron density and temperature fields will be studied by changing the relative rotation between external RMP field and toroidal plasma fluid rotation [85].
The investigations with rotating RMP fields rely on findings with static RMP fields, which were summarized in section 5.4. In particular, it was shown for static RMP fields that the Laminar Zone imposes a modulation to the $n_e(r,\Theta)$ and $T_e(r,\Theta)$ fields along the poloidal angle Θ [67, 65]. This modulation was shown to be preserved for fast rotating RMP fields at the radial position of the Laminar Zone in section 6.2 and radially inward at the next rational flux surface in section 6.1. In the following we extend this results and demonstrate that a modulation in both n_e and T_e at $r/a > 0.9$ exists but that depending on the relative rotation the electron density modulation appears to be shifted with respect to the expected position modeled in vacuum approximation (section 6.3.2). In section 6.3.3 a pronounced phase delay Φ between n_e and T_e will be shown to exist, which in fact is a function of the radius. This phase delay Φ is shown to vanish with increasing RMP amplitude for low relative rotation frequency between the RMP field and the plasma fluid only but is maintained for high relative rotation. This phase delay Φ will be compared with results from EMC3-EIRENE modeling in order to develop an idea for the underlying magnetic topology. The interpretation will be extended to more detail in section 6.3.4 by investigating the plasma edge structure for different relative rotations by a detailed analysis of the electron density $n_e(r)$, temperature $T_e(r)$ and pressure $p_e(r)$ profile reactions and by relating them to the local magnetic topology. This enables a comparison of the experimentally determined magnetic topology to the one modeled in vacuum approximation without screening effects as well as to the drift-fluid model including plasma response described in section 5.5.

6.3.1 Experimental Scenario

The experiments were performed at TEXTOR with a DED field applied with poloidal/toroidal base mode numbers $m/n = 3/1$, a low order electro magnetic multi-pole and therefore high resonant field amplitudes in the plasma edge layer. We analyze a highly resistive (edge electron collisionality $\nu_e^* > 4$) ohmic plasma with circular shape and limited on the DED target. Two opposite RMP rotation frequencies of $\nu_{DED} = +/-974\,\mathrm{Hz}$ were used where the sign of the rotation direction is defined in the direction of the electron diamagnetic drift direction $\vec{\omega}_{ed}$. Technically, the change of the rotation direction is realized by changing the relative phase between the AC currents in the DED coils from $+\pi/2$ to $-\pi/2$. Here, the positive sign results in a helical rotation with a toroidal component in the

direction of the toroidal magnetic field B_t whereas the negative sign describes the counter B_t rotation direction. This yields two rotation cases: *low relative rotation* will refer to RMP field rotation parallel to $\vec{\omega}_{ed}$, i.e. co-B_t, and hence a relative rotation frequency of $f_{rel} = -0.2\,\mathrm{kHz}$. *High relative rotation* will refer to RMP rotation in opposite direction, i.e. counter-B_t, with $f_{rel} = +1.8\,\mathrm{kHz}$.
The global plasma parameters in the core/edge are: electron density $n_e(R = R_0) = 2.0{\cdot}10^{19}\,\mathrm{m}^{-3}$, $n_e(r/a = 0.92) = 8.0{\cdot}10^{18}\,\mathrm{m}^{-3}$, electron temperature $T_e(R = R_0) = 1.0\,\mathrm{keV}$, $T_e(r/a = 0.92) = 60\,\mathrm{eV}$, plasma radius $a = 45.6\,\mathrm{cm}$, edge safety factor $q_a = 4.8$. At the rational flux surface $q = 4$ a electron drift frequency of $f_e^* \approx 1.5\,\mathrm{kHz}$ in the poloidal direction is measured, which is an order of magnitude larger than the poloidal component of the DED rotation and the poloidal plasma rotation and therefore not important here in terms of resonance effects to the electron fluid drift. Therefore, we stick to the toroidal RMP rotation ν_{DED} and the toroidal plasma rotation to quantify the relative rotation f_{rel} for the remainder of this chapter.
All global parameters were kept constant during the RMP field application with an amplitude of $I_{DED} = 1\,\mathrm{kA}$. No changes in the global plasma parameters and in the MHD spectrum, e.g. no indications for an $n = 1$ tearing mode [20] were observed. The toroidal rotation frequency was measured with Charge Exchange Recombination Spectroscopy (CXRS) [86] and the radial profile of the plasma rotation frequency appears to be flat over a wide radial range of $0.50 < r/a < 0.85$ within the error bars. It is important to note that the plasma rotation can be changed locally at the rational flux surfaces due to the RMP fields in general [82, 93]. However, the radial range of the measurements described in the following is not captured by the CXRS diagnostic. Therefore, the outermost detected, i.e. closest measurement position for the toroidal rotation at $r/a = 0.85$ and will be treated as a global parameter. The toroidal rotation frequency increases for both RMP rotation directions linearly with the RMP strength up to $\Omega_{plasma,tor} = v_{tor}/R = +5\,\mathrm{kHz}$. This is compatible with the finding with static RMP field that the RMP amplitude drives the toroidal rotation due to an open, stochastic edge layer causing additional electron losses which are balanced by a radial ion current. This current causes an increase of the toroidal rotation by $\vec{j} \times \vec{B}_{toroidal}$ forces [94] and seems to exist as well under the impact of rotating RMP fields supporting the interpretation of the results in conjunction with an open perturbed edge layer with a helical 3D SOL.
The $n_e(r,t)$ and $T_e(r,t)$ fields within $r/a = 0.9 - 1.05$ are measured by the Supersonic Helium Beam diagnostic (SHE) (section 4.2).

6.3.2 Rotation Dependent Shift of the Edge Plasma Structure Relative to the Magnetic Topology in Vacuum Approximation

Figures 6.11a-d show measurements of the normalized electron density $\tilde{n}_e(r,t)$ and temperature $\tilde{T}_e(r,t)$ fields obtained with the SHE diagnostic during application of a fast rotating DED field with a rotation frequency of $\nu_{DED} = +/-\,974\,\mathrm{Hz}$ and hence low/high relative rotation. Both $\tilde{n}_e$ and $\tilde{T}_e$ are normalized to its mean values $\bar{n}_e$ and $\bar{T}_e$: $\tilde{n}_e = (n_e - \bar{n}_e)/\bar{n}_e$ and $\tilde{T}_e = (T_e - \bar{T}_e)/\bar{T}_e$. The DED period $\tau_{DED} = 1/\nu_{DED}$ is employed

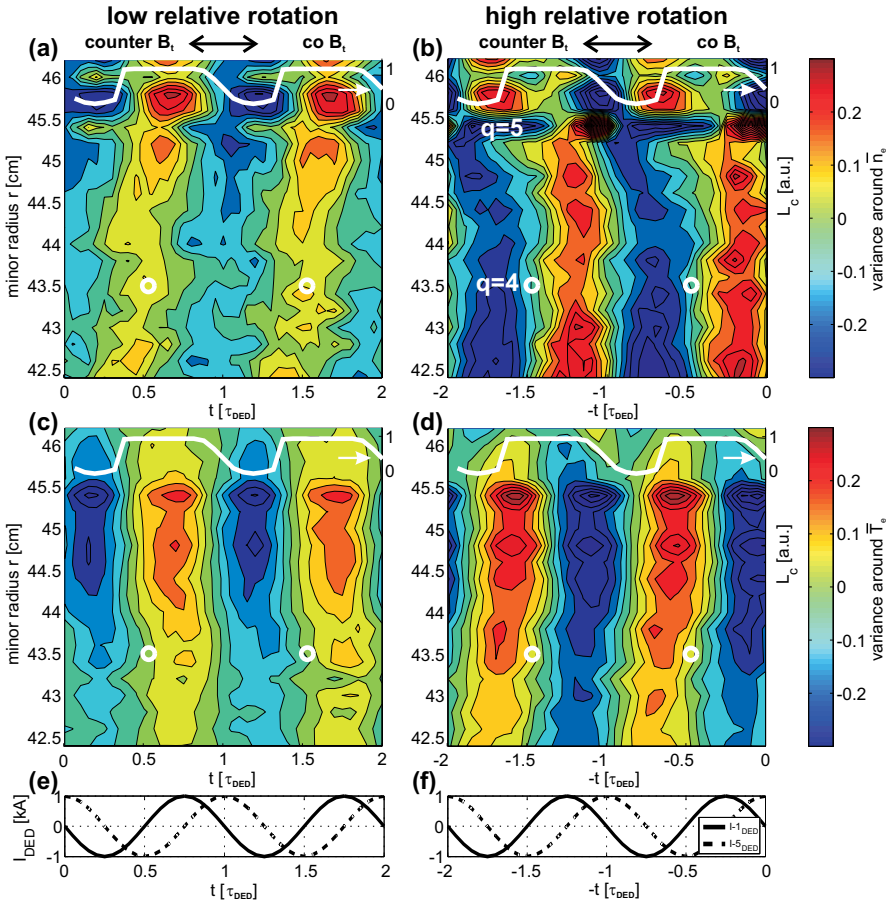

Figure 6.11: Normalized electron density (upper row) and electron temperature (lower row) as a contour plot versus the minor radius and time (normalized to the DED rotation period τ_{DED}) for low relative rotation ($f_{rel} = -200\,\mathrm{Hz}$, left column) and a high relative rotation ($f_{rel} = +1800\,\mathrm{Hz}$, right column). The sinusoidal current distribution of the DED power supplies I-1 and I-5 is plotted in (e) and (f). Note the time axis transformation for the high relative rotation case: $t \rightarrow -t$, necessary due to the opposite DED current rotation direction. The position of the O-point at the rational flux surface $q = 4$ calculated in vacuum approximation is marked (◯). The time trace of the direct connection length L_c in poloidal turns to the wall from the measurement position at $r = 46\,\mathrm{cm}$ is depicted as white line.

as time axis and data are shown for two DED periods. A clear modulation of $\tilde{n}_e$ and $\tilde{T}_e$ is observed induced by the rotating RMP field for comparable discharges as in section 6.2. This provides evidence that the plasma edge structure revealed for static RMP, i.e. poloidally modulating $n_e(\Theta)$ and $T_e(\Theta)$ fields, is preserved but rotates now with the RMP rotation frequency. However, we will show that there is a clear impact of the relative rotation between external RMP field and toroidal plasma fluid rotation on the modulation suggesting a dependence of the magnetic topology on the relative rotation level.

In order to compare both rotation directions directly, we show the sinusoidal current distribution of the DED power supplies I-1 and I-5 for $\nu_{DED} = +974\,\mathrm{Hz}$ in figure 6.11e and for $\nu_{DED} = -974\,\mathrm{Hz}$ in figure 6.11f. Note that for the RMP rotation case in counter-B_t direction, the time axis in figures 6.11b,d and f are transformed as $t \rightarrow -t$. This allows to display the same current distribution for both rotation directions due to the invariance of the DED input current waveforms $I \propto sin(2\pi\nu_{DED}t + \phi_0)$ on transformation of both $\nu_{DED} \rightarrow -\nu_{DED}$ and $t \rightarrow -t$. Intuitively, without including plasma response effects, one would expect in this display that the n_e and T_e modulations look the same for both DED rotation direction as the current distribution is exactly the same.

To compare the density and temperature modulations with the rotating local magnetic topology modeled in the quasi-static vacuum approach, i.e. with a stepwise application of the sinusoidal current distribution, the total connection length L_c of field lines from wall to the wall is calculated and plotted as an overlay at the radial position $r = 46\,\mathrm{cm}$ (compare section 5.2). For the low relative rotation case in figure 6.11a,c, both $n_e(t)$ and $T_e(t)$ are found to be modulated in phase with the connection length time trace $L_c(t)$. At the minimum in $L_c(t)$ a reduction of n_e, T_e and therefore a pressure drop $p_e \propto n_e T_e$ is found. This in-phase modulation shows that a Laminar Zone exists consisting of alternating laminar flux tubes and fingers with stochastically distributed field lines and is compatible with the experimental findings of section 6.2. For the high relative rotation case (figure 6.11b,d), both the n_e and T_e minima are found to be shifted by a quarter period or $\pi/2$ to smaller numbers of t and therefore in co-B_t direction. This provides for the first time direct experimental evidence that the Laminar Zone detected in section 6.2 still exists but is shifted for the high relative rotation case by $\pi/2$ with respect to the magnetic topology modeled in vacuum approximation. We will show in the following that the position of this outermost edge layer (Laminar Zone) is determined by the local magnetic topology at the next inward rational flux surface.
As shown in figure 6.12, a fragmented remnant island appears in the magnetic topology in vacuum approximation. The position of the O-points (OP) of this remnant island chain is calculated and overlayed at the rational flux surface $q = 4$ in figure 6.11 as white circles ($\bigcirc$). We detect one modulation in n_e and T_e per DED period evidently with one rotating O-point due to the $n = 1$ symmetry chosen in $m/n = 3/1$ base mode. For the low relative rotation case (figure 6.11a) the n_e maximum matches the calculated OP position, while for the high relative rotation case the calculated OP is located in between the n_e

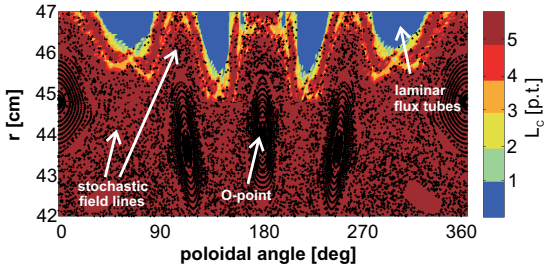

Figure 6.12: Magnetic topology calculated in vacuum approximation for a static RMP field. The complete connection length L_c in poloidal turns (p.t.) is displayed color-coded and the field line distribution as a Poincare plot.

minimum and maximum. The shift of the n_e maximum by $\pi/2$ at the rational flux surface $q = 4$ in co-B_t direction gives experimental evidence that a new shifted magnetic topology exists for increased relative rotation, which deviates from the magnetic topology modeled in vacuum approximation as we have suggested in Ref. [84]. Moreover, the shift of the plasma structure in terms of $n_e(t)$ and $T_e(t)$ at the last rational flux surface is correlated to the position of the Laminar Zone in general. In vacuum approximation this coupling is intrinsically given [51] and seems to be preserved in the high rotation case for a shifted magnetic topology. On this experimental basis, it will be investigated in section 6.4, in how far this shift of the plasma structure persists toward the vicinity of the DED coils.

These experimental findings are compatible with results from the 4-field drift-fluid model described in Ref. [79] (compare section 5.5). Here, for low RMP amplitudes screening currents are predicted in a self-consistent way at the position of the O- and X-point in opposite directions. This results in an internal radial magnetic field counter-acting the external RMP field, which can in turn (1) weaken the total RMP field and (2) results in a new magnetic topology shifted by maximum $\pi/2$ in the co-B_t direction depending on the level of screening of the external RMP field. The new topology was modeled for $m/n =$

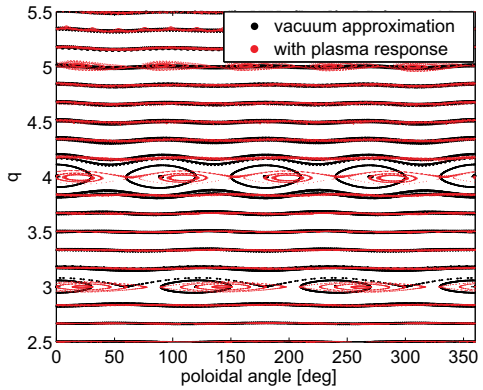

Figure 6.13: Magnetic topology modeled with field line tracing in (a) vacuum approximation and (b) with plasma response (compare section 5.5).

$3/1, 4/1, 5/1$ mode numbers and initial plasma parameters $n_e(q = 4) = 5.7 \cdot 10^{18}\,\mathrm{m}^{-3}$, $T_e(q = 4) = 52\,\mathrm{eV}$ and $\nabla_r p_e(q = 4) = 2200\,\mathrm{Pa/m}$. The model considers zero relative rotation: $f_{rel} = 0$. For high RMP amplitudes no screening of the external radial magnetic field is present and the vacuum approximation holds. Therefore, we compare in figure 6.13 for low RMP amplitude the vacuum magnetic topology to a topology with fully compensated external field in figure 6.13. We detect that an $m/n = 4/1$ island appears to be shifted by $\pi/2$ with respect to the one with full RMP penetration. Moreover, due to intrinsical coupling of modes on neighbored flux surfaces, a small island appears at the $q = 5$ surface. This might correlate to the shifted maximum of $\tilde{n}_e$ in figure 6.11b at the $q = 5$ as being also the position of the last closed flux surface in the unperturbed case.
Hence, this modeling shows that a screening of the external RMP field leads to a new shifted magnetic topology which can potentially explain the rotation dependent shift of the density modulation. In the following, a detailed analysis of the modulation properties will be presented. Together with a detailed analysis of the profile reactions in comparison with transport modeling results this will provide substantial experimental evidence on the underlying local magnetic topology for both relative rotation cases which can be correlated to a potential screening effect at high relative rotation or low RMP field amplitude.

6.3.3 Comparison of Electron Density and Temperature Modulations to the Magnetic Topology in Vacuum Approximation

In order to get first experimental evidence of the plasma structure in conjunction with the local magnetic topology, we focus on the modulation characteristics between $n_e(t)$ and $T_e(t)$. In Ref. [84], we introduced a phase delay Φ between n_e and T_e as a relative quantity independent of the actual OP and XP position with respect to the one in vacuum approximation.

Focussing again on figures 6.11a and 6.11c (section 6.3.2), we observe for the case with low relative rotation a clear modulation of $\tilde{n}_e$ and $\tilde{T}_e$ coherent with the DED period and we detect that $\tilde{n}_e$ and $\tilde{T}_e$ increase simultaneously at $t = 0.7 \cdot \tau_{DED}$ with only a small phase delay Φ between n_e and T_e of $\Phi < 60°$ at $r = 43.6\,\mathrm{cm}$. In contrast, the high relative rotation case shown in figure 6.11b and 6.11d reveals a clear shift of the $\tilde{n}_e$ maximum toward $t = -1.2 \cdot \tau_{DED}$ while the $\tilde{T}_e$ maximum remains at $t = -1.7 \cdot \tau_{DED}$. This corresponds to a phase delay between $\tilde{n}_e$ and $\tilde{T}_e$ of $\Phi \approx 180°$ at a radius of $r = 43.6\,\mathrm{cm}$.
In order to approach explanation of this phase delay we compare the experimental findings to the fluid plasma and kinetic neutral transport code package EMC3-EIRENE (see section 5.3). This code employs a three-dimensional field aligned grid calculated in vacuum approximation. With this attempt we assume a rotation of a magnetic topology similar to the static case without field screening. However, it allows to study directly the relation between n_e, T_e and the magnetic topology.
The numerical analysis of a similar discharge showed that the phase Φ between the n_e and T_e waveforms of a cut in the toroidal direction depends on the local topological

domain. We extract toroidal cuts at two characteristic domains: (a) Laminar Zone and (b) remnant island (compare figure 5.5 in section 5.4). Figure 6.14 depicts a modulation of the modeled $n_e(\phi)$ and $T_e(\phi)$ profiles along the toroidal angle ϕ. The toroidal profile at the radial position of the Laminar Zone (figure 6.14a) shows a simultaneous drop in n_e and T_e and hence a phase $\Phi \to 0$. In contrast, a counter modulation ($\Phi = \pi$) at the location of a remnant island chain (figure 6.14b) is seen.

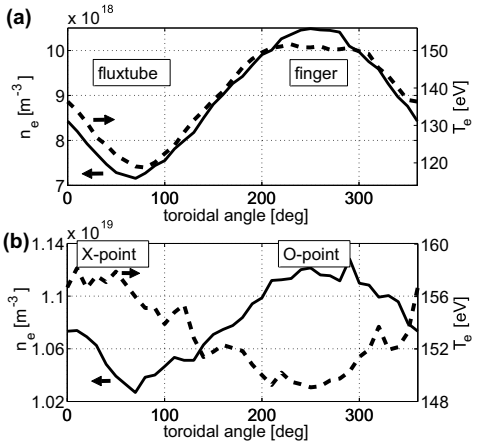

Figure 6.14: Toroidal profiles of n_e (solid line, left axis) and T_e (dashed line, right axis) modeled with EMC3-EIRENE in vacuum approximation through the Laminar Zone (a) and through a remnant island chain (b) in $m/n = 3/1$ base mode configuration.

To understand the physics reason for the counter modulation the heat and particle transport of a remnant island has to be considered which is matter of present research. Based on the EMC3-Eirene results, we focus first on the transport properties around a magnetic island with no contact to the plasma edge, e.g. in the core, as sketched in figure 6.15a (cp. discussion in section 6.1.1 for a magnetic island due to a tearing mode) [88, 89, 90, 95, 96]. The magnetic island changes the unperturbed equilibrium locally and leads to sub-volumes with closed flux surfaces at the so-called O-point (OP). Both heat and particles are transferred from the core by cross-field transport $\Gamma_\perp$, $q_\perp$ via deformed closed flux surfaces and reach the island. At the position of the O-point (OP) the flux surfaces are short-cut over a certain radial extension which lead to fast effective radial transport $\Gamma_\parallel$ around the island parallel to the short-cut flux surfaces. Therefore, gradients over the extension of the island are decreased as here only cross-field transport realizes transport into, out and through the radial domain of the island. For fixed plasma parameters at the edge this is supposed to result in a decrease of both density and temperature locally at the OP position. Assuming these transport properties we would expect no phase shift between n_e and T_e.

For a remnant island [97, 98, 99] with broken flux surfaces at the island's X-point and good flux surfaces close to the O-point as sketched in figure 6.15b, additional effects have

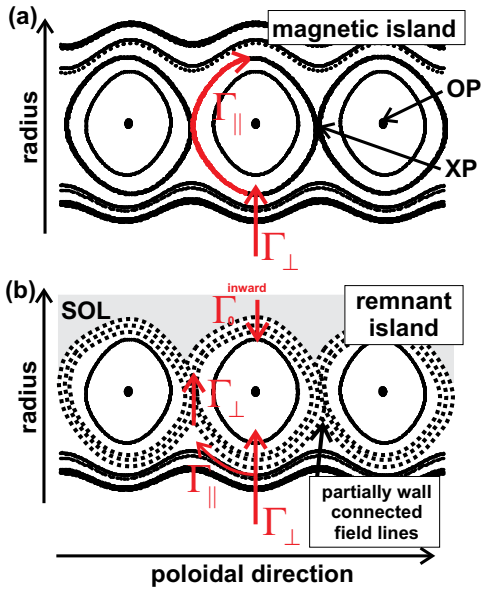

Figure 6.15: Sketch of the expected transport properties of a magnetic island with closed flux surfaces (a) and of a remnant island with stochastic field lines connecting partially to the wall and close contact to the SOL.

to be considered. Here, stochastically distributed field lines with partially connection to the wall exist with close contact to the surrounding Scrape-off layer (SOL). For limiter tokamaks as TEXTOR the SOL is almost transparent to recycling particles and neutrals which can reach the remnant island and cause ionization sources there. This source layer is magnetically connected to the remanent island and hence direct fueling by a thermal force driven by a temperature gradient can cause a radially inward directed particle transport (Γ^{inward}) into the OP of the island: The density in the island can be sufficient high in comparison to the density in the SOL to cause a transport of particles from the wall close to the island so that particles enter the island.
At the OP the density gradient is flat due to the closed flux surfaces so that penetrating particles are not released anymore from the OP area. Hence, particles from the SOL are confined locally at the OP which leads to an increase in density. At the XP, however, parallel loss channels to the wall exist which yield a local reduction of the plasma density. The considerations discussed above provide a reasonable explanation for the counter modulation of n_e and T_e as a result of the EMC3-EIRENE code, which balances these physical processes and in particular account for the sources in the edge.

Based on the basic results provided by EMC3-EIRENE modeling, we use for the interpretation of the measurement the phase delay Φ as an indicator for the locally dominant topological domain and define $\Phi \to 0$ as Laminar Zone and $\Phi \to \pi$ as a region with dominant remnant islands. In the following we will use the latter interpretation to

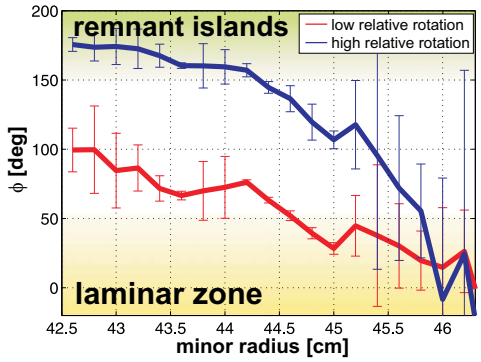

Figure 6.16: Phase Φ between n_e and T_e as a function of the minor radius for low relative rotation ($f_{rel} = -0.2\,\mathrm{kHz}$, #104741, red line) and high relative rotation ($f_{rel} = +1.8\,\mathrm{kHz}$, #104739, blue line).

discuss the Φ as a function of the minor radius.

A clear radial dependence of $\Phi(r)$ is observed experimentally as shown in figure 6.16 and the gradient of $\Phi(r)$ exhibits a rotation dependence. The error bars represent the statistical variations of the Φ within time interval used for averaging. For both relative rotation levels, a phase $\Phi \approx 0$ is observed for $r > 46\,\mathrm{cm}$, where the laminar zone is present in modeling and formed in agreement to the interpretation above also in the experiment. For the low relative rotation case, $\Phi(r)$ increases up to $\Phi(r) = 100°$ at $r = 42.5\,\mathrm{cm}$ indicating that the magnetic topology in this radial direction changes from a SOL laminar flux tube layer towards remnant islands as inner boundary of the stochastic edge layer, which is expected from vacuum field line tracing. However, increasing the relative rotation leads to a stronger gradient $\nabla\Phi(r)$ which provides evidence based on the EMC3-EIRENE modeling results that here the magnetic islands are still preserved, not yet broken up and therefore not transformed into laminar flux tubes as occurring for low relative rotation at this radial position. In this interpretation, the low relative rotation case is dominated by laminar flux tubes and the high relative rotation case by remnant islands. This gives substantial evidence that - depending on the relative rotation - a new and shifted magnetic topology exists which results in shifts of the n_e and T_e fields.

In order to relate these experimental findings to the magnetic topology, we simulate a potential damping of the RMP field in the plasma by modeling of the perturbed topology in the detection volume in vacuum approach for different RMP currents as shown in figure 6.17. The perturbed topology for three different perturbation currents $I_{DED} = 0.5, 0.75, 1.0\,\mathrm{kA}$ is shown as color coded contour plot of the field line connection length L_c from wall to wall with a Poincare plot as an overlay. The measurement position of the SHE diagnostic is highlighted grey. We find that with a perturbation as applied in the experiment, a region with stochastic field lines with a broad Laminar Zone ($L_c < 3$ poloidal turns) at $45.5 < z < 47\,\mathrm{cm}$ develops in the observation volume. This shows that at low rotation and comparably high DED amplitude the interpretation of no phase shift

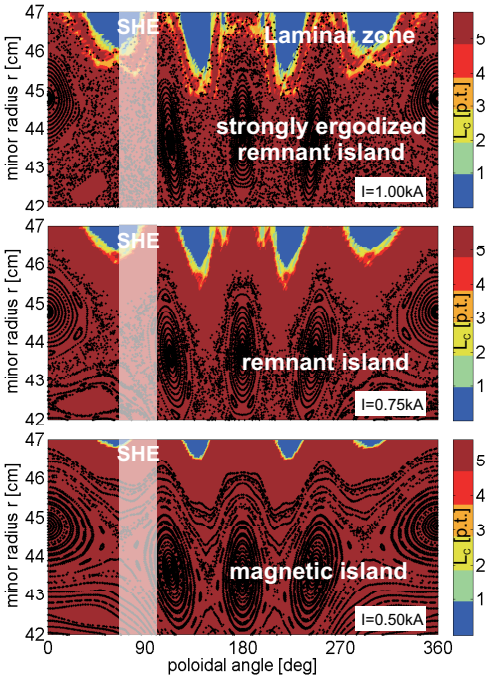

Figure 6.17: Modeled magnetic topology with the ATLAS code (Refs. [51, 67]) in vacuum approximation for different DED currents in coordinates of the minor radius r versus the poloidal angle. A Laminar plot is shown with an overlayed Poincare plot. The position of the SHE diagnostic is highlighted grey.

in the Laminar Zone and an increasing phase shift for occurrence of remnant islands which was extracted from static 3D fluid modeling provides a reasonable explanation. However, the experimental measurement at higher rotation suggests that the radial domain of the Laminar Zone shrinks and the remnant island layer seems to be extended towards the edge. The same characteristics are seen in the magnetic field line tracing for a globally damped RMP field in reducing the DED current. In this case the resonant islands on this flux surfaces are not broken up and accordingly the stochastic region is replaced by remnant islands chains and finally a intact magnetic island with closed flux surfaces. At the same time the radial extension of the Laminar Zone decreases. Taking into account the modeling results with EMC3-EIRENE, a damping of the RMP amplitude and therefore a changeover of the magnetic topology from the Laminar Zone to a magnetic island is expected to result in a changeover of the phase delay between n_e and T_e.
This interpretation provides for the high rotation case first direct experimental evidence for a damping of the external RMP field inside the plasma edge. The latter changes the magnetic topology in such a way that the Laminar Zone is not generated but magnetic islands are present as expected only for a smaller local resonant amplitudes.

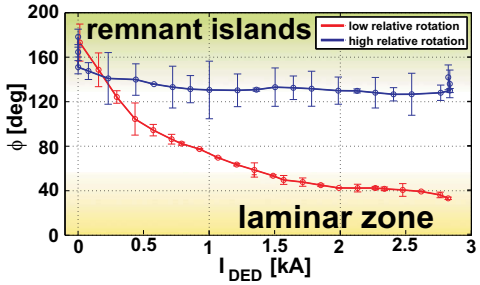

Figure 6.18: Phase Φ between n_e and T_e (solid line, left axis) as a function of the external RMP current I_{DED} for low relative rotation ($f_{rel} = 5\,\text{kHz}$, #110141-#110146, red line) and high relative rotation ($f_{rel} = 7\,\text{kHz}$, #110247-#110251, blue line) at the rational flux surface $q = 5$.

This process of net reduction of the external field due to internal plasma response currents is in qualitative agreement with the 4-field drift-fluid model described in Ref. [79]. However, for higher external perturbation current, a break-down of the response currents which damps the resonant components on the rational flux surface is predicted by the model. This is also found by analysis of the dependence of $\Phi(I_{DED})$ on the perturbation level and for RMP rotation frequencies of $\nu_{DED} = +/-\,974\,\text{Hz}$. The plasma scenario was adjusted with counter neutral beam injection and co-current torque input in order to reach a higher toroidal plasma rotation frequency of $\Omega_{tor} = +6\,\text{kHz}$. Figure 6.18 shows the dependence of $\Phi(I_{DED})$ at the rational flux surface $q = 5$ on the DED current I_{DED} for the low relative rotation ($f_{rel} = 5\,\text{kHz}$) and the high relative rotation case ($f_{rel} = 7\,\text{kHz}$). For high relative rotation (blue), Φ stays constant at $\Phi = 140°$ indicating that a shifted magnetic island is present independently of the DED current. In contrast, for low relative rotation (red) Φ decreases with increasing I_{DED} from $\Phi = 180°$ to $\Phi = 35°$. This provides evidence for breaking up the outermost $q = 5$ magnetic island chain forming a Laminar Zone. At high perturbations ($I_{DED} > 1.5\,\text{kA}$) finally a pure short connection length layer (Laminar Zone) is developed suggested by a vanishing phase delay.

6.3.4 Identification of the Local Magnetic Topology by Density, Temperature and Pressure Profile Reactions

To analyze the transport properties of the plasma structure and to deduce the local magnetic topology in more detail, figure 6.19 shows radial profiles of $p_e(r)$, $n_e(r)$ and $T_e(r)$. These profiles are extracted at those times, when the density $\tilde{n}_e(t, q = 4)$ has its minimum or maximum at the $q = 4$ surface. This corresponds for the low relative rotation case to radial profiles at $t_{max(n_e)} = 0.6 \cdot \tau_{DED}$ and $t_{min(n_e)} = 1.1 \cdot \tau_{DED}$ and for the high relative rotation case at $t_{max(n_e)} = -1.2 \cdot \tau_{DED}$ and $t_{min(n_e)} = -0.7 \cdot \tau_{DED}$. Due to the application of the conditional averaging method proposed in section 4.4, the statistical errors of the profiles are reduced to $\sigma(n_e)/n_e = 10\%$, $\sigma(T_e)/T_e = 7\%$ and $\sigma(p_e)/p_e = 1\%$.

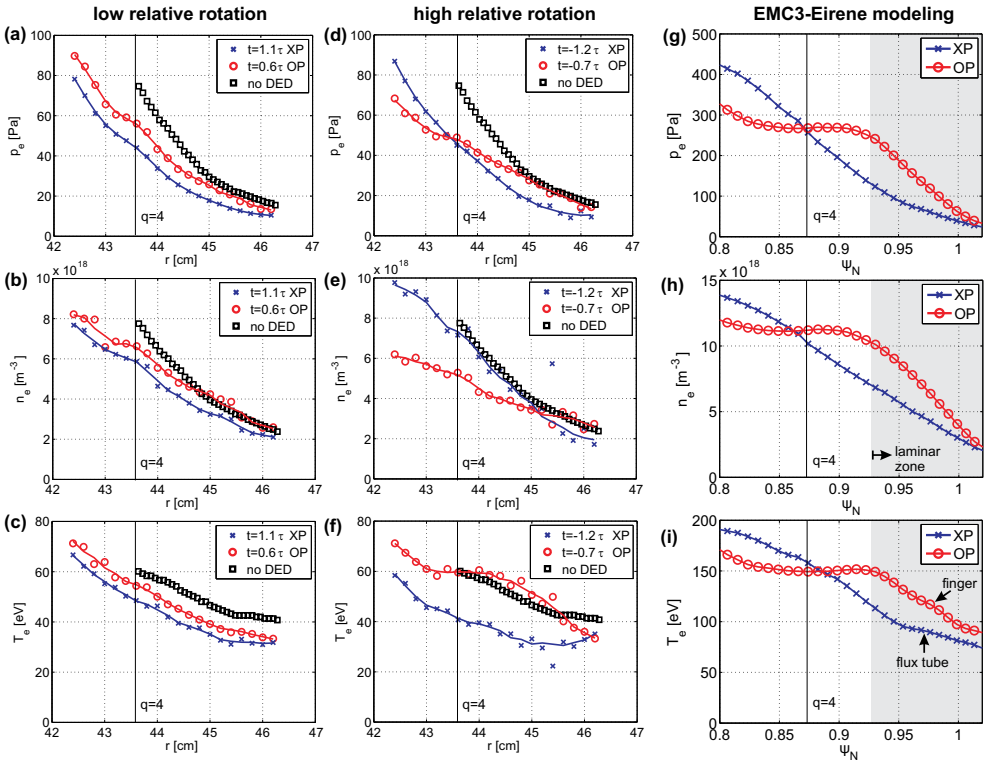

Figure 6.19: Radial profiles of electron pressure p_e (upper row), density n_e (mid row) and temperature T_e (lower row) measured with low relative rotation ($f_{rel} = -200\,\mathrm{Hz}$, left column) and high relative rotation ($f_{rel} = +1800\,\mathrm{Hz}$, mid column) and calculated with the EMC3-EIRENE code (right column). The measured profiles (a-f) are extracted for times with maximum and minimal density at the $q = 4$ surface.

In general, the average values of n_e, T_e and p_e along a flux surface are reduced with respect to the no-RMP case for both relative rotations as soon as the DED field is applied. However, the absolute local reduction and the radial gradient depends on the radius, the time within a rotation period and therefore on the local magnetic topology. In the following, profile reactions will be analyzed in detail and compared to the ones calculated with the EMC3-EIRENE code based on the magnetic topology in vacuum approximation.

We will focus on the **low relative rotation** case first (figures 6.19a-c), where the O-point position calculated in vacuum approximation matches the density maximum. In the radial range $r > 45\,\mathrm{cm}$, n_e and T_e and therefore p_e drop simultaneously by $\Delta n_e = -20\%$, $\Delta T_e = -25\%$ and $\Delta p_e = -40\%$ for $t = 1.1\tau_{DED}$ and $\Delta n_e > -3\%$, $\Delta T_e = -13\%$ and $\Delta p_e = -15\%$, respectively, for $t = 0.6\tau_{DED}$. This is consistent with the discussion in section 6.2, where we concluded from a correlated modulation of n_e and T_e with the connection length L_c that a rotating Laminar Zone exists. The reduction of the

parameters was also measured with static RMP fields at TEXTOR [65] and we extended these results toward rotating RMPs in section 6.2. Short connection length flux tube were found to cause a strong reduction in both n_e and T_e due to a strong parallel transport to the wall. In contrast, finger structures with stochastically distributed field lines were dominated by diffusive transport and lead to less reduction. This behavior is reproduced by EMC3-EIRENE modeling of the plasma parameters in this radial range. Figure 6.19 shows the modeled radial profiles of electron density (g), temperature (h) and pressure (i) as a function of the normalized flux coordinate Ψ_N for a magnetic topology in vacuum approximation similar to the experiment in $m/n = 3/1$ base mode configuration. Profiles are extracted at the island's OP and XP position. A strong reduction of all parameters is found to be present in the radial range of the Laminar Zone at $\Psi_N > 0.93$ for laminar flux tubes being in qualitative agreement with the experimental results.

Radially inward vacuum modeling suggests - in comparison with figure 6.20 - a remnant island chain at the $q = 4$ surface with a OP with closed flux surfaces and a strongly ergodized XP and long connection length. Experimentally, in fact all plasma parameters are measured to be reduced in the radial range $r < 45\,\mathrm{cm}$ and in particular at the $q = 4$ surface. At the calculated OP position a pronounced reduction by 25% of the no-DED reference value in p_e is observed with a localized flattening of the p_e profile. This experimental finding support a fast parallel transport around locally closed flux surfaces of the island's OP expected from vacuum modeling as discussed in section 6.3.2. In contrast, at the XP position a strong reduction of 40% in p_e is found while the gradient $\nabla p_e(r)$ is less affected. This behavior agrees with findings with static RMP fields for ergodized regions with connections to the wall, where a dominantly enhanced diffusive radial transport leads to stronger decrease of the plasma parameters and a decrease in the radial gradient [65].
Figures 6.19b and c show that the p_e profile reactions are dominantly governed by the electron density, which drops at $q = 4$ by 15% and 25% at the expected OP and XP, respectively. In contrast, T_e decreases by 9% and 20%. Hence, a larger reduction of both n_e and T_e is found to exist for the XP position than for the OP position. However, a flattening is measured in n_e while the temperature profiles decay with the same gradient. This gives direct experimental evidence that the region, where vacuum modeling suggests

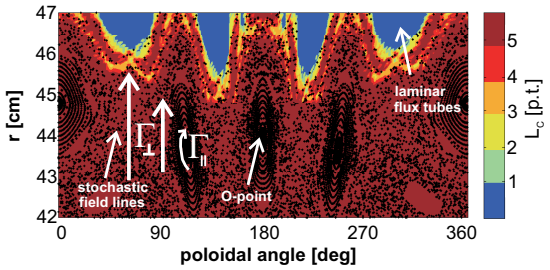

Figure 6.20: Magnetic topology calculated in vacuum approximation for a static RMP field. The complete connection length L_c in poloidal turns (p.t.) is displayed color-coded and the field line distribution as a Poincare plot.

the ergodized XP is determined by stochastically distributed and field lines with direct connection to the wall. The latter causes at the XP an enhanced loss of particles and energy due to parallel transport and therefore reduced plasma parameters in comparison to the OP. At the OP, vacuum modeling suggests closed flux surfaces around the OP with no connection to the wall. Therefore, this region is expected to be dominated by cross-field transport which would lead to a flattening of the gradient and less reduction of the plasma parameters.
This behavior is found in the n_e, T_e and p_e profile reactions consistently and agrees with findings with static RMP fields [65, 60]. In turn, the comparison of the profile reactions with the magnetic topology in vacuum approximation is compatible with the existence of a remnant island with an O-point at $t = 1.1\tau_{DED}$ and an ergodized X-point at $t = 0.6\tau_{DED}$ for the low relative rotation case.

For the **high relative rotation** case it was shown in section 6.3.2 that the modulation and therefore the entire plasma structure is shifted by $\pi/2$ in space. In the following, measured radial profiles at the shifted position will be discussed and compared to EMC3-EIRENE calculations in vacuum approximation in order to get experimental evidence about the underlying local magnetic topology. With this attempt, the transport properties of the shifted magnetic topology are assumed to be the similar to the unshifted magnetic topology as island structures still appear but are shifted in modeling with plasma response (compare fig. 6.13).
From the modulation characteristics it was initially derived in section 6.3.3 that the counter modulation of n_e and T_e can be correlated to a rotating magnetic island. This behavior is reflected in the radial profiles for $r < 45\,\text{cm}$ in figures 6.19e,f by the fact that n_e increases as soon as T_e decreases and vice versa. In contrast, for $r > 45\,\text{cm}$ an in-phase modulation is represented by a simultaneous drop both n_e and T_e. The radial profiles are again extracted at the time steps, where $n_e(t, q = 4)$ has its maximum or minimum, hence at $t = -1.2 \cdot \tau_{DED}$ and $t = -0.7 \cdot \tau_{DED}$, respectively.
We will discuss first the most obvious change in the profile shape (figure 6.19c, red ◯) in order to show that an OP of a rotating magnetic island is present at the $q = 4$ surface: At $t = -0.7 \cdot \tau_{DED}$, no global reduction but a pronounced flattening in T_e around the $q = 4$ within about 1.2 cm is detected, which is correlated with a drop in n_e of 33% and a localized peaking in p_e. The flattening in T_e can be caused by enhanced effective radial transport which can be related to the behavior of the OP of a magnetic island (compare section 6.3.3). The effect is also reproduced for a magnetic island in vacuum approximation as shown in figure 6.19i. Here, a pronounced flattening of the profile is found as well coincident with a counter-modulation of n_e and T_e, which stems consistently from the heat flux around the island's OP. This gives evidence that profiles at $t = -0.7 \cdot \tau_{DED}$ and at $q = 4$ describe the OP of an rotating magnetic island structure with a width of $w = 1.2\,\text{cm}$. The increased particle transport for this position is indicated by a reduction of n_e by 32% and a decreased gradient.
This decrease in both n_e and $\nabla n_e(r)$ is qualitatively reproduced by the simulations with the EMC3-EIRENE code shown in figure 6.19i. However, in contrast to the measurement, the profile in the calculations appears completely flat, which emphasizes a lower radial particle transport around the island in the experiment than in the modeling assumed.

The particular profile shape and the detailed waveform of the toroidal profile (figure 6.14) are matter of in how far the boundary conditions, in particular the radial transport coefficients used, match the experiment. Additionally, the absolute values of the profiles do not fit to the experimental ones as they are matter of the actual input parameters of the modeling code used. We aim at a qualitative comparison of the overall profile shape here and leave the exact reproduction of the measured profile for future work to inversely extract the local radial transport.
For the expected XP (figure 6.19e, blue $\times$), the n_e profiles at $t = -0.7 \cdot \tau_{DED}$ are not significantly affected, which gives experimental evidence that the particle transport along open field lines is not enhanced as for the ergodized XP area for the low relative rotation case. In contrast, T_e is reduced by 30% while the gradient ∇T_e remains unchanged. This effect can be explained by analyzing the p_e profiles first. In contrast to the low relative rotation case, we find p_e to be the same at the $q = 4$ surface for the OP and the XP which indicates that loss channels, e.g. by field lines with short connection length, have a minor effect. This is consistent with the modeling shown in figure 6.19g. As a consequence, since n_e is not affected, a drop of T_e is needed to balance p_e. Therefore, the behavior found in the profile reactions can be explained assuming the existence of a non-ergodized XP and - in combination with the discussion of the OP - the presence of an rotating magnetic island.
Further outside at $r > 45\,\mathrm{cm}$, as suggested by the modulation characteristics in section 6.2, a shifted Laminar Zone seems to exist. The in-phase modulation of n_e and T_e and therefore the pressure drop is reproduced in the radial profiles. The absolute drop of n_e, T_e and p_e in a laminar flux tube (blue $\times$) in comparison to the no RMP case is similar to the low relative rotation case. Therefore, the absolute drop in a flux tube and a finger seems to be maintained independently of the relative rotation which gives direct experimental evidence that the Laminar zone exists independently from the relative rotation. However it was shown in section 6.3.2 that the position of the Laminar Zone depends on the position of the rotation dependent plasma structure at the outermost radial flux surface. In order to meet the rotation dependent plasma parameters radially inward at the rational flux surface, the gradients of the profiles are needed to be changed. This effect explains the change in the gradient of T_e in figure 6.19f.

The detailed analysis of the profile reactions presented here are in agreement with the findings proposed in section 6.2 and support the interpretation that the low relative rotation exhibits a strongly ergodized remnant island in the detection volume as expected from the magnetic topology in vacuum approximation. In contrast, for the case of high relative rotation evidence was shown that a shifted remnant magnetic island is present, which accounts for a shift of the Laminar Zone and is borne from an apparent rotation dependent plasma response.

6.3.5 Summary and Conclusion

In summary, we have shown for the first time measurements of a modulation of n_e and T_e fields at the position of the outermost rational flux surface $q = 4$ at TEXTOR which

are coherent to the rotation frequency of an externally applied RMP field. This modulation proves that a perturbed magnetic boundary layer is imposed even with fast RMP rotations in general.
A phase delay $\Phi(r)$ between n_e and T_e was found as a function of radius r showing that the typical topological domains of a perturbed boundary with static RMP fields can be identified. In particular, a Laminar Zone with $\Phi \to 0$ at the edge exists and remnant islands with $\Phi \to \pi$ towards smaller radii. However, occurrence of either domains depends on the relative rotation between the toroidal plasma rotation and RMP field. The radial gradient $\nabla\Phi(r)$ steepens with increasing rotation which shows that the stochastic layer found at low rotation is replaced by remnant magnetic islands at higher relative rotation. A reduced phase Φ is measured with increasing perturbation current which provides in case of low rotation and high resonant field amplitude evidence for the transition to a topology resembles the vacuum magnetic modeling prediction. However, for higher rotation and/or lower resonant field amplitude, an increasing phase is measured. These observations provide direct experimental evidence that shielding of the external field takes place within this highly resistive TEXTOR edge plasma for (a) low rotation and small RMP amplitude and (b) high rotation at any perturbation strength accessible in the actual experiment.
Comparing the position of the plasma structure in terms of n_e modulation with the expected position of the magnetic topology modeled in vacuum approximation showed that for high relative rotation a shift of the plasma structure at the rational flux surface of $\pi/2$ in the toroidal direction occurs. This behavior is supported by the 4-field fluid-drift model proposed in Ref. [79] and shows that a shifted magnetic topology is present due to screening currents on the rational flux surface. The actual poloidal/toroidal position of the laminar flux tubes, however, is found to depend on the position of the local magnetic topology at the next radially inward rational flux surface, as a direct connection between the structure at the rational flux surface and the position of the Laminar Zone seems to exist. The question remains, if - as a consequence - the plasma structure at the DED target plates is also affected since here the DED near field competes with structure of the Laminar Zone. This will be studied and discussed in section 6.4.
A detailed analysis of the profile reactions at the density maximum and minimum of the modulation at a rational flux surface showed that for low relative rotation the lower reduction in n_e, T_e and p_e occurs together with a reduction of the gradient of n_e. This provides direct experimental evidence that a region with fast parallel particle transport, e.g. by locally closed flux surfaces exists. The profiles for the n_e minimum show stronger gradient of the plasma parameters which supports the existence of wall connecting field lines in this region. In combination, the analysis of the modulation properties together with the analysis of the profile reaction provides strong experimental evidence that a remnant island with short connection length field lines at the X-point and closed flux surfaces at the O-point as modeled in vacuum approximation exists. For high relative rotation of $f_{rel} = +1800\,\mathrm{Hz}$ or low relative rotation level and low RMP field strength, a profile reaction analysis in combination with EMC3-EIRENE modeling indicate the presence of a magnetic island. These results are in agreement with the discussion of the modulation properties and supports the interpretation that a remnant island appears for high relative rotation due to a damping of the external resonant field amplitude by internal plasma response. In contrast, a strongly ergodized island with short connection length to the

wall exists for low relative rotation in agreement with the vacuum approximation. The analysis of the measured radial profiles shows a qualitative agreement with the modeled profiles for a remnant island. Two effects can cause the differences: (1) The radial transport coefficients as being input parameter of the code influence the shape of the radial and toroidal profiles. The alignment of the latter parameters to match the experimental data quantitatively is beyond of the scope of this work and will be left for future. (2) The assumption may be not valid that the remnant island modeled in vacuum approximation has similar transport features than the measured one. To conclude on that, models with internal plasma response are needed to be implemented into transport codes like the EMC3-EIRENE code in future.

6.4 Rotation Dependence of Ion Fluxes in Front of Resonant Magnetic Perturbation Coils

In high temperature plasmas, a typical way to get information about the processes taking place at the plasma boundary, is the observation of a remote, RMP induced two-dimensional (2D) target pattern which is located in the divertor region or in front of the RMP coils [100, 101]. The target pattern is determined by the near field of the RMP field coils or - in case of divertor tokamaks - by the deformation of the separatrix. Measurements with static RMP fields showed a good agreement of the measured target pattern in terms of heat and particle fluxes with the magnetic footprint pattern modeled in vacuum approximation for both limiter tokamaks [65] and divertor tokamaks [100]. For a high relative rotation between plasma and RMP field, however, a shift of the magnetic topology at the last rational flux surface was found here, which was discussed in section 6.3.2 to be potentially correlated to a screening of the external RMP field. This shift was shown to continue radially outward to the Laminar Zone as sketched in figure 6.21. We will show in the following that a direct connection between the magnetic topology at the outermost rational flux surfaces and the target pattern exists. Depending on the rotation level and direction we will find the target structure to be shifted with respect to the structure expected in vacuum approximation. A correlated shift of the magnetic topology at the outermost rational flux surface is detected. These experimental findings will show that the measured target pattern is determined by the competition between the magnetic field in the vicinity of the RMP coils and the local magnetic topology at the outermost rational flux surface.

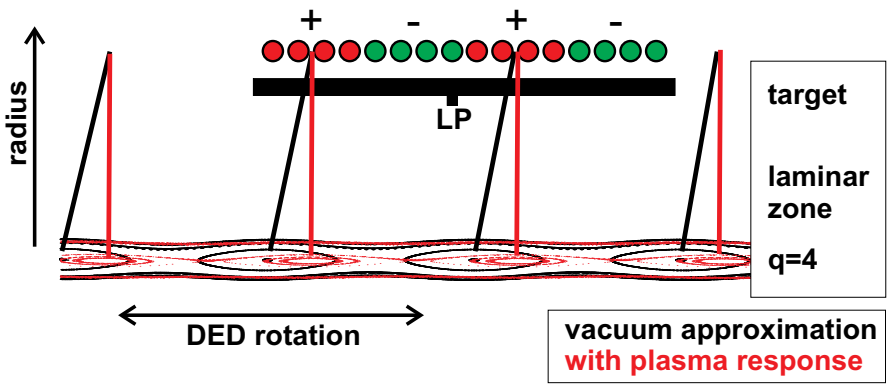

Figure 6.21: Sketch of a shifted magnetic topology at the outermost rational flux surface ($q = 4$) correlated to a potential shift of the DED target pattern. The position of a Langmuir probe (LP) is indicated.

6.4.1 Experimental Scenario

The analysis presented is performed at TEXTOR for the same experimental scenario as depicted in section 6.3.1. For diagnosing the target pattern in the vicinity of the DED coils an array of five single Langmuir probes is used (section 4.3). They are mounted at the high magnetic field side slightly below the midplane at an poloidal angle of $\Theta = 173.8°$ and at different toroidal positions ϕ around the torus. All probes are operated with negative bias voltage and measure the ion saturation current I_{sat} and hence the ion flux $\Gamma_i \propto I_{sat}$ to the probe with a time resolution of $\Delta t = 20\,\mu$s.
Figure 6.22a shows the toroidal position of the Langmuir probes (white lines) overlayed onto a modeled, rotating magnetic target footprint pattern. Therefore, the wall to wall connection length $L_c(\phi, t)$ of field lines is calculated in a quasi-static vacuum approach, i.e. by applying the sinusoidal current distribution shown in figure 6.22b to the code in vacuum approximation stepwise. With this approach we assume the vacuum approximation without internal plasma response to be valid. In order to compare both rotation direction directly, note that for the RMP rotation case in counter-B_t direction, the time axis in figure 6.22b is transformed as $t \rightarrow -t$. This enables the display of $L_c(\phi, t)$ for the same current distribution for both rotation directions due to the invariance of the DED input current waveforms $I \propto sin(2\pi\nu_{DED}t + \phi_0)$ on transformation of both $\nu_{DED} \rightarrow -\nu_{DED}$ and $t \rightarrow -t$.
Intuitively, without including plasma response effects, one would expect that the Langmuir probes measurements correlate for both DED rotation directions with the modeled target pattern shown in figure 6.22. The connection length $L_c(t)$ modulates one time per period due to the chosen $n = 1$ DED mode structure. However, the modulation of $L_c(t)$ gets delayed with decreasing toroidal angle caused by the helical setup of the DED coils. A symmetric $L_c(\phi, t)$ target pattern appears, where one DED period in time corresponds to one rotation in ϕ.

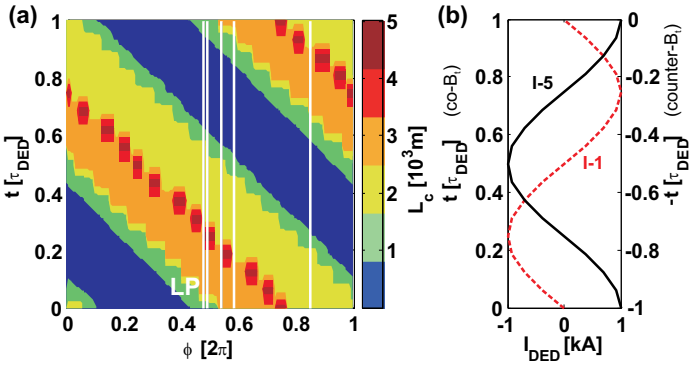

Figure 6.22: Toroidal profile of the wall to wall connection length L_c as a function of time (a) modeled in a quasi-static vacuum approach for the current distribution (b) of the DED power supplies (I-1, I-5) for both co-B_t (left axis) and counter-B_t (right axis, transformed) rotation direction. The toroidal positions of the Langmuir probes (LP) are marked in white.

6.4.2 Rotation Dependence of a Target Plasma Structure

Figure 6.23 shows the ion flux measured with one Langmuir probe at $\phi = 176.5°$. The time axis is employed in units of the DED rotation period $\tau_{DED} = 1/|\nu_{DED}|$ and two periods are shown. We will first focus on figure 6.23a, where a DED rotation of $\nu_{DED} = +974\,\mathrm{Hz}$ results in a small relative rotation between plasma fluid and RMP rotation of $f_{rel} = -200\,\mathrm{Hz}$. We detect a modulation of the ion flux, which is coherent with the DED rotation period and proofs experimentally that a plasma structure is imposed by the RMP field onto the target and rotates locked with the RMP frequency. This extends measurements described in Ref. [84], where rotating RMP fields were found to impose a modulation to electron density and temperature in the edge layer of TEXTOR. In addition a sub-modulation is measured, which gives direct experimental evidence that the local plasma structure on the target has sub-structures. Focussing on figure 6.23a, the probe to wall connection length $L_c(t)$ of field lines modeled in the quasi-static approach is overlayed as dashed line. The target ion flux modulates correlated and in-phase with the modulation of $L_c(t)$ and an increased ion flux is found for larger L_c. This extends the results obtained with static RMP fields in Ref. [102] toward fast rotating RMP fields. However, we will show that the rotating target structure appears to be shifted depending on the rotation frequency and direction of the external RMP field. In figure 6.23b, for the opposite rotation direction ($\nu_{DED} = -974\,\mathrm{Hz}$), a similar waveform of Γ_i is observed, which gives experimental evidence that a magnetic topology still exists. A global change can be observed by analyzing the average ion flux $\bar{\Gamma}_i$ with respect to the no-DED value. While for the low relative rotation case, $\bar{\Gamma}_i$

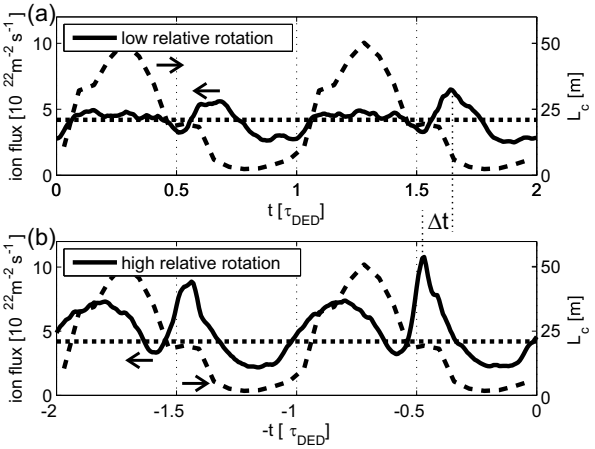

Figure 6.23: Ion flux (solid, left axis) as a function of time during application of a helically rotating RMP field in co-B_t direction [(a), low relative rotation] and counter-B_t-direction [(b), high relative rotation]. The connection length of field lines to the walls is calculated in a quasi-static approach in vacuum approximation and plotted as an overlay (dashed, right axis). The ion flux for the no-RMP case is marked by the horizontal dotted lines.

remains unchanged, an increase by 21% is measured for the high relative rotation from $\bar{\Gamma}_i = 4.2 \cdot 10^{22}\,\mathrm{m^{-2}s^{-1}}$ to $\bar{\Gamma}_i = 5.1 \cdot 10^{22}\,\mathrm{m^{-2}s^{-1}}$. Additionally to this global observation, the waveforms are changed in terms of modulation depth and gradient. With increasing relative rotation, the modulation depth $\sigma = \Delta\Gamma_i/\bar{\Gamma}_i$ with $\Delta\Gamma_i = \max(\Gamma_i) - \min(\Gamma_i)$ increases from $\sigma_{low f_{rel}} = 0.95$ to $\sigma_{high f_{rel}} = 1.67$. The slope of the modulations steepens for the peak at $t = -0.45\tau_{DED}$ and the plasma structure.
This analysis shows that the local plasma structure is changed, which basically can be caused by two coupled effects: a change in the magnetic topology and/or an perpendicular drift of ions within the magnetic topology while they arrive at the target from the core plasma. However, the modulation is found to be shifted by $\Delta t = 0.05\tau_{DED}$ to smaller numbers of t and hence in counter-B_t direction. In the tokamak geometry, this shift in time corresponds to a shift in the toroidal direction of $\Delta\phi = 360° \cdot \Delta t/\tau_{DED} = 18°$ respectively a path along the DED target of $\Delta s_{tor} = 2\pi R_{target} \cdot \Delta t/\tau_{DED} = 40\,\mathrm{cm}$ with the major radius of the target of $R_{target} = 1.27\,\mathrm{m}$. The shift measured is much larger than a drift displacement or a collisional displacement of ions (typically on scales of the ion gyro radius $\mathcal{O}(r^i_{gyro}) = \mathrm{mm}$), i.e. $\Delta s_{tor} \gg r^i_{gyro}$ and can therefore not be explained by transport effects. Hence, the measured shift in time can only be caused by a shift of the magnetic topology at the DED target position which is correlated to the shifted magnetic topology found at the outermost rational flux surface (compare section 6.3.2). This provides first experimental evidence that the magnetic field near the DED coils competes with the local magnetic topology radially inwards, i.e. at the position of the last rational flux surface. It is important to note that, although the DED coils are mounted in-vessel, a shift could potentially be caused by eddy currents in the supporting material structure and the DED target plates. It was shown in Ref. [103] that this effect is negligible for the DED frequencies and amplitudes discussed here.

In the following, the ion flux maximum of the broader peak is considered as a characteristic point of the modulation. In figure 6.24, the time t_{peak}, at which the maximum flux is reached, is plotted for multiple Langmuir probes and therefore as a function of their toroidal position. Note the inverted time axis for the high relative rotation case in order to achieve the same current distribution. The maximum of Γ_i gets delayed linearly with decreasing toroidal angle. The slope remains the same independently on the relative rotation, which proves experimentally that the helical footprint pattern and therefore the symmetry persists. The ion flux peak distribution matches for low relative rotation the long connection distribution shown in figure 6.22 and confirms therefore the correlation between the quasi-static modeled magnetic topology and the measured plasma structure for multiple Langmuir probes. However, the shift of the maximum Δt for the high relative rotation appears consistently for all Langmuir probes and proves that the plasma structure is shifted globally in counter-B_t direction.
It was shown in section 6.3.2 for the same plasma discharges that at the most outward rational flux surface $q = 4$ a pronounced shift of the measured plasma structure of $\pi/2$ is present, which was correlated to a screening of the external RMP amplitude. A coincident shift of the Laminar Zone was measured. These results - in combination with the rotation dependent shift of the target plasma structure - demonstrate experimentally that the near field magnetic topology in front of the DED coils is determined by the

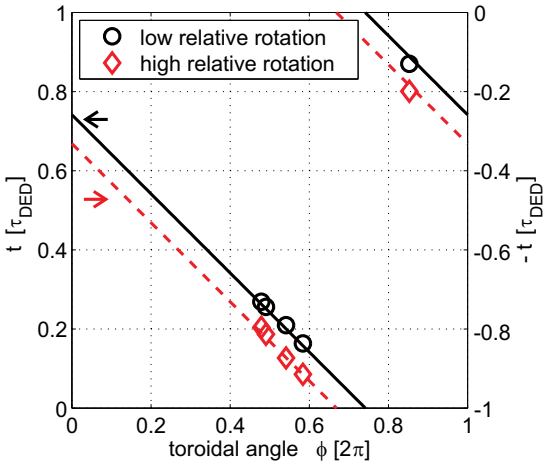

Figure 6.24: Time of maximum of ion influx Γ_i as a function of the toroidal probe position for low (solid, black, ◯, left axis) and high relative rotation (dashed, red, ◊, right axis).

competition of the DED near field and the local magnetic topology and response currents at the inward rational flux surface.
Field line tracing in vacuum approximation contains a generic property which can explain this coupling effect [51]. It was shown in particular in Refs. [104, 105] that the application of external RMP fields splits the unperturbed island separatrix at the outermost rational flux surface into stable and unstable manifolds. The manifolds define the actual trace of field lines toward the target, i.e. the magnetic target pattern which depends on the XP position of most outward island chain. The latter position is defined by the resonant components of the magnetic perturbation field on the rational surface, i.e. the external RMP field and the internal magnetic field due to plasma response. Therefore, the manifolds can be used as a sensitive indicator for the local magnetic topology at the outermost rational flux surface. The measurements show consistently that this concept inferred from vacuum approximation applies for fast RMP rotation and provides evidence that the shifted magnetic topology at the outermost rational surface defines the magnetic footprint pattern at the wall.
The fact that the shift is more pronounced at the rational flux surface ($\Delta t = 0.25 \cdot \tau_{DED}$) than at the DED target ($\Delta t = 0.05 \cdot \tau_{DED}$), gives direct experimental evidence that a "radial shear" of the magnetic topology must exist. As the magnetic field at exactly the radial position of the coils, i.e. where no plasma is present, is vacuum-like per definition, a competition between the shifted magnetic topology inside the plasma and the vacuum magnetic field outside the plasma is likely to cause this shear.

As the DED features RMP rotation with frequencies of $\nu_{DED} = 1, 2, 5\,\mathrm{kHz}$ depending on the base mode number applied (see section 3.2), we study in the following in how far the shift Δt depends depends on the RMP rotation frequency. We will show that the shift of the footprint pattern increases with the rotation frequency. Therefore, the rotation direc-

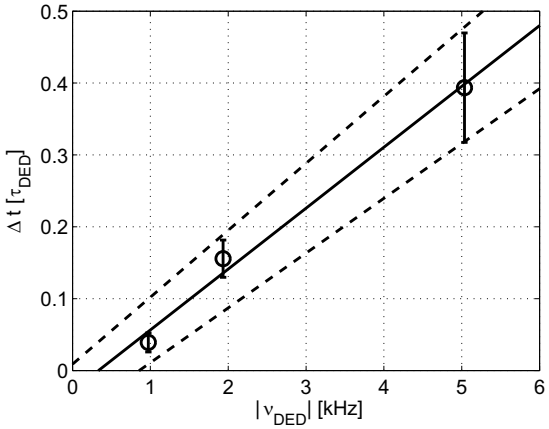

Figure 6.25: Shift Δt of the ion peak flux between co-B_t and counter-B_t rotating DED field is plotted as a function of the DED rotation frequency $|\nu_{DED}|$.

tion is changed from co to counter-B_t and the shift between the ion peak fluxes in time is measured. Figure 6.25 shows the shift Δt as a function of the DED rotation frequency $|\nu_{DED}|$ for comparable discharges. The shift is averaged over multiple periods within the flat top phase of the discharge and the error bar represents the standard deviation. The shift is given in units of the DED rotation period τ_{DED}, which corresponds to a shift in space with a toroidal component of $\Delta\phi_{tor} = 2\pi/n \cdot \Delta t$ and a poloidal component of $\Delta\phi_{pol} = 2\pi/m \cdot \Delta t$. The data point for $|\nu_{DED}| = 974\,Hz$ corresponds to the discharges discussed in figure 6.23. We find Δt to increase linearly with increasing RMP rotation frequency within the error bars, i.e. $\Delta t = (0.85 \pm 0.01) \cdot |\nu_{DED}| + (-0.03 \pm 0.04)$. The offset is within the error bar of the fit but may indicate that a small shift exist for $|\nu_{DED}| = 0$ and therefore static RMP fields. These finding motivate investigations of a potential shift of the DED target pattern during application of static DED fields in future. As a consequence, the shift disappears for an offset frequency of $\nu_{offset} = 300\,\mathrm{Hz}$. This offset may indicate that a resonance for field penetration exists at a plasma related frequency. It was shown in Ref. [106] that core tearing modes ($m/n = 2/1$) lead to a shifted target pattern and that the excitation threshold of tearing modes has its minimum for a relative rotation matching the electron diamagnetic drift frequency f_e^* [20]. This experimental result obtained for the excitation of tearing modes may be preserved also for the effect described here without tearing modes.
The question remains, how the increase of the shift with increasing DED rotation frequencies can be explained. Two possible causes may be considered: First the screening currents at the rational flux surface are supposed to increase with the RMP rotation frequency which may lead to a larger internal magnetic field competing with the near field and therefore a larger shift at the DED target. Second, screening at the radially inward rational flux surfaces, which are not directly accessible by measurements here, could also affect the near field structure.

6.4.3 Summary and Conclusion

In summary, we have shown by means of rotating resonant magnetic perturbation (RMP) fields that a rotation depend target pattern in front of the RMP coils at TEXTOR exists. The target pattern was scanned two-dimensionally in the toroidal and the helical rotation direction. A modulation was found to exist corresponding to the local magnetic topology in the vicinity of the RMP coils. However, the magnetic topology matches the one calculated in vacuum approximation only for low relative rotation between external RMP field and plasma rotation. For high relative rotation the magnetic topology is shifted. This shift is correlated to a shift of the magnetic topology radially inward at the outermost rational flux surface $q = 4$, which was explained in section 6.3 by screening effects. The shift of the target pattern appears to be less than the shift at the rational flux surface, which gives substantial experimental evidence that a competition between the vacuum-like topology and the shifted magnetic topology determined by plasma response inside the plasma exists. Independently from the rotation, the helical symmetry given by the setup was shown to be preserved. The shift increases significantly with increasing RMP rotation, which gives experimental evidence that the target pattern is either affected by increased screening currents at the rational flux surface or by an additional screening effect at rational flux surfaces radially inward. A detailed study of the local magnetic topology of more than one rational flux surface and its direct connections to the DED target pattern is an important step for the future also with respect to studies of the target pattern in divertor tokamaks.

Chapter 7

Summary

Resonant magnetic perturbations (RMPs) are a possible way to control transport in the edge of magnetically confined fusion plasmas. In particular, they have shown the potential to mitigate or suppress Edge Localized Modes (ELMs), which can lead to unacceptably large transient heat fluxes to the plasma facing components.

In the frame of this work the impact of fast rotating Resonant Magnetic Perturbation fields provided by the Dynamic Ergodic Divertor (DED) on plasma edge parameters at the TEXTOR tokamak was studied experimentally. The aim of this investigations was a detailed characterization of the RMP imposed 3D plasma structure for fast rotating RMP fields by means of electron density and temperature profile measurements.

To meet this a goal, a resistive edge plasma (edge electron collisionality $\nu_e^* > 4$) in low confinement mode (L-mode) is studied at TEXTOR with a set of three diagnostics:
(1) The gas puff imaging technique is utilized to resolve the local variations of the hydrogenic Balmer-alpha emission within a hydrogen gas puff with a high temporal resolution of $20\,\mu$s. It was shown that this method can be used for measuring local electron density variations for plasma edge electron temperatures of $T_e > 40\,\mathrm{eV}$ as achieved in the plasmas under consideration. The diagnostic was designed in the frame of this work and used to measure for the first time the impact of rotating RMP fields at TEXTOR with radial, poloidal and temporal resolution.
(2) Electron density and temperature measurements were performed with a *S*upersonic *He*lium beam (SHE) diagnostic based on beam emission spectroscopy on thermal helium. This diagnostic was improved in the frame of this work toward a reliable standard diagnostic at TEXTOR with high spatial and temporal resolution. A new nozzle-skimmer combination was designed in order to create a neutral helium beam with low divergence of $\sphericalangle \pm 1.6^\circ$ and high neutral particle density of $n_0 = 1.0 \cdot 10^{18}\,\mathrm{m}^{-3}$ on axis at the same time. With the improved setup, the helium beam flux was increased by 85% to $q_{He} = 3.2 \cdot 10^{17}\,\mathrm{s}^{-1}$. The high beam flux in combination with a highly efficient multi-anode photomultiplier system enables to determine electron density n_e

and temperature T_e simultaneously with a high temporal resolution of $20\,\mu$s and a radial resolution of $\Delta r = 2\,$mm. It was shown that a static collisional radiative model can be applied to dynamic processes in order to deduce the density and temperature variations from the helium emission profiles. The time resolution of the optimized setup presented is finally limited by the pumping efficiency of the SHE, which prevents higher helium to be injected and therefore higher photon fluxes to the detector.
(3) A set of five single Langmuir probes was used to determine the local ion flux to the probe as a function of time with a high temporal resolution of $20\,\mu$s. They are mounted into the DED target in front of the DED coils and are distributed around the torus. This set of Langmuir probes enable to characterize the rotating plasma structure on the DED target in the toroidal direction and in the rotation direction of the DED field.

The setup presented allows the characterization of the local plasma parameter distribution, i.e. plasma structure, imposed by fast rotating 3D RMP fields. It was shown by gas puff imaging (GPI) techniques that rotating RMP fields impose a characteristic plasma structure to the edge similar to the one observed with static RMP fields, which rotates locked to the external RMP frequency of $|\nu_{RMP}| = 1\,$kHz in the RMP rotation direction. The data show that the rotating plasma structure imposes a modulation to the electron density at a fixed poloidal position. It was shown that the plasma structure is characterized by the modulation depth and a phase shift of the modulation and the spatial variation of these quantities. Both change along the radial direction which gives first experimental evidence that the underlying rotating 3D magnetic topology consists of domains with different transport properties.
Utilizing the SHE diagnostic, a modulation of both n_e and T_e fields coherent with the rotation frequency of the externally applied RMP field was measured. The modulation proves consistently with GPI measurements that a perturbed magnetic boundary layer is imposed with fast RMP rotations in general.

In order to compare results for fast rotating RMP fields to those obtained with static RMP fields, a low relative rotation between rotating RMP field and plasma fluid rotation of $f_{rel} = -200\,Hz$ was chosen. In the far plasma edge at a normalized minor radius of $r/a > 0.98$ with a as the radial position of the last closed flux surface, substantial experimental evidence was found that the three-dimensional scrape-off layer found with static RMP fields is preserved for fast RMP field rotation. Therefore, electron density and temperature modulations were compared to the modeled magnetic topology in vacuum approximation, i.e. without internal plasma response. The modulation in both n_e and T_e shows that an alternating layer with different local transport properties exists: A strong reduction in both plasma parameters is found to be correlated with regions within the 3D SOL, where coherent field lines bundled to so-called laminar flux tubes connect the measurement position to the wall on short distances. The reduction in n_e, T_e and therefore electron pressure p_e shows in agreement with measurements in the presence of static RMP fields that the laminar flux tubes are dominated by a strong parallel transport and represent an effective exhaust channel for both particles and energy. In contrast, regions within the 3D SOL with long, stochastically distributed field

lines leave the electron density and temperature unchanged. The spatial dimensions of the $p_e(r,t)$ drop and therefore of the laminar flux tubes were shown to be correlated to the modeled magnetic topology in vacuum approximation. For high DED amplitudes the pressure drop inside the helical flux tube is limited either by an effectively enhanced radial transport or by an increased particle recycling fueling the flux tubes.

At the radially inward, next rational flux surface, the electron density waveform appears to be phase shifted with respect to the temperature waveform, which gives first experimental evidence that the underlying magnetic topology changes in the radial direction.
In order to study a potential dependence of the plasma structure on the relative rotation between the external RMP field and the intrinsic plasma fluid rotation, the external RMP field rotation direction was changed without changing the global plasma parameters. This yields a low and high relative rotation case with $f_{rel} = -200\,\mathrm{Hz}$ and $f_{rel} = 1800\,\mathrm{Hz}$, respectively.
For a *low relative rotation*, the phase shift between density and temperature is small ($\phi < 100°$), which shows that a dominant pressure drop is still present and indicates a dominant loss of both particles and energy. This experimental observation is in fair agreement with the modeled underlying magnetic topology in vacuum approximation, which suggests at the position of the rational flux surface a domain with field lines connecting the measurement position to the wall on short distances and therefore a dominant particle and energy loss. For a *high relative rotation*, it was shown that at the rational flux surface the density waveform is delayed to the temperature waveform by 180°. It means that an increase in density occurs in coincidence to a decrease in temperature and vice versa. This experimental observation shows for the first time that the edge plasma structure exhibits a dependence on the relative rotation. A comparison of the local modulation properties and the radial density and temperature profiles with the 3D plasma kinetic fluid and transport code EMC3-EIRENE indicates that for high relative rotation the measured plasma structure can be interpreted as the formation of a magnetic island at the rational flux surface. This island represents a confining sub-volume which connects radially separated regions with fast particle and energy transport around the so-called O-point of the island. An additional detailed analysis of the experimental profile reactions in comparison with the modeled ones confirms qualitatively that a magnetic island is formed only for high relative rotation. As modeling in vacuum approximation predicts a domain with field lines connecting on short distances to the wall, the experimental data point to a local damping of the resonant amplitude resulting in an intact island structure.
It was shown that the characteristic density and temperature waveforms indicating a local magnetic island are found for high relative rotation at any perturbation strength as is expected in vacuum approximation for a damped perturbation strength. For low relative rotation, the phase delay between n_e and T_e vanishes with increasing RMP field strength, which indicates that the magnetic island is replaced by a Laminar Zone with connecting field lines to the wall.
A comparison of the modulation with the vacuum topology clearly demonstrates that the O-point and X-point of the island are shifted by $\pi/2$ in the direction of the toroidal

magnetic field. This behavior confirms qualitatively the results of a 4-field fluid-drift model including internal plasma response. Here, a shifted magnetic topology is present due to screening currents on the rational flux surface. The basic modeling results can potentially explain the experimental observations. This provides evidence that at high relative rotation a magnetic island exists which is phase shifted to the external vacuum field. The island replaces the Laminar Zone at high rotation leading to the conclusion that screening with shifted magnetic island structures instead of a Laminar Zone occurs at (a) high rotation at any perturbation strength and (b) low rotation at low RMP field strength.

Radially outward at the position of the Laminar Zone, a shift of the entire density and temperature modulations is detected in correlation with the shifted plasma structure at the next radially inward rational flux surface. This shows for the first time that a direct connection between the structure at the rational flux surface and the position of the outward Laminar Zone exists. The rotation dependent shift of the plasma structure far away from the RMP coils support the existence of a rotation dependent shift directly in front of the RMP coils, i.e. the magnetic near field of the DED. Therefore, the ion flux was measured with a set of Langmuir probes to quantify the rotating plasma structure in the near field of the RMP coils. A modulation was found to exist which corresponds to the local magnetic topology directly in front of the RMP coils. The measured waveform matches the one calculated in vacuum approximation for low relative rotation only. For high relative rotation the measured modulation appears to be shifted according to the shift at the outermost rational flux surface. However, the shift of the target pattern appears to be less than at the rational flux surface, which gives substantial experimental evidence that a competition exists between the vacuum-like unshifted topology and the shifted magnetic topology at the outermost rational flux surface. Independently of the rotation, the helical symmetry given by the setup was shown to be preserved.

These new results obtained for highly resistive edge plasmas show that the basic topological domains found for static RMP fields are preserved with fast rotating RMP fields. However, the results also prove that the formation of the edge plasma structure depends on the relative rotation between the external RMP field and the plasma fluid which suggests a rotation dependent plasma response of the underlying magnetic topology. It was shown that a direct connection exists between the plasma structure at the rational flux surface and the outermost regions close to the target in front of the RMP coils.

In general, the results obtained manifest that any modeling of the edge plasma structure in the presence of 3D magnetic perturbations has to account for internal plasma response in general, e.g. as prescribed in the four-field model used in the frame of this work. In particular, for modeling of the externally imposed 3D plasma structure for the next step fusion experiment ITER, the internal plasma response as a function of the plasma parameters is of major importance. In ITER, the actual rotation level and the dominant driving terms are not yet entirely known. However, in the foreseen scenario of improved high confinement ("H-mode"), already the steep edge pressure gradients are capable to generate a diamagnetic plasma response to the external perturbation fields. Both,

pressure profile and rotation measurements are captured by the experimental results presented. Here, in particular the rotation of the perturbation field facilitated the measurement of important quantities needed to benchmark plasma response models with a profile diagnostic. In particular, the spatial extension of the structures in terms of electron density and temperature, the phase between them and the phase shift of the structures with respect to the vacuum-like magnetic topology could be determined with an accuracy better than any measurement before. This set of parameters are used at present as key ingredients for basic benchmarking of modeling codes including plasma response in the limit of high resistivity in order to extrapolate to the operational parameter space of ITER with low resistivity plasmas.

The results motivate future studies of the perturbed 3D magnetic topology by measuring directly the local magnetic field, as has been already started in TEXTOR. Since such measurements will be very difficult in divertor tokamaks with H-mode and much smaller distances between the rational flux surfaces, it is proposed – based on the experimental results presented here – to observe the divertor strike line pattern with static and rotating RMP fields in order to conclude from these on the magnetic topology radially inward. Such an approach is currently applied on all devices investigating external resonant magnetic perturbation fields [101, 107, 108]. Upcoming experiments on the ASDEX-Upgrade tokamak [109] with the capability to apply both rotating and static RMP fields will extend these studies. Comparing the basic results from TEXTOR with this variety of plasma shapes and operational regimes will contribute to the understanding of the formation of a 3D plasma boundary and the plasma transport.

Bibliography

[1] Heinloth, K. Die Energiefrage. Vieweg Verlag, zweite Auflage (2003).

[2] Rebhan, E. et. al. Energy Technologies: Nuclear Energy. Springer Verlag GmbH (2003).

[3] Wesson, J. Tokamaks. Clarendon Press, Oxford, third edition (2004).

[4] Samm, U. *Contemporary Physics Of Plasmas*, **44, number 3** (2003), 203–217.

[5] Keilhacker, M. *Fusion Engineering and Design*, **46** (1999), 2-4, 273 – 290.

[6] Wagner, F. et al. *Physical Review Letters*, **49** (1982), 19, 1408–1412.

[7] Zohm, H. et al. *Nuclear Fusion*, **35** (1995), 5, 543.

[8] Federici, G. et al. *Journal of Nuclear Materials*, **313-316** (2003), 11 – 22. Plasma-Surface Interactions in Controlled Fusion Devices 15.

[9] Evans, T. E. et al. *Nature of Physics*, **2** (2006), 6, 419–423.

[10] DIII-D Team, Simonen, T. C. *Fusion Engineering and Design*, **39-40** (1998), 83–90.

[11] Lyman Spitzer, J. *Physics of Fluids*, **1** (1958), 4, 253–264.

[12] Burrell, K. H. et al. *Plasma Physics and Controlled Fusion*, **34** (1992), 13, 1859.

[13] Asakura, N., et al. *Nippon Genshiryoku Kenkyujo JAERI,Review*, **L2149A** (2003), 327–337.

[14] Federici, G.; Loarte, A. and Strohmayer, G. *Plasma Physics and Controlled Fusion*, **45** (2003), 9, 1523.

[15] Snyder, P. et al. *Nuclear Fusion*, **44** (2004), 2, 320.

[16] Schmitz, O. et al. *Phys. Rev. Letters*, **103** (2009), 165005.

[17] Neubauer, O. et al. *Fus. Science and Techn.*, **47** (2005), 76–86.

[18] Finken, K. H. et al. The structure of magnetic field in the TEXTOR-DED. Forschungszentrum Jülich, Zentralbibliothek, Verlag (2005).

[19] Finken, K.H. et al. *Contrib. Plasma Phys.*, **46, No. 7-9** (2006), 515–526.

[20] Koslowski, H.R. et al. *Plasma Phys. Control. Fusion*, **48** (2006), 12B, B53–B61.

[21] Schmitz, O. et al. *AIP Conference Proceedings*, **993** (2008), 1, 135–142.

[22] Zweben, S. J. et al. *Physics of Plasmas*, **9** (2002), 5, 1981–1989.

[23] Terry, J. et al. *Journal of Nuclear Materials*, **290-293** (2001), 757–762.

[24] Maqueda, R. J. et al. *Review of Scientific Instruments*, **72** (2001), 1, 931–934.

[25] Bozhenkov, S. Analysis of disruptions and their mitigation using ultra-fast observation systems. Ph.D. thesis, Ruhr-Universität Bochum (2007).

[26] Wiese, W. L. and Fuhr, J. R. *Journal of Physical and Chemical Reference Data*, **38** (2009), 3, 565–720.

[27] http://open.adas.ac.uk/.

[28] Hintz, E. and Schweer, B. *Plasma Physics and Controlled Fusion*, **37** (1995), 11A, A87–A101.

[29] Schweer, B.; Brix, M. and Lehnen, M. *Journal of Nuclear Materials*, **266-269** (1999), 673 – 678.

[30] Schmitz, O. et al. *Plasma Phys. Control. Fusion*, **50** (2008), 11, 115004.

[31] Pospieszczyk, A. et al. *Nuclear Instruments and Methods in Physics Research Section B: Beam Interactions with Materials and Atoms*, **72** (1992), 2, 207 – 223.

[32] Andruczyk, D. et al. *Plasma Devices and Operations*, **14** (2006), 1, 81–89.

[33] Diez-Rojo, T. et al. *Review of Scientific Instruments*, **68** (1997), 3, 1423–1428.

[34] Hidalgo, A. et al. *Review of Scientific Instruments*, **75** (2004), 10, 3478–3480.

[35] Brosda, B. Modellierung von Helium-Atomstrahlen und ihr Einsatz zur Plasmadiagnostik der Tokamakrandschicht. Ph.D. thesis, Ruhr-Universität Bochum (1993).

[36] Brix, M. Messung von Elektronentemperatur und -dichte mittels Heliumstrahldiagnostik im Randschichtplasma eines Tokamaks. Ph.D. thesis, Universität Bochum (1998).

[37] Kruezi, U. Entwicklung einer Heliumstrahldiagnostik zur Messung der Elektronendichte und -temperatur mit hoher räumlicher und zeitlicher Auflösung, volume 62. Schriften des Forschungszentrums Jülich . Reihe Energietechnik / Energy Technology (2007).

[38] Fenn, J. and Deckers, J. Molecular Beams from Nozzle Sources. Rarefield Gas Dynamics, Vol. 1, Acadamic Press, New York (1963).

[39] Campargue, R.; Lebehot, A. and Lemmonnier, J. High Intensity Supersonic Molecular Beam Apparatus. Rarefield Gas Dynamics, Vol. 2, Acadamic Press, New York (1966).

[40] Wegener, P. *Yale University, Marcel Dekker Inc., New York*, (1974), 1–58.

[41] Campargue, R. *J. Phys Chem.*, **88** (1984), 4466–4474.

[42] Gentry, W. Low-Energy Pulsed Beam Sources. Atomics and moleacular beam methods, Vol. 1, Oxford University Press, New York (1988).

[43] Fritsche, B. Operating a Skimmer in Continuum Flow. Rarefield Gas Dynamics, 17th, Weinheim (1990).

[44] Morse, M. Supersonic beam sources. Atomic, molecular and optical physics: atoms and molecules, Academic Press, Vol. 29b (1996).

[45] Miller, D. R. Free Jet Sources in Atomic and Molecular beam methods. Oxford University Press, New York (1988).

[46] Stuckenberg, H. J. *CAMAC Bull.*, **13SA** (1975), 1–40.

[47] Bencze, A. and Zoletnik, S. *Physics of Plasmas*, **12** (2005), 5, 052323.

[48] Stangeby, P. The Plasma Boundary of Magnetic Fusion Devices. IoP, Institute of Physics Publishing, Bristol and Philadelphia, ISBN 0 7503 0559 2 (2000).

[49] Endler, M. Experimentelle Untersuchung und Modellierung elektrostatischer Fluktuationen in den Abschälschichten des Tokamak ASDEX und des Stellarators Wendelstein 7-AS. Max-Planck Institut für Plasmaphysik, Garching bei München, IPP III/197 (1994).

[50] Abdullaev, S. S.; Finken, K. H. and Spatschek, K. H. *Physics of Plasmas*, **6** (1999), 1, 153–174.

[51] Abdullaev, S. et al. *Nuclear Fusion*, **43** (2003), 5, 299–313.

[52] Gourdon, C. *CEN, Fontenay aux Roses*, (1970). Programme optimise de calculs numeriques dans les configurations magnetiques toroidales.

[53] Lotz, W. Optimiertes Programm für numerische Rechnungen in toroidalen Magnetfeld-Konfigurationen. Fassung für Benutzer der GOURDON-Programme, die von W. Lotz revidiert wurden. Zweiter Teil: Programmstruktur Gebrauchs-Spezifikationen. Max-Planck-Institut für Plasmaphysik Garching, Diplomarbeit, 1983 (unpublished).

[54] Frerichs, H. Three-dimensional plasma transport in open chaotic magnetic fields: A computational assessment for tokamak edge layers. Berichte des Forschungszentrums Jülich, Jül-4321, ISSN 0944-2952 (2010).

[55] Press, W.h. et al. Numerical Recipes in C, The Art of Scientific Computing. Cambridge University Press, Second Edition (2002).

[56] Haberscheidt, T. MHD-Gleichgewichte im TEXTOR Tokamak. Master's thesis, Heinrich-Heine Universität Düsseldorf (2002).

[57] Feng, Y.; Sardei, F. and Kisslinger, J. *Journal of Nuclear Materials*, **266-269** (1999), 812–818.

[58] D. Reiter, P. B., M. Baelmans. *Fusion Science and Technology*, **47** (2005), 172–186.

[59] Feng, Y. et al. *Nuclear Fusion*, **49** (2009), 9, 095002.

[60] Kobayashi, M. et al. *Nuclear Fusion*, **44** (2004), 6, S64–S73.

[61] Frerichs, H. et al. *Nuclear Fusion*, **50** (2010), 034004.

[62] Braginski, S. I. *Reviews of Plasma Physics, Consultants Bureau, New York*, **1** (1965), 205–311.

[63] Schmitz, O. Experimentelle Untersuchung der Plasmastruktur und Charakterisierung des Transportverhaltens in der laminaren Zone einer stochastisierten Plasmarandschicht. Ph.D. thesis, Heinrich-Heine-Universität Düsseldorf (2006).

[64] Abdullaev, S.S. et al. *Proceedings of the 32th European Physical Society Conference on Controlled Fusion and Plasma Physics*, (2005).

[65] Schmitz, O. et al. *Nuclear Fusion*, **48** (2008), 2, 024009.

[66] Jakubowski, M.W. et al. *Nuclear Fusion*, **44** (2004), 6, S1–S11.

[67] Jakubowski, M.W. et al. *Phys. Rev. Letters*, **96** (2006), 3, 035004.

[68] Wolf, R. C. et al. *Nuclear Fusion*, **45** (2005), 12, 1700–1707.

[69] Miyamoto, K. Plasma Physics for Nuclear Fusion. The MIT Press, ISBN 0-262-13145-5 (1976).

[70] Fitzpatrick, R. The Physics of Plasmas (lecture notes). The University of Texas at Austin.

[71] Wiegmann, Ch. et al. *36th EPS Conference on Plasma Phys. Sofia, June 29 - July 3, 2009 ECA*, **Vol.33E** (2009), P–1.132.

[72] Beyer, P.; Garbet, X. and Ghendrih, P. *Physics of Plasmas*, **5** (1998), 12, 4271–4279.

[73] Beyer, P. et al. *Plasma Physics and Controlled Fusion*, **44** (2002), 10, 2167.

[74] Yu, Q. et al. *Nuclear Fusion*, **48** (2008), 2, 024007.

[75] Kikuchi, Y. et al. *Contributions to Plasma Physics*, **46** (2006), 529–544.

[76] Fitzpatrick, R. *Nuclear Fusion*, **33** (1993), 7, 1049–1084.

[77] Fitzpatrick, R. *Physics Of Plasmas*, **5** (1998), 9, 3325–3341.

[78] Cole, A. and Fitzpatrick, R. *Phys. of Plasmas*, **13** (2006), 3, 032503.

[79] Reiser, D. and Chandra, D. *Phys. of Plasmas*, **16** (2009), 1, 042317.

[80] Reiser, D. and Tokar, M. Z. *Physics of Plasmas*, **16** (2009), 12, 122303.

[81] Reiser, D. and Scott, B. *Physics of Plasmas*, **12** (2005), 12, 122308.

[82] Coenen, J. The Influence of the Dynamic Ergodic Divertor on the Radial Electric Field at the Tokamak TEXTOR. Schriften des Forschungszentrums Jülich, Reihe Energie & Umwelt / Energy & Environment 39, ISSN 1866-1793 (2009).

[83] Stoschus, H. et al. *Journal of Nuclear Materials*, (2010), (In Press, Corrected Proof).

[84] Stoschus, H. et al. *Phys. Plasmas*, **17** (2010), 060702.

[85] Stoschus, H. et al. *Nuclear Fusion*, (2011), (submitted).

[86] Isler, R. C. *Plasma Physics and Controlled Fusion*, **36** (1994), 2, 171.

[87] Domier, C. W. et al. *Review of Scientific Instruments*, **77** (2006), 10, 10E924.

[88] Spakman, G.W. et al. *Nuclear Fusion*, **48** (2008), 11, 115005 (10pp).

[89] Taylor, E. D. et al. *Physics of Plasmas*, **9** (2002), 9, 3938–3945.

[90] Kantor, M. et al. *36th EPS Conference on Plasma Phys. Sofia, June 29 - July 3*, **ECA Vol.33E** (2009), P–1.184.

[91] Clever, M. Hydrogen recycling an transport in the helical divertor of TEXTOR. Forschungszentrum Jülich, Zentralbibliothek, Verlag, ISBN: 978-3-89336-673-6 (2010).

[92] Schmitz, O. et al. *J. of Nucl. Mat.*, **390-391** (2009), 330–334.

[93] De Bock, M. et al. *Nuclear Fusion*, **48** (2008), 015007.

[94] Unterberg, B. et al. *J. of Nucl. Mat.*, **363** (2007), 698–702.

[95] Nardon, E. et al. *Phys. of Plasmas*, **14** (2007), 092501.

[96] Leconte, M. *Phys. Rev. Letters*, **102** (2009), 045006.

[97] Loozen, X. Modeling of Plasma Response to Magnetic Field Perturbations from the Dynamic Ergodic Divertor (DED) and Comparison with Experiments. Berichte des Forschungszentrums Jülich, Jül-4251, ISSN 0944-2952 (2006).

[98] Hölzl, M. et al. *Physics of Plasmas*, **14** (2007), 5, 052501.

[99] Tokar, M. Z. et al. *Physics of Plasmas*, **15** (2008), 7, 072515.

[100] Schmitz, O. et al. *Plasma Physics and Controlled Fusion*, **50** (2008), 12, 124029.

[101] Nardon, E. et al. *Journal of Nuclear Materials*, (2010), (In Press, Corrected Proof).

[102] Lehnen, M. et al. *Plasma Fusion*, **3** (2008), S1039.

[103] Giesen, B. et al. *Fusion Engineering and Design*, **66-68** (2003), 419–423.

[104] Wingen, A. et al. *Physics of Plasmas*, **14** (2007), 042502.

[105] Jakubowski, M. et al. *Journal Of Nuclear Materials*, **363-365** (2007), 371–376.

[106] Sakamoto, M. et al. Dynamic behavior of rotating magnetic field perturbation induced by the dynamic ergodic divertor in the textor tokamak (2007). Workshop on Stochasticity in Fusion Plasmas, http://www.fz-juelich.de/sfp/.

[107] Schmitz, O. et al. *Journal of Nuclear Materials*, (2011), (In Press, Accepted Manuscript).

[108] Ahn, J.-W. et al. *Journal of Nuclear Materials*, (2011), (In Press, Accepted Manuscript).

[109] Suttrop, W. et al. *Fusion Engineering and Design*, **84** (2009), 2-6, 290–294.

List of Figures

Acknowledgements

Finally, I would like to express my deepest gratitude to all who contributed to the success of this work:

First of all, Prof. U. Samm for the interesting and challenging topic and the opportunity to work on it in a remarkable environment. The steady support by asking the right questions improved my understanding and motivated me a lot. I would like to extend my thanks to Prof. G. Pretzler for taking over the co-review.

My special thanks and respect I would like to express cordially to Prof. B. Unterberg and Dr. O. Schmitz for their outstanding supervision. They supported me with their experience and the continuous development of ideas in various fruitful discussions, which were the basis for the success of this work.

Thank you to all who read the thesis and for many helpful comments, in particular Philippe Mertens for correcting my orthography.

Without a doubt, I am very grateful for the warm and colleague atmosphere and the numerous inspiring physics related and private discussions with my colleagues and friends: Jan Coenen, Nadine Baumgarten, Meike Clever, Benjamin Berberich, Mikhael Mitri, Marcin Jakubowski, Christian Schulz, Maria Matveeva, Dmitri Matveev, Heinke Frerichs, Florian Irrek, Niels Gierse, Miroslav Zlobinski, Simon Freutel and Sören Möller. I would like to extend my thanks to the entire PSI group: D. Borodin, S. Brezinsek, A. Kirschner, A. Kreter, M. Lehnen, A. Litnovsky, P. Mertens, V. Philipps and A. Pospieszczyk. For their advices and patient support regarding the diagnostic and therefore technical part, I am very grateful to B. Schweer and U. Kruezi.

The data presented in this thesis would have never been obtained without the entire TEXTOR team, in particular the colleagues: K. Klören, D. Schüller, K. von Bovert, T. Tietz, I. Lassive, N. Sandri, and H. Reimer. Thank you very much for your support with all technical issues.

For many profound discussion I am grateful to the group of Prof. D. Reiter, in particular D. Reiser and H. Frerichs. Their work were the basis for the modeling results in this thesis and helped me a lot in understanding my measurements.

A special thank you I would like to express to the RMP and ELM suppression groups at DIII-D for the colleague atmosphere, especially to T.E. Evans for his support during my research stays.

My deepest gratitude is owed again Oliver Schmitz, not only as a colleague: Numerous private discussion even in busy times or around the whole world helped me to get what I would not have got without probably.

I would like continue in german with thanks to the most important person in my life, my wife: *Nicole, Ich danke Dir für Deinen Rückhalt und Deine Geduld. Du hast mich immer bekräftigt und warst einfach immer für mich da. Ich bin froh, dass es dich gibt!*

Erklärung:
Die hier vorgelegte Dissertation habe ich eigenhändig und ohne unerlaubte Hilfe angefertigt. Die Dissertation wurde in der vorgelegten oder in ähnlicher Form noch bei keiner anderen Institution eingereicht. Ich habe bisher keine erfolglosen Promotionsversuche unternommen.

Düsseldorf, den 28.02.2011

Henning Stoschus

Schriften des Forschungszentrums Jülich
Reihe Energie & Umwelt / Energy & Environment

1. **Einsatz von multispektralen Satellitenbilddaten in der Wasserhaushalts- und Stoffstrommodellierung – dargestellt am Beispiel des Rureinzugsgebietes**
   von C. Montzka (2008), XX, 238 Seiten
   ISBN: 978-3-89336-508-1

2. **Ozone Production in the Atmosphere Simulation Chamber SAPHIR**
   by C. A. Richter (2008), XIV, 147 pages
   ISBN: 978-3-89336-513-5

3. **Entwicklung neuer Schutz- und Kontaktierungsschichten für Hochtemperatur-Brennstoffzellen**
   von T. Kiefer (2008), 138 Seiten
   ISBN: 978-3-89336-514-2

4. **Optimierung der Reflektivität keramischer Wärmedämmschichten aus Yttrium-teilstabilisiertem Zirkoniumdioxid für den Einsatz auf metallischen Komponenten in Gasturbinen**
   von A. Stuke (2008), X, 201 Seiten
   ISBN: 978-3-89336-515-9

5. **Lichtstreuende Oberflächen, Schichten und Schichtsysteme zur Verbesserung der Lichteinkopplung in Silizium-Dünnschichtsolarzellen**
   von M. Berginski (2008), XV, 171 Seiten
   ISBN: 978-3-89336-516-6

6. **Politikszenarien für den Klimaschutz IV – Szenarien bis 2030**
   hrsg.von P. Markewitz, F. Chr. Matthes (2008), 376 Seiten
   ISBN 978-3-89336-518-0

7. **Untersuchungen zum Verschmutzungsverhalten rheinischer Braunkohlen in Kohledampferzeugern**
   von A. Schlüter (2008), 164 Seiten
   ISBN 978-3-89336-524-1

8. **Inorganic Microporous Membranes for Gas Separation in Fossil Fuel Power Plants**
   by G. van der Donk (2008), VI, 120 pages
   ISBN: 978-3-89336-525-8

9. **Sinterung von Zirkoniumdioxid-Elektrolyten im Mehrlagenverbund der oxidkeramischen Brennstoffzelle (SOFC)**
   von R. Mücke (2008), VI, 165 Seiten
   ISBN: 978-3-89336-529-6

10. **Safety Considerations on Liquid Hydrogen**
    by K. Verfondern (2008), VIII, 167 pages
    ISBN: 978-3-89336-530-2

11. **Kerosinreformierung für Luftfahrtanwendungen**
von R. C. Samsun (2008), VII, 218 Seiten
ISBN: 978-3-89336-531-9

12. **Der 4. Deutsche Wasserstoff Congress 2008 – Tagungsband**
hrsg. von D. Stolten, B. Emonts, Th. Grube (2008), 269 Seiten
ISBN: 978-3-89336-533-3

13. **Organic matter in Late Devonian sediments as an indicator for environmental changes**
by M. Kloppisch (2008), XII, 188 pages
ISBN: 978-3-89336-534-0

14. **Entschwefelung von Mitteldestillaten für die Anwendung in mobilen Brennstoffzellen-Systemen**
von J. Latz (2008), XII, 215 Seiten
ISBN: 978-3-89336-535-7

15. **RED-IMPACT**
Impact of Partitioning, Transmutation and Waste Reduction Technologies on the Final Nuclear Waste Disposal
SYNTHESIS REPORT
ed. by W. von Lensa, R. Nabbi, M. Rossbach (2008), 178 pages
ISBN 978-3-89336-538-8

16. **Ferritic Steel Interconnectors and their Interactions with Ni Base Anodes in Solid Oxide Fuel Cells (SOFC)**
by J. H. Froitzheim (2008), 169 pages
ISBN: 978-3-89336-540-1

17. **Integrated Modelling of Nutrients in Selected River Basins of Turkey**
Results of a bilateral German-Turkish Research Project
project coord. M. Karpuzcu, F. Wendland (2008), XVI, 183 pages
ISBN: 978-3-89336-541-8

18. **Isotopengeochemische Studien zur klimatischen Ausprägung der Jüngeren Dryas in terrestrischen Archiven Eurasiens**
von J. Parplies (2008), XI, 155 Seiten, Anh.
ISBN: 978-3-89336-542-5

19. **Untersuchungen zur Klimavariabilität auf dem Tibetischen Plateau - Ein Beitrag auf der Basis stabiler Kohlenstoff- und Sauerstoffisotope in Jahrringen von Bäumen waldgrenznaher Standorte**
von J. Griessinger (2008), XIII, 172 Seiten
ISBN: 978-3-89336-544-9

20. **Neutron-Irradiation + Helium Hardening & Embrittlement Modeling of 9%Cr-Steels in an Engineering Perspective (HELENA)**
by R. Chaouadi (2008), VIII, 139 pages
ISBN: 978-3-89336-545-6

21. **in Bearbeitung**

22. **Verbundvorhaben APAWAGS (AOEV und Wassergenerierung) – Teilprojekt: Brennstoffreformierung – Schlussbericht**
von R. Peters, R. C. Samsun, J. Pasel, Z. Porš, D. Stolten (2008), VI, 106 Seiten
ISBN: 978-3-89336-547-0

23. **FREEVAL**
Evaluation of a Fire Radiative Power Product derived from Meteosat 8/9 and Identification of Operational User Needs
Final Report
project coord. M. Schultz, M. Wooster (2008), 139 pages
ISBN: 978-3-89336-549-4

24. **Untersuchungen zum Alkaliverhalten unter Oxycoal-Bedingungen**
von C. Weber (2008), VII, 143, XII Seiten
ISBN: 978-3-89336-551-7

25. **Grundlegende Untersuchungen zur Freisetzung von Spurstoffen, Heißgaschemie, Korrosionsbeständigkeit keramischer Werkstoffe und Alkalirückhaltung in der Druckkohlenstaubfeuerung**
von M. Müller (2008), 207 Seiten
ISBN: 978-3-89336-552-4

26. **Analytik von ozoninduzierten phenolischen Sekundärmetaboliten in *Nicotiana tabacum* L. cv Bel W3 mittels LC-MS**
von I. Koch (2008), III, V, 153 Seiten
ISBN 978-3-89336-553-1

27. **IEF-3 Report 2009. Grundlagenforschung für die Anwendung**
(2009), ca. 230 Seiten
ISBN: 978-3-89336-554-8

28. **Influence of Composition and Processing in the Oxidation Behavior of MCrAlY-Coatings for TBC Applications**
by J. Toscano (2009), 168 pages
ISBN: 978-3-89336-556-2

29. **Modellgestützte Analyse signifikanter Phosphorbelastungen in hessischen Oberflächengewässern aus diffusen und punktuellen Quellen**
von B. Tetzlaff (2009), 149 Seiten
ISBN: 978-3-89336-557-9

30. **Nickelreaktivlot / Oxidkeramik – Fügungen als elektrisch isolierende Dichtungskonzepte für Hochtemperatur-Brennstoffzellen-Stacks**
von S. Zügner (2009), 136 Seiten
ISBN: 978-3-89336-558-6

31. **Langzeitbeobachtung der Dosisbelastung der Bevölkerung in radioaktiv kontaminierten Gebieten Weißrusslands – Korma-Studie**
von H. Dederichs, J. Pillath, B. Heuel-Fabianek, P. Hill, R. Lennartz (2009), Getr. Pag.
ISBN: 978-3-89336-532-3

32. **Herstellung von Hochtemperatur-Brennstoffzellen über physikalische Gasphasenabscheidung**
von N. Jordán Escalona (2009), 148 Seiten
ISBN: 978-3-89336-532-3

33. **Real-time Digital Control of Plasma Position and Shape on the TEXTOR Tokamak**
by M. Mitri (2009), IV, 128 pages
ISBN: 978-3-89336-567-8

34. **Freisetzung und Einbindung von Alkalimetallverbindungen in kohlebefeuerten Kombikraftwerken**
von M. Müller (2009), 155 Seiten
ISBN: 978-3-89336-568-5

35. **Kosten von Brennstoffzellensystemen auf Massenbasis in Abhängigkeit von der Absatzmenge**
von J. Werhahn (2009), 242 Seiten
ISBN: 978-3-89336-569-2

36. **Einfluss von Reoxidationszyklen auf die Betriebsfestigkeit von anodengestützten Festoxid-Brennstoffzellen**
von M. Ettler (2009), 138 Seiten
ISBN: 978-3-89336-570-8

37. **Großflächige Plasmaabscheidung von mikrokristallinem Silizium für mikromorphe Dünnschichtsolarmodule**
von T. Kilper (2009), XVII, 154 Seiten
ISBN: 978-3-89336-572-2

38. **Generalized detailed balance theory of solar cells**
by T. Kirchartz (2009), IV, 198 pages
ISBN: 978-3-89336-573-9

39. **The Influence of the Dynamic Ergodic Divertor on the Radial Electric Field at the Tokamak TEXTOR**
von J. W. Coenen (2009), xii, 122, XXVI pages
ISBN: 978-3-89336-574-6

40. **Sicherheitstechnik im Wandel Nuklearer Systeme**
von K. Nünighoff (2009), viii, 215 Seiten
ISBN: 978-3-89336-578-4

41. **Pulvermetallurgie hochporöser NiTi-Legierungen für Implanat- und Dämpfungsanwendungen**
von M. Köhl (2009), XVII, 199 Seiten
ISBN: 978-3-89336-580-7

42. **Einfluss der Bondcoatzusammensetzung und Herstellungsparameter auf die Lebensdauer von Wärmedämmschichten bei zyklischer Temperaturbelastung**
von M. Subanovic (2009), 188, VI Seiten
ISBN: 978-3-89336-582-1

43. **Oxygen Permeation and Thermo-Chemical Stability of Oxygen Permeation Membrane Materials for the Oxyfuel Process**
by A. J. Ellett (2009), 176 pages
ISBN: 978-3-89336-581-4

44. **Korrosion von polykristallinem Aluminiumoxid (PCA) durch Metalljodidschmelzen sowie deren Benetzungseigenschaften**
von S. C. Fischer (2009), 148 Seiten
ISBN: 978-3-89336-584-5

45. **IEF-3 Report 2009. Basic Research for Applications**
(2009), 217 Seiten
ISBN: 978-3-89336-585-2

46. **Verbundvorhaben ELBASYS (Elektrische Basissysteme in einem CFK-Rumpf) - Teilprojekt: Brennstoffzellenabgase zur Tankinertisierung - Schlussbericht**
von R. Peters, J. Latz, J. Pasel, R. C. Samsun, D. Stolten
(2009), xi, 202 Seiten
ISBN: 978-3-89336-587-6

47. **Aging of ^{14}C-labeled Atrazine Residues in Soil: Location, Characterization and Biological Accessibility**
by N. D. Jablonowski (2009), IX, 104 pages
ISBN: 978-3-89336-588-3

48. **Entwicklung eines energetischen Sanierungsmodells für den europäischen Wohngebäudesektor unter dem Aspekt der Erstellung von Szenarien für Energie- und CO_2 - Einsparpotenziale bis 2030**
von P. Hansen (2009), XXII, 281 Seiten
ISBN: 978-3-89336-590-6

49. **Reduktion der Chromfreisetzung aus metallischen Interkonnektoren für Hochtemperaturbrennstofzellen durch Schutzschichtsysteme**
von R. Trebbels (2009), iii, 135 Seiten
ISBN: 978-3-89336-591-3

50. **Bruchmechanische Untersuchung von Metall / Keramik-Verbundsystemen für die Anwendung in der Hochtemperaturbrennstoffzelle**
von B. Kuhn (2009), 118 Seiten
ISBN: 978-3-89336-592-0

51. **Wasserstoff-Emissionen und ihre Auswirkungen auf den arktischen Ozonverlust**
Risikoanalyse einer globalen Wasserstoffwirtschaft
von T. Feck (2009), 180 Seiten
ISBN: 978-3-89336-593-7

52. **Development of a new Online Method for Compound Specific Measurements of Organic Aerosols**
by T. Hohaus (2009), 156 pages
ISBN: 978-3-89336-596-8

53. **Entwicklung einer FPGA basierten Ansteuerungselektronik für Justageeinheiten im Michelson Interferometer**
von H. Nöldgen (2009), 121 Seiten
ISBN: 978-3-89336-599-9

54. **Observation – and model – based study of the extratropical UT/LS**
by A. Kunz (2010), xii, 120, xii pages
ISBN: 978-3-89336-603-3

55. **Herstellung polykristalliner Szintillatoren für die Positronen-Emissions-Tomographie (PET)**
von S. K. Karim (2010), VIII, 154 Seiten
ISBN: 978-3-89336-610-1

56. **Kombination eines Gebäudekondensators mit H2-Rekombinatorelementen in Leichwasserreaktoren**
von S. Kelm (2010), vii, 119 Seiten
ISBN: 978-3-89336-611-8

57. **Plant Leaf Motion Estimation Using A 5D Affine Optical Flow Model**
by T. Schuchert (2010), X, 143 pages
ISBN: 978-3-89336-613-2

58. **Tracer-tracer relations as a tool for research on polar ozone loss**
by R. Müller (2010), 116 pages
ISBN: 978-3-89336-614-9

59. **Sorption of polycyclic aromatic hydrocarbon (PAH) to Yangtze River sediments and their components**
by J. Zhang (2010), X, 109 pages
ISBN: 978-3-89336-616-3

60. **Weltweite Innovationen bei der Entwicklung von CCS-Technologien und Möglichkeiten der Nutzung und des Recyclings von CO_2**
Studie im Auftrag des BMWi
von W. Kuckshinrichs et al. (2010), X, 139 Seiten
ISBN: 978-3-89336-617-0

61. **Herstellung und Charakterisierung von sauerstoffionenleitenden Dünnschichtmembranstrukturen**
von M. Betz (2010), XII, 112 Seiten
ISBN: 978-3-89336-618-7

62. **Politikszenarien für den Klimaschutz V – auf dem Weg zum Strukturwandel, Treibhausgas-Emissionsszenarien bis zum Jahr 2030**
hrsg. von P. Hansen, F. Chr. Matthes (2010), 276 Seiten
ISBN: 978-3-89336-619-4

63. **Charakterisierung Biogener Sekundärer Organischer Aerosole mit Statistischen Methoden**
von C. Spindler (2010), iv, 163 Seiten
ISBN: 978-3-89336-622-4

64. **Stabile Algorithmen für die Magnetotomographie an Brennstoffzellen**
von M. Wannert (2010), ix, 119 Seiten
ISBN: 978-3-89336-623-1

65. **Sauerstofftransport und Degradationsverhalten von Hochtemperaturmembranen für CO2-freie Kraftwerke**
von D. Schlehuber (2010), VII, 139 Seiten
ISBN: 978-3-89336-630-9

66. **Entwicklung und Herstellung von foliengegossenen, anodengestützten Festoxidbrennstoffzellen**
von W. Schafbauer (2010), VI, 164 Seiten
ISBN: 978-3-89336-631-6

67. **Disposal strategy of proton irradiated mercury from high power spallation sources**
by S. Chiriki (2010), xiv, 124 pages
ISBN: 978-3-89336-632-3

68. **Oxides with polyatomic anions considered as new electrolyte materials for solid oxide fuel cells (SOFCs)**
by O. H. Bin Hassan (2010), vii, 121 pages
ISBN: 978-3-89336-633-0

69. **Von der Komponente zum Stack: Entwicklung und Auslegung von HT-PEFC-Stacks der 5 kW-Klasse**
von A. Bendzulla (2010), IX, 203 Seiten
ISBN: 978-3-89336-634-7

70. **Satellitengestützte Schwerewellenmessungen in der Atmosphäre und Perspektiven einer zukünftigen ESA Mission (PREMIER)**
von S. Höfer (2010), 81 Seiten
ISBN: 978-3-89336-637-8

71. **Untersuchungen der Verhältnisse stabiler Kohlenstoffisotope in atmosphärisch relevanten VOC in Simulations- und Feldexperimenten**
von H. Spahn (2010), IV, 210 Seiten
ISBN: 978-3-89336-638-5

72. **Entwicklung und Charakterisierung eines metallischen Substrats für nanostrukturierte keramische Gastrennmembranen**
von K. Brands (2010), vii, 137 Seiten
ISBN: 978-3-89336-640-8

73. **Hybridisierung und Regelung eines mobilen Direktmethanol-Brennstoffzellen-Systems**
von J. Chr. Wilhelm (2010), 220 Seiten
ISBN: 978-3-89336-642-2

74. **Charakterisierung perowskitischer Hochtemperaturmembranen zur Sauerstoffbereitstellung für fossil gefeuerte Kraftwerksprozesse**
von S.A. Möbius (2010) III, 208 Seiten
ISBN: 978-3-89336-643-9

75. **Characterization of natural porous media by NMR and MRI techniques: High and low magnetic field studies for estimation of hydraulic properties**
by L.-R. Stingaciu (2010), 96 pages
ISBN: 978-3-89336-645-3

76. **Hydrological Characterization of a Forest Soil Using Electrical Resistivity Tomography**
by Chr. Oberdörster (2010), XXI, 151 pages
ISBN: 978-3-89336-647-7

77. **Ableitung von atomarem Sauerstoff und Wasserstoff aus Satellitendaten und deren Abhängigkeit vom solaren Zyklus**
von C. Lehmann (2010), 127 Seiten
ISBN: 978-3-89336-649-1

78. **18th World Hydrogen Energy Conference 2010 – WHEC2010 Proceedings**
Speeches and Plenary Talks
ed. by D. Stolten, B. Emonts (2010)
ISBN: 978-3-89336-658-3

78-1. **18th World Hydrogen Energy Conference 2010 – WHEC2010 Proceedings**
Parallel Sessions Book 1:
Fuel Cell Basics / Fuel Infrastructures
ed. by D. Stolten, T. Grube (2010), ca. 460 pages
ISBN: 978-3-89336-651-4

78-2. **18th World Hydrogen Energy Conference 2010 – WHEC2010 Proceedings**
Parallel Sessions Book 2:
Hydrogen Production Technologies – Part 1
ed. by D. Stolten, T. Grube (2010), ca. 400 pages
ISBN: 978-3-89336-652-1

78-3. **18th World Hydrogen Energy Conference 2010 – WHEC2010 Proceedings**
Parallel Sessions Book 3:
Hydrogen Production Technologies – Part 2
ed. by D. Stolten, T. Grube (2010), ca. 640 pages
ISBN: 978-3-89336-653-8

78-4. **18th World Hydrogen Energy Conference 2010 – WHEC2010 Proceedings**
Parallel Sessions Book 4:
Storage Systems / Policy Perspectives, Initiatives and Cooperations
ed. by D. Stolten, T. Grube (2010), ca. 500 pages
ISBN: 978-3-89336-654-5

78-5. **18th World Hydrogen Energy Conference 2010 – WHEC2010 Proceedings**
Parallel Sessions Book 5:
Stategic Analysis / Safety Issues / Existing and Emerging Markets
ed. by D. Stolten, T. Grube (2010), ca. 530 pages
ISBN: 978-3-89336-655-2

78-6. **18th World Hydrogen Energy Conference 2010 – WHEC2010 Proceedings**
Parallel Sessions Book 6:
Stationary Applications / Transportation Applications
ed. by D. Stolten, T. Grube (2010), ca. 330 pages
ISBN: 978-3-89336-656-9

78 Set (complete book series)

18th World Hydrogen Energy Conference 2010 – WHEC2010 Proceedings
ed. by D. Stolten, T. Grube, B. Emonts (2010)
ISBN: 978-3-89336-657-6

79. **Ultrafast voltex core dynamics investigated by finite-element micromagnetic simulations**
by S. Gliga (2010), vi, 144 pages
ISBN: 978-3-89336-660-6

80. **Herstellung und Charakterisierung von keramik- und metallgestützten Membranschichten für die CO_2-Abtrennung in fossilen Kraftwerken**
von F. Hauler (2010), XVIII, 178 Seiten
ISBN: 978-3-89336-662-0

81. **Experiments and numerical studies on transport of sulfadiazine in soil columns**
by M. Unold (2010), xvi, 115 pages
ISBN: 978-3-89336-663-7

82. **Prompt-Gamma-Neutronen-Aktivierungs-Analyse zur zerstörungsfreien Charakterisierung radioaktiver Abfälle**
von J.P.H. Kettler (2010), iv, 205 Seiten
ISBN: 978-3-89336-665-1

83. **Transportparameter dünner geträgerter Kathodenschichten der oxidkeramischen Brennstoffzelle**
von C. Wedershoven (2010), vi, 137 Seiten
ISBN: 978-3-89336-666-8

84. **Charakterisierung der Quellverteilung von Feinstaub und Stickoxiden in ländlichem und städtischem Gebiet**
von S. Urban (2010), vi, 211 Seiten
ISBN: 978-3-89336-669-9

85. **Optics of Nanostructured Thin-Film Silicon Solar Cells**
by C. Haase (2010), 150 pages
ISBN: 978-3-89336-671-2

86. **Entwicklung einer Isolationsschicht für einen Leichtbau-SOFC-Stack**
von R. Berhane (2010), X, 162 Seiten
ISBN: 978-3-89336-672-9

87. **Hydrogen recycling and transport in the helical divertor of TEXTOR**
by M. Clever (2010), x, 172 pages
ISBN: 978-3-89336-673-6

88. **Räumlich differenzierte Quantifizierung der N- und P-Einträge in Grundwasser und Oberflächengewässer in Nordrhein-Westfalen unter besonderer Berücksichtigung diffuser landwirtschaftlicher Quellen**
von F. Wendland et. al. (2010), xii, 216 Seiten
ISBN: 978-3-89336-674-3

89. **Oxidationskinetik innovativer Kohlenstoffmaterialien hinsichtlich schwerer Lufteinbruchstörfälle in HTR´s und Graphitentsorgung oder Aufarbeitung**
von B. Schlögl (2010), ix, 117 Seiten
ISBN: 978-3-89336-676-7

90. **Chemische Heißgasreinigung bei Biomassenvergasungsprozessen**
von M. Stemmler (2010), xv, 196 Seiten
ISBN: 978-3-89336-678-1

91. **Untersuchung und Optimierung der Serienverschaltung von Silizium-Dünnschicht-Solarmodulen**
von S. Haas (2010), ii, 202 Seiten
ISBN: 978-3-89336-680-4

92. **Non-invasive monitoring of water and solute fluxes in a cropped soil**
by S. Garré (2010), xxiv, 133 pages
ISBN: 978-3-89336-681-1

93. **Improved hydrogen sorption kinetics in wet ball milled Mg hydrides**
by L. Meng (2011), II, 119 pages
ISBN: 978-3-89336-687-3

94. **Materials for Advanced Power Engineering 2010**
ed. by J. Lecomte-Beckers, Q. Contrepois, T. Beck and B. Kuhn
(2010), 1327 pages
ISBN: 978-3-89336-685-9

95. **2D cross-hole MMR – Survey design and sensitivity analysis for cross-hole applications of the magnetometric resistivity**
by D. Fielitz (2011), xvi, 123 pages
ISBN: 978-3-89336-689-7

96. **Untersuchungen zur Oberflächenspannung von Kohleschlacken unter Vergasungsbedingungen**
von T. Melchior (2011), xvii, 270 Seiten
ISBN: 978-3-89336-690-3

97. **Secondary Organic Aerosols: Chemical Aging, Hygroscopicity, and Cloud Droplet Activation**
by A. Buchholz (2011), xiv, 134 pages
ISBN: 978-3-89336-691-0

98. **Chrom-bezogene Degradation von Festoxid-Brennstoffzellen**
von A. Neumann (2011), xvi, 218 Seiten
ISBN: 978-3-89336-692-7

99. **Amorphous and microcrystalline silicon applied in very thin tandem solar cells**
by S. Schicho (2011), XII, 190 pages
ISBN: 978-3-89336-693-4

100. **Sol-gel and nano-suspension electrolyte layers for high performance solid oxide fuel cells**
by F. Han (2011), iv, 131 pages
ISBN: 978-3-89336-694-1

101. **Impact of different vertical transport representations on simulating processes in the tropical tropopause layer (TTL)**
by F. Plöger (2011), vi, 104 pages
ISBN: 978-3-89336-695-8

102. **Untersuchung optischer Nanostrukturen für die Photovoltaik mit Nahfeldmikroskopie**
von T. Beckers (2011), xiii, 128 Seiten
ISBN: 978-3-89336-696-5

103. **Impact of contamination on hydrogenated amorphous silicon thin films & solar cells**
by J. Wördenweber (2011), XIV, 138 pages
ISBN: 978-3-89336-697-2

104. **Water and Organic Nitrate Detection in an AMS: Laboratory Characterization and Application to Ambient Measurements**
by A. Mensah (2011), XI, 111 pages
ISBN: 978-3-89336-698-9

105. **Entwicklung eines neuen Konzepts zur Steuerung der thermischen Ausdehnung von glaskeramischen Verbundwerkstoffen mit angepasster Fließfähigkeit am Beispiel der Hochtemperatur-Brennstoffzelle**
von E. Wanko (2011), xi, 134 Seiten
ISBN: 978-3-89336-705-4

106. **Tomographic reconstruction of atmospheric volumes from infrared limb-imager measurements**
by J. Ungermann (2011), xiv, 153 pages
ISBN: 978-3-89336-708-5

107. **Synthese und Identifizierung von substituierten Mg-Al-Cl Doppelhydroxidverbindungen mit Schwerpunkt IR-Spektroskopie**
von B. Hansen (2011), XII, 121 Seiten
ISBN: 978-3-89336-709-2

108. **Analysis of spatial soil moisture dynamics using wireless sensor networks**
by U. Rosenbaum (2011), xxii, 120 pages
ISBN: 978-3-89336-710-8

109. **Optimierung von APS-ZrO2-Wärmedämmschichten durch Variation der Kriechfestigkeit und der Grenzflächenrauhigkeit**
von M. E. Schweda (2011), 168 Seiten
ISBN: 978-3-89336-711-5

110. **Sorption of a branched nonylphenol isomer and perfluorooctanoic acid on geosorbents and carbon nanotubes**
by C. Li (2011), X, 102 pages
ISBN: 978-3-89336-716-0

111. **Electron Transport in the Plasma Edge with Rotating Resonant Magnetic Perturbations at the TEXTOR Tokamak**
by H. Stoschus (2011), iv, 113 pages
ISBN: 978-3-89336-718-4

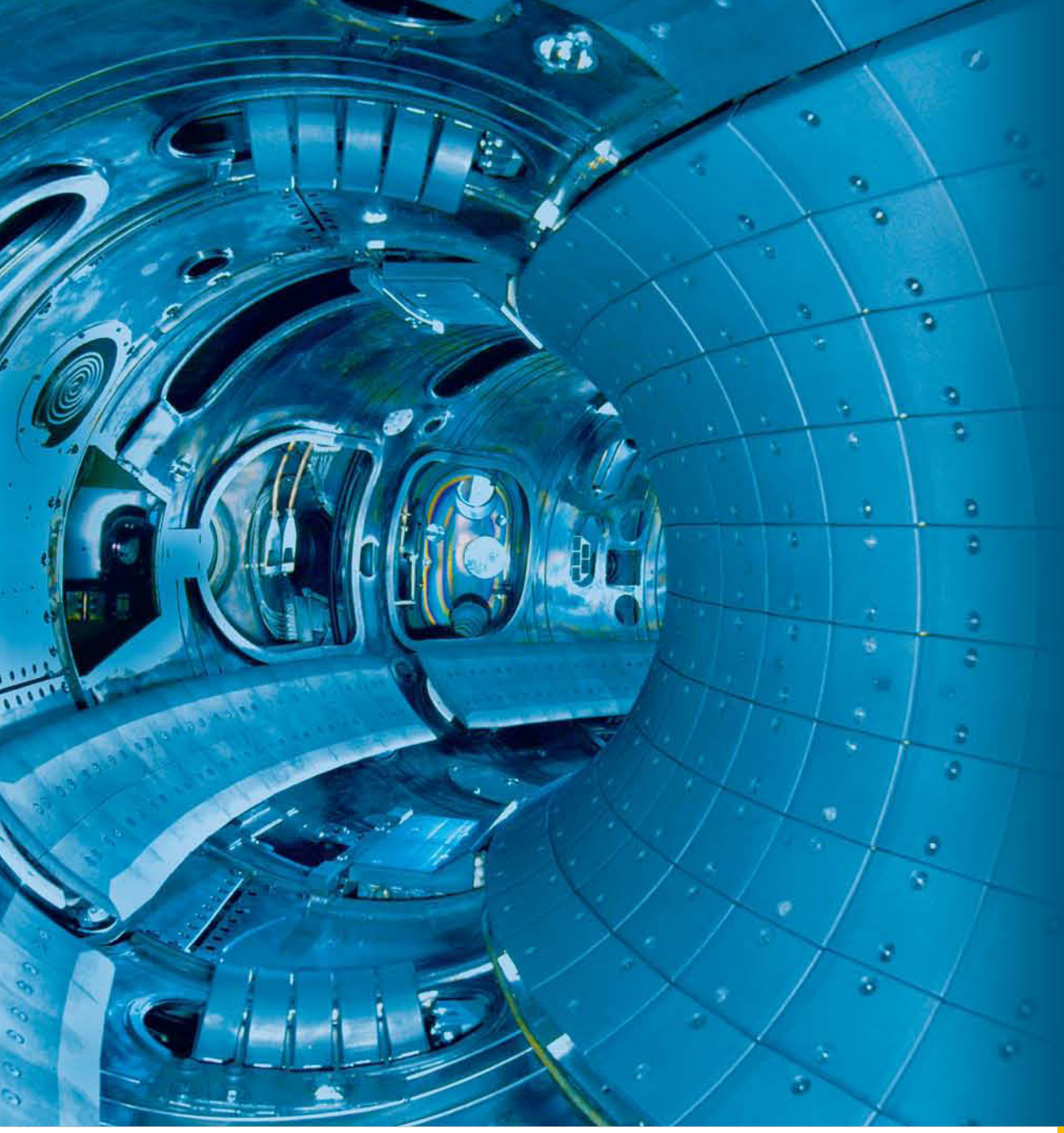

Energie & Umwelt / Energy & Environment
Band / Volume 111
ISBN 978-3-89336-718-4

JÜLICH
FORSCHUNGSZENTRUM